

University of Alberta

Performance of a Cadmium Tungstate MVCT Scanner

by

Paul Francis Kirvan

A thesis submitted to the Faculty of Graduate Studies and Research
in partial fulfillment of the requirements for the degree of

Master of Science

in

Medical Physics

Department of Physics

©Paul Francis Kirvan

Spring 2010

Edmonton, Alberta

Permission is hereby granted to the University of Alberta Libraries to reproduce single copies of this thesis and to lend or sell such copies for private, scholarly or scientific research purposes only.

Where the thesis is converted to, or otherwise made available in digital form, the University of Alberta will advise potential users of the thesis of these terms.

The author reserves all other publication and other rights in association with the copyright in the thesis and, except as herein before provided, neither the thesis nor any substantial portion thereof may be printed or otherwise reproduced in any material form whatsoever without the author's prior written permission.

Examining Committee

Dr. Satyapal Rathee, Department of Oncology

Dr. Gino Fallone, Department of Oncology, Department of Physics

Dr. Sharon Morsink, Department of Physics

Dr. Ron Sloboda, Department of Oncology, Department of Physics

Dr. Terence Riauka, Department of Oncology

To my mother, Dawn

Abstract

Megavoltage computed tomography (MVCT) and megavoltage cone beam computed tomography can be used for visualizing anatomical structures prior to radiation therapy treatments to assist in patient setup and target localization. These systems provide images using the same beam used for patient treatment, however their image contrast is limited by the low detective quantum efficiency (DQE) of the detectors currently available. By using higher DQE thick, segmented cadmium tungstate detectors we can improve the system contrast. This in turn would permit enhanced soft tissue visualization, allowing MVCT to be more useful.

This thesis describes the evaluation of a prototype MVCT system that uses thick, segmented detectors. The system was found to be able to easily visualize a 15 mm diameter 1.5% contrast target with 2 cGy of radiation dose delivered. This system could become the basis for improved commercial MVCT systems.

Acknowledgements

I would like to thank all of the people who have helped me over the course of my studies at the University of Alberta. I would like to thank the members of my supervisory committee, in particular my supervisor Dr. Satyapal Rathee, who was very generous with his time and always ready to offer assistance. Dr. Rathee's understanding and support was vital to my ability to complete this research.

I am grateful to all the member of the Medical Physics department at the Cross Cancer Institute, especially Dr. Tara Monajemi. Tara was a great help with the Monte Carlo and Wellhöfer dosimetry and was a great person to talk to about any subject be it physics or personal.

I would like to thank everyone who works in the machine shop and Technology Management Group for making the various bits and pieces that were needed along the way.

Finally, I would like to thank my mother, Dawn. She was diagnosed with a terminal form of colon cancer shortly after I began this work, and died less than three days after my thesis defense. She was a great mother and friend, and she will be an inspiration to me for the rest of my life.

List of Tables

- Table 2.1: Summary of contrast findings for several MVCT and MVCBCT systems. All of these systems were evaluated in a nominal 6 MV beam.*
- Table 3.1: Parameters used to calculate phase space data for each of four different runs using the Monte Carlo model.*
- Table 3.2: Parameters used in the Monte Carlo dose simulations.*
- Table 4.1: Dose Estimates for a single image created in the 6 MeV imaging beam and 6 MV treatment beam. The dose for the imaging beam is estimated for a full rotation, while the dose for the treatment beam is estimated for a minimal 200° rotation in order to reduce the dose as much as possible.*
- Table 4.2: Dose Estimates for a single image created with the 6 MeV imaging beam based on Monte Carlo simulations. In both geometries a dose rate of 1080 MU/min was assumed, and the dose per image is given for a full 360° rotation.*

List of Figures

- Figure 2.1: Qualitative diagram showing how increasing the thickness of a scintillator increases the potential for spreading of the optical photons before they reach the detector, resulting in reduced resolution.*
- Figure 2.2: Qualitative diagram drawn to scale showing how resolution is lost in a thick, segmented detector when a ray is incident on the detector at an oblique angle. Monte Carlo studies show that at 10° the resolution is severely reduced. As the angle increases, a ray can cause direct interactions in multiple detectors.*
- Figure 3.1: A 2D array (320 x 16) of $1 \times 1 \times 10 \text{ mm}^3$ CdWO₄ scintillators is arranged in an arc of radius 92.5 cm. Each of the twenty 16 x 16 array blocks is mounted on a 2D photodiode array. The arrays are mounted on long printed circuit boards which are connected to the data acquisition system (DAS) via long cables (not shown) to reduce the scattered radiation reaching the electronics in the DAS.*
- Figure 3.2: The timings for the DAS when running at 180 Hz as per Analogic Corporation documentation. The DAS integrates for only a small portion of each cycle, which measures the signal produced by a single linac pulse.*
- Figure 3.3: Uniform phantom image showing a centering artifact. The lower portion of the phantom appears to bulge and vertical streaks are seen. The effect is most apparent at the left and right sides denoted by arrows.*
- Figure 3.4: A bar phantom imaged with a 6 MV treatment beam. 90% of the pulses were dropped, resulting in just under one pulse being collected per degree of rotation. The dose delivered to produce this image is estimated to be around 6 cGy.*
- Figure 3.5: Geometry of the source location estimate. The ratio of the readings D_z to D_{ref} must be equivalent to the ratio of the total squared distances to those locations.*

- Figure 3.6: Overview schematic of the components that were included in the Monte Carlo simulations for a 6 MeV imaging beam.*
- Figure 3.7: Attenuation vs. thickness curve for a typical detector. A linear trend-line for the first three data points is shown alongside a second order polynomial trend-line for the full dataset.*
- Figure 3.8: Close-up view of the detector blocks showing the sub-millimeter gaps between the blocks.*
- Figure 3.9: Process used to create uniform factors. The data for each detector is averaged over all views and normalized. This is done for both the real data from a uniform phantom and mathematically generated ideal data for a same size uniform phantom. The final factors for each detector are generated by dividing the mathematical mean for that detector by the mean of the measured data for that detector.*
- Figure 3.10: Uniform factors for each detector. The uniform factors are generally unity, with the exception of detectors near the air gaps and the phantom edges.*
- Figure 4.1: The distance below isocenter (z) plotted as a function of the square root of the quotient of the reference chamber reading at isocenter and the chamber reading at point z . The slope corresponds to the distance from the effective bremsstrahlung source to the linac isocenter, while the y-intercept is the negative of this distance.*
- Figure 4.2: The first and second order coefficients of the polynomial fit to the beam hardening calibration data for the 6 MeV imaging beam. The parameters are shown for one of the central rows along the detector arc.*
- Figure 4.3: The first and second order coefficients of the polynomial fit to the beam hardening calibration data for the 6 MV treatment beam. The parameters are shown for one of the central rows along the detector arc.*
- Figure 4.4: Measured and simulated PDD in 6 MeV imaging beam. In both cases the SSD is 100 cm, the field size is 25 x 25 cm², and the curves are normalized at 1.1 cm (the depth of the maximum dose in both cases). Where error bars are not seen they are smaller than the data points.*

- Figure 4.5: Photon fluence per incident electron on the scattering foil as a function of energy in a 6 MeV imaging beam. There are 59%, 24%, 9%, 4.3% and 3.4% of photons in the range of 0-0.5 MeV, 0.5-1.5 MeV, 1.5- 2.5 MeV and 2.5-3.5 MeV respectively.*
- Figure 4.6: The profiles at 10 cm depth for the 6 MeV imaging beam and 6 MV treatment beam. The profiles were measured using a Wellhöfer IC-10 ion chamber being scanned across a 25 x 25 cm² field at a rate determined by Wellhöfer software.*
- Figure 4.7: Uniform phantom imaged using the 6 MeV imaging beam (top row) and 6 MV treatment beam (bottom row) in fan beam geometry. The phantom is seen without beam hardening or uniform factor correction (left column), with only beam hardening correction (centre column), and with both beam hardening and uniform factor correction (right column). The brightness and contrast were adjusted separately for each image in order to maximize the visibility of the artifacts.*
- Figure 4.8: SNR² vs. dose in fan-beam and cone-beam geometry. The error bars are calculated using propagation of errors in estimating mean signal and noise (i.e. standard deviation) of pixels. R² is 0.9996 for fan beam and 0.999 for cone beam geometry.*
- Figure 4.9: Portion of a CATPHAN500 resolution phantom having bar patterns ranging from 1 to 6 line pairs per cm. Images from left to right using: 6 MeV imaging beam at 2 cGy, 6 MV treatment beam at 60 cGy and TomoTherapy imaging beam with pitch =1.0.*
- Figure 4.10: Custom designed low contrast phantom of CATPHAN500 showing plugs of 3.0%, 2.5%, and 1.5% contrast (clockwise from left). For each contrast level there are cylinders of 20, 4, 5, 6, 7, 8, and 15 mm diameter. Images from left to right: 6 MeV imaging beam at 2 cGy and 8 mm slice thickness, Tomo beam with pitch = 1.0 and 5 mm slice thickness, and 6 MeV imaging beam at 4 cGy and 8 mm slice thickness.*

- Figure 4.11: CNR as a function of scan dose in fan and cone beam geometry. Nominal contrast values for cobalt energy are given in the legend.*
- Figure 4.12: Mean pixel value as a function of electron density for fan beam and cone beam geometry. $R^2 = 0.9998$ for both geometries. The error bars are smaller than the size of the data points.*
- Figure 4.13: Mean pixel value as a function of relative electron density for a diagnostic CT scanner that uses an X-ray tube operating at 120 KV potential. The data is obtained for the system (Brilliance Big Bore, Philips Medical Systems) installed in the radiotherapy department of the Cross Cancer Institute. The data is generally not linear and has a discontinuity around a relative electron density of 1.0.*

List of Abbreviations

AMFPI	Active Matrix Flat Panel Imager
CBCT	Cone Beam Computed Tomography
CMDF	Contrast Maintaining Dose Factor
CNR	Contrast to Noise Ratio
CSDA	Continuous Slowing Down Approximation
CT	Computed Tomography
DAS	Data Acquisition System
DQE	Detective Quantum Efficiency
EPID	Electronic Portal Imaging Device
kV	Kilo-Voltage
kVCT	kilo-Voltage Computed Tomography
LCD	Low Contrast Definition
LSF	Line Spread Function
MLC	Multi-Leaf Collimator
MTF	Modulation Transfer Function
MU	Monitor Unit
MV	Mega-Voltage
MVCBCT	Mega-Voltage Cone Beam Computed Tomography
MVCT	Mega-Voltage Computed Tomography
NIST	National Institute of Standards and Technology
NPS	Noise Power Spectrum
OBI	On-Board Imager
ODI	Optical Distance Indicator
PDD	Percent Depth Dose
ROI	Region Of Interest
SCD	Source to Chamber Distance
SNR	Signal to Noise Ratio
SSD	Source to Surface Distance

Table of Contents

CHAPTER 1: THESIS OVERVIEW.....	1
<i>References.....</i>	<i>5</i>
CHAPTER 2: BACKGROUND	7
2.1 MVCT Overview.....	7
2.1.1 MVCT History.....	8
2.1.2 MVCT Advantages.....	15
2.1.3 MVCT Disadvantages.....	17
2.1.4 Types of MVCT.....	20
2.1.5 Other Applications of MVCT.....	21
2.2 Thick Crystal Detectors	21
2.2.1 Advantages of Cadmium Tungstate	23
2.2.2 Previous Work at the University of Alberta	23
2.2.3 Current MVCT Prototype	26
2.3 Imaging Performance Tests	26
2.3.1 Uniformity	26
2.3.2 Signal to Noise Ratio	28
2.3.3 High Contrast Resolution.....	30
2.3.4 Low Contrast Definition.....	32
2.3.5 CT Number Linearity.....	33
<i>References.....</i>	<i>35</i>
Chapter 3: MATERIALS AND METHODS	41
3.1 System Description	41
3.1.1 Detectors	42

3.1.1.1 Cadmium Tungstate Scintillator	43
3.1.1.2 Septa	43
3.1.1.3 Detector Block Focusing	44
3.1.1.4 Photodiode and Optical Coupling	45
3.1.1.5 Radiation Damage vs Detector Response	46
3.1.2 Data Acquisition System	46
3.1.2.1 Sync Pulse	47
3.1.2.2 Long Cables.....	47
3.1.3 Rotating Stage.....	47
3.1.3.1 Rotating Stage Centering	48
3.1.4 LabView Software	49
3.2 6 MeV Imaging Beam	50
3.2.1 6 MeV Setup.....	52
3.2.1.1 Solid Water.....	52
3.2.1.2 Field Sizes.....	53
3.2.2 Wellhöfer PDD at 6 MeV.....	54
3.2.3 Source Location Estimation.....	54
3.2.4 Penumbra and Flatness.....	56
3.3 6 MV Treatment Beam.....	56
3.3.1 Irradiation Setup.....	57
3.4 Beam Hardening.....	57
3.4.1 Solid Water Phantoms	58
3.5 Imaging Dose Estimation	59
3.5.1 Reference Conditions	60
3.5.2 Imaging Conditions.....	61
3.6 Monte Carlo Investigations	61

3.6.1 BEAMnrc Accelerator Model	62
3.6.2 Phase Space Simulation.....	64
3.6.3 BeamDP Spectrum	66
3.6.4 DOSXYZnrc PDD Calculations	66
3.6.5 Dose Calculation	67
3.7 Phantoms.....	68
3.7.1 CATPHAN Phantoms	68
3.7.1.1 Uniformity	68
3.7.1.2 Ramp Phantom.....	68
3.7.1.3 High Contrast Resolution.....	69
3.7.2 Low Contrast Definition.....	69
3.8 Reconstruction.....	69
3.8.1 Dark Field and Flood Field Averaging.....	70
3.8.2 Drop Pulse Elimination.....	71
3.8.3 Multiple Rotation Averaging.....	72
3.8.4 Multiple Slice Averaging	72
3.8.5 Beam Hardening Correction	73
3.8.5.1 Determination of Equivalent Solid Water Thicknesses	74
3.8.6 Fan to Parallel Beam Conversion	74
3.8.6.1 Fan to Parallel Conversion Bug Workaround.....	75
3.8.7 Inverse Radon Transform.....	76
3.8.8 Uniform Factor Correction	76
3.9 Image Analysis.....	79
3.9.1 Conversion Process	80
3.10 TomoTherapy.....	80

<i>References</i>	81
Chapter 4: RESULTS AND DISCUSSION	83
4.1 Beam Characteristics	83
4.1.1 <i>Source Location Estimation</i>	83
4.1.2 <i>Beam Hardening</i>	85
4.1.2.1 <i>Parameters in 6 MeV Imaging Beam</i>	87
4.1.2.2 <i>Parameters in 6 MV Treatment Beam</i>	88
4.1.3 <i>PDD measurements</i>	89
4.1.4 <i>Monte Carlo Spectrum</i>	90
4.1.5 <i>Ratio Dose Estimate</i>	92
4.1.6 <i>Monte Carlo Dose Estimate</i>	93
4.1.7 <i>Penumbra and Flatness</i>	95
4.2 Artifact Correction	98
4.3 Uniformity	100
4.3.1 <i>Signal to Noise Ratio</i>	101
4.4 High Contrast Resolution	102
4.5 Low Contrast Definition	104
4.6 CT Number Linearity	107
<i>References</i>	110
CHAPTER 5: CONCLUSIONS	111
BIBLIOGRAPHY	114

CHAPTER 1: THESIS OVERVIEW

Modern external beam radiation therapy techniques used to treat cancer, such as inverse planned intensity modulated radiation therapy and TomoTherapy, require medical imagery in order to verify the position of the tumor prior to treatment [Verellen, et al. 2008]. This imagery can be done by incorporating a separate imaging system into the treatment process. For example, an x-ray tube can be attached to the treatment gantry to permit planar x-ray images or cone-beam computed tomography (CBCT) [Jaffray, et al. 2000]. Ultrasound imagery has been implemented in some cases [Lattanzi, et al. 1999] and there is work underway to incorporate magnetic resonance imaging into the treatment process [Fallone, et al. 2009].

There are also imaging techniques that create images using the same high energy radiation beam used for treatment. These include electronic portal imaging devices (EPIDs) that are limited to planar images [Munro 1995], as well as megavoltage computed tomography (MVCT) [Ruchala, et al. 1999] and megavoltage cone beam computed tomography (MVCBCT) [Morin, et al. 2006] that provide cross sectional imagery of a patient. MVCT techniques have potential benefits including simpler hardware and lower cost compared to systems that incorporate separate kilovoltage CT (kVCT) capability.

In addition to use in the detection of setup errors, medical imaging is required to plan external beam radiation therapy procedures. Typically in this context a kVCT system is used to scan the patient [Kijewski, et al. 1978]. The attenuation values from the kVCT scan are then used to estimate the electron density throughout the patient, which in turn is used to calculate how a high energy treatment beam will deposit radiation dose in the patient. MVCT can benefit treatment planning [Thomas, et al. 2009]

as the attenuation at higher energy is less affected by atomic composition and more representative of the attenuation that will occur in the treatment beam. A further benefit for treatment planning is that MVCT has less artifacts for patients who have metal implants, allowing the attenuation in the region of an implant to be calculate more accurately.

Unfortunately, MVCT image quality is currently limited compared to other imaging modalities [Morin, et al. 2006]. Most critically, it offers poor low contrast definition (LCD), which is required to differentiate one soft tissue from another. In other words, it is difficult for physicians to differentiate between tumor and surrounding healthy tissue. This lack of contrast is due primarily to the low detective quantum efficiency (DQE) of current MVCT detectors. One promising technology that could improve the DQE of MVCT detectors is the use of thick, segmented, cadmium tungstate detectors [Monajemi, et al. 2004].

This thesis focuses on the evaluation of a prototype MVCT system based on cadmium tungstate technology that was designed to have improved LCD. The key research in this thesis has been published in the journal Medical Physics [Kirvan, et al. 2010]. This thesis is organized into the following chapters.

Chapter 2: Background

This chapter begins with the history of MVCT including previously tested research systems as well as current commercial systems. It then discusses the benefits of cadmium tungstate detectors and summarizes several years of related research that has been completed at the University of Alberta, including some previous prototype systems. This chapter introduces the most recent prototype cadmium tungstate MVCT system, which is the focus of this work, and provides an overview of the

important image characteristics that the current system will be evaluated on.

Chapter 3: Materials and Methods

A detailed description of all elements of the current MVCT prototype system is provided here. This includes a description of the detectors, data acquisition system (DAS), rotating stage, DAS control software, phantoms, and image reconstruction software. This chapter also describes the setup of the linear accelerators (linacs) with which the system was tested, the experiments required to characterize the photons produced by the linacs, and the experiments, both measurements and computer simulations, required to estimate the dose delivered during imaging. The system was tested in both a 6 MeV imaging beam, as well as a 6 MV treatment beam.

Chapter 4: Results and Discussion

This chapter describes the results of the experiments conducted to characterize the 6 MeV imaging beam and the 6 MV treatment beam. The 6 MeV imaging beam was assessed in detail including beam flatness, energy spectrum, virtual source location, and beam hardening parameters. A discussion of the estimated dose is provided here, followed by the key analysis of the prototype system's image quality. This analysis includes the uniformity, signal to noise ratio, LCD, high contrast resolution, and CT number linearity.

Chapter 5: Conclusions

This chapter summarizes the principal characteristics of the prototype MVCT system. It also offers possible improvements that could be done to enhance this system in future work, as well as indicates how these results relate to the field of radiation therapy.

References

Fallone, B. G., Murray, B., Rathee, S., Stanescu, T., Steciw, S., Vidakovic, S., Blosser, E. & Tymofichuk, D. First MR images obtained during megavoltage photon irradiation from a prototype integrated linac-MR system. *Medical physics* 36, 2084-2088 (2009).

Garcia-Ramirez, J. L., Mutic, S., Dempsey, J. F., Low, D. A. & Purdy, J. A. Performance evaluation of an 85-cm-bore X-ray computed tomography scanner designed for radiation oncology and comparison with current diagnostic CT scanners. *International Journal of Radiation Oncology Biology Physics* 52, 1123-1131 (2002).

Jaffray, D. A. & Siewerdsen, J. H. Cone-beam computed tomography with a flat-panel imager: Initial performance characterization. *Medical physics* 27, 1311-1323 (2000).

Kijewski, P. K. & Bjarngard, B. E. The use of computed tomography data for radiotherapy dose calculations. *International Journal of Radiation Oncology Biology Physics* 4, 429-435 (1978).

Kirvan, P. F., Monajemi, T. T., Fallone, B. G. & Rathee, S. Performance characterization of a MVCT scanner using multislice thick, segmented cadmium tungstate-photodiode detectors. *Medical physics* 37, 249-257 (2010).

Lattanzi, J., McNeeley, S., Pinover, W., Horwitz, E., Das, I., Schultheiss, T. E. & Hanks, G. E. A comparison of daily CT localization to a daily ultrasound-based system in prostate cancer. *International Journal of Radiation Oncology Biology Physics* 43, 719-725 (1999).

McCollough, C. H. & Zink, F. E. Performance evaluation of a multi-slice CT system. *Medical physics* 26, 2223-2230 (1999).

Monajemi, T. T., Steciw, S., Fallone, B. G. & Rathee, S. Modeling scintillator-photodiodes as detectors for megavoltage CT. *Medical physics* 31, 1225-1234 (2004).

Morin, O., Gillis, A., Chen, J., Aubin, M., Bucci, M. K., Roach, M., 3rd & Pouliot, J. Megavoltage cone-beam CT: system description and clinical applications. *Medical dosimetry : official journal of the American Association of Medical Dosimetrists* 31, 51-61 (2006).

Munro, P. Portal imaging technology: Past, present, and future. *Seminars in radiation oncology* 5, 115-133 (1995).

Ruchala, K. J., Olivera, G. H., Schloesser, E. A. & Mackie, T. R. Megavoltage CT on a tomotherapy system. *Physics in Medicine and Biology* 44, 2597-2621 (1999).

Thomas, T. H., Devakumar, D., Purnima, S. & Ravindran, B. P. The adaptation of megavoltage cone beam CT for use in standard radiotherapy treatment planning. *Physics in Medicine and Biology* 54, 2067-2077 (2009).

Verellen, D., De Ridder, M. & Storme, G. A (short) history of image-guided radiotherapy. *Radiotherapy and oncology : journal of the European Society for Therapeutic Radiology and Oncology* 86, 4-13 (2008).

CHAPTER 2: BACKGROUND

This chapter provides an overview of megavoltage computed tomography. It discusses the advantages and disadvantages of using MVCT in medicine as well as some of its medical applications. A brief history of MVCT and a summary of its published implementations is provided. The various adaptations of MVCT, such as multi-slice MVCT, helical MVCT, and cone-beam MVCT are introduced. This chapter also describes some of the previous work done at the University of Alberta and other institutions involving the use of cadmium tungstate photodiode detectors in MVCT. Finally, this chapter provides a description of the standard attributes of a computed tomography system and how they can be measured in order to assess the system's imaging performance. These attributes include image uniformity, signal-to-noise ratio, high contrast resolution, low contrast definition, and CT number linearity.

2.1 MVCT Overview

MVCT systems were described as early as 1982 [Simpson, et al. 1982]. These systems are based on the same principles as kilovoltage computed tomography (kVCT) systems. kVCT systems are employed in medicine for the diagnosis of many medical conditions [Johns, et al. 1993], as well as for the planning of external beam radiation therapy [Zubal, et al. 1994]. Like kVCT systems, MVCT systems rely on the collection of many 1D (fan-beam) or planar (cone-beam) projections of the object being imaged as a photon source is rotated around a target. These projections are then used to reconstruct an image, typically by a process called filtered back projection [Ramachandran, et al. 1971]. The resulting image represents

the linear attenuation coefficient map in a cross sectional slice, also referred to as a tomograph, of the object.

Because they image using ionizing radiation, kVCT and MVCT systems deliver radiation dose, particularly throughout the region of the patient being imaged. To reduce the patient dose, kVCT systems employ photons at an energy chosen to produce optimal contrast for a given radiation dose to the patient. This optimization is important for in-vivo applications since the radiation dose may cause health problems such as cancer [Smith-Bindman, et al. 2009] in the patient and should therefore be minimized. Typically, kVCT systems image using photons of a peak energy around 120 keV¹. MVCT systems differ in that they image using the much higher energy photon beams used in radiation therapy. For example, a typical linear accelerator used for external beam radiation treatments has a peak photon energy of 6 MeV or greater.

2.1.1 MVCT History

The first MVCT system was developed at the University of Arizona [Simpson, et al. 1982; Swindell, et al. 1983]. That system used plastic scintillators in conjunction with silicon photodiodes to detect photons from a 4 MV Varian Clinac-4 linear accelerator. The scintillator plastic had a density of 1.1 g/cm³, and the scintillator elements were relatively large- 7.4 mm x 20 mm in the directions perpendicular to the beam, and 50 mm in

¹ Most photon sources used for medical imaging produce radiation via the bremsstrahlung effect for a nearly mono-energetic electron beam stopping in a high atomic number target material. They produce a continuous spectrum of photons from zero energy up to the maximum energy of the electron beam. The resulting photon energy spectra are generally referred to by the electron beam accelerating potential. For example, a 120 kV source produces photons with an energy ranging from zero to 120 keV.

the direction parallel to the beam, hereafter referred to as the thickness direction.

The Arizona system was later upgraded to use bismuth germanate ($\text{Bi}_4\text{Ge}_3\text{O}_{12}$) detectors [Swindell, et al. 1983]. Those detectors had a much greater absorption efficiency of 83% compared to 25% for the plastic detectors, despite the thickness being the same 50 mm. The investigators reported that a large disk with a contrast of 1% could be visualized at 10 cGy dose. That dose is too large for daily imaging of a patient. The Arizona prototype was later modified further and tested in beams with a peak photon energy up to 50 MV [Brahme, et al. 1987].

The Nakagawa group at the University of Tokyo later created a MVCT system using cadmium tungstate as a scintillator [Nakagawa, et al. 1994]. Cadmium tungstate, as will be discussed later, has beneficial properties for use as a scintillator, particularly its high density. Nevertheless, that particular system was unable to detect a 2.5 cm diameter polystyrene cylinder on a water background [Nakagawa, et al. 1992]. The cylinder had a contrast of 4.1% and was imaged at the more clinically acceptable doses of 1.4 cGy and 2.8 cGy in a 4 MV or 6 MV beam respectively, from a Mitsubishi linac (Mitsubishi linac ML-20M, Japan).

By the 1990s, electronic portal imaging devices (EPIDs) had become readily available [Antonuk 2002]. These EPIDs generally consisted of a large rectangular active matrix flat panel imager (AMFPI) on a retractable arm attached to the same rotating gantry as the photon source used to deliver a radiation therapy treatment. The AMFPI detects photons via Compton interactions in a thin copper plate and an even thinner phosphor screen. These interactions produce scattered electrons that deposit energy in the phosphor screen, which then emits visible light. The visible light is collected to form an image. An EPID can produce a planar image

using the same source used for treatment. These images can be used to detect errors in the patient setup based on bony anatomy prior to treatment. Also, if properly calibrated they can be used during treatment to record how much dose was delivered- a process known as treatment verification. Several attempts were made to do MVCT imaging using EPIDs by rotating the source and EPID around a patient while collecting projection data.

Among those were Guan and Zhu [Guan, et al. 1998] who used an EPID consisting of a fluorescent screen and charge-coupled-device (CCD) camera. Using a 6 MV beam (Primus linac, Siemens Medical Systems, Concord, CA) they were able to achieve a contrast detectability on the order of 2.5% using a large 50 cGy dose. In Germany, Hesse [Hesse, et al. 1998] used an EPID (BIS 700, Wellhofer Dosimetrie, Schwarzenbruck, Germany) consisting of a 1 mm copper plate coated with a thin layer of $\text{GD}_2\text{O}_2\text{S:Tb}$ phosphor. The light produced in the phosphor was collected by a CCD camera. A contrast of 9% was reported for a large dose (more than 15.8 cGy). Midgley [Midgley, et al. 1998] used a commercial EPID (Varian Portal Vision V3.1, Varian Medical Associates, Palo Alto, California) in conjunction with a 6 MV linac beam (Varian 2100C, Varian Medical Associates, Palo Alto, California). The EPID was a liquid-filled ionization design and a contrast of 4% was reported at 90 cGy.

For the systems discussed in the previous paragraph, the beam used for imaging was collimated to a slit in order to approximate a typical CT system. Several other groups have used a wide beam in conjunction with the entire EPID in what is referred to as cone beam geometry. Some examples of such research include work done by Ford [Ford, et al. 2002] using an active matrix flat panel imager (aS500, Varian Medical Systems, Palo Alto, CA). He was able to achieve 2% contrast at a huge dose of 200 cGy. Groh used another flat panel imager (RID 256-L, PerkinElmer

Optoelectronics) to obtain 2% contrast at 32 cGy [Groh, et al. 2002]. Mosleh-Shirazi achieved 2% contrast at 40 cGy using CsI crystals and a CCD camera [Mosleh-Shirazi, et al. 1998]. Seppi used a high resolution flat panel imager (PaxScan 4030A, Varian Medical Systems, Palo Alto, CA) to obtain an estimated 1% contrast at 16 cGy [Seppi, et al. 2003]. Dr. Antonuk's group has done extensive research on the use of thick crystal detectors in EPIDs [Wang, et al. 2006; Wang, et al. 2009] that could be used for cone beam MVCT. Based on *theoretical* Monte Carlo calculations, they believe that a 4 cm thick CsI detector could resolve electron density differences of 1.3% using a dose of 3.1 cGy in cone-beam geometry [Wang, et al. 2008].

Most of the systems mentioned so far require too large a radiation dose to be clinically useful. However, some MVCT systems have become commercially available for clinical use. One of the most used MVCT systems is the TomoTherapy HiArt system (TomoTherapy Inc, Madison WI) [Mackie, et al. 1999; Mackie, et al. 2003; Ruchala, et al. 1999; Ruchala, et al. 1999; Ruchala, et al. 2000]. It uses a detector consisting of 0.32 mm wide tungsten septa alternating with 0.32 mm wide chambers filled with high pressure xenon gas. The detector is 2.54 cm thick. A 300 V bias is applied to every second septum. The incident photons interact with the septa via Compton scattering, producing scattered electrons that ionize gas in the chambers. While the interaction probability of a photon incident on a 2.54 cm thick tungsten septum is quite high relative to other thinner detectors, the geometrical efficiency of the detector as a whole is only 50%, because half the surface area is taken up by the gas chambers that do not cause a significant amount of ionization in direct interactions with the photon beam. The TomoTherapy detector is constructed in an arc focused to 110 cm, while the photon source is 145 cm from the detector. This mis-focusing may increase the contrast at points away from the central axis of the beam, but at a cost of lost spatial resolution. The 6 MV

linac used as the source of photons in TomoTherapy MVCT is detuned to produce a 3.5 MV beam during imaging, so as to take advantage of the higher contrast for a given dose available at lower energy.

Another commercial MVCT system is the Siemens MVision cone-beam MVCT (Siemens Medical Solutions, Concord, CA). The MVision system uses a flat panel EPID consisting of gadolinium oxo-sulphide terbium activated $Gd_2O_2S:Tb$ scintillators coupled to amorphous silicon photodiodes. That system was able to detect a 2 cm diameter object with 1% contrast using a dose of 10 cGy [Gayou, et al. 2007].

The minimum detectable contrasts reported by many of the above mentioned groups are summarized in Table 2.1. It is noteworthy that none of these systems demonstrate an ability to resolve 1% contrast targets using less than 10 cGy dose. This would limit such systems to the detection of bony anatomy and would not permit soft tissue visualization at an acceptable dose in most cases. Also, the contrast performance of flat panel detectors in cone-beam geometry is especially poor. The TomoTherapy system, which uses a lower energy beam, has been shown to offer better performance and is further discussed later in this work.

Publication	Technology	Minimum Contrast Detected	Dose Require to Achieve Stated Contrast (cGy)
Swindell et al. 1983	Bi ₄ Ge ₃ O ₁₂ scintillators	1%	10
Nakagawa et al. 1994	CdWO ₄ scintillators	>4%	>2.8
Guan et al. 1998	Commercial EPID	2.5%	50
Hesse et al. 1998	Gd ₂ O ₂ S:Tb EPID	9%	>15.8
Midgley et al. 1998	Varian Portal Vision Liquid Filled EPID	4%	90
Ford et al. 1992	Active Matrix Flat Panel EPID (MVCBCT)	2%	200
Groh et. al 2002	Flat Panel EPID (MVCBCT)	2%	32
Mosleh-Shirazi et al. 1998	Cs:I Scintillators (MVCBCT)	2%	40
Seppi et al. 2003	High Resolution Flat-Panel (MVCBCT)	1%	16
Gayou et al. 2007	Flat panel EPID with Gd ₂ O ₂ S:Tb scintillators (MVCBCT)	1%	10

Table 2.1: Summary of contrast findings for several MVCT and MVCBCT systems. All of these systems were evaluated in a nominal 6 MV beam.

While most of the detectors mentioned so far consist of either a copper plate and phosphor or a scintillator and photodiode, some groups are researching novel detector designs. These include tri-electrode ion

chambers [Samant, et al. 2007], Cerenkov radiation detectors [Mei, et al. 2006], and segmented phosphors [Sawant, et al. 2005]. These approaches may be able to increase the detective quantum efficiency (DQE) of the detectors, however at present no actual images have been published for such systems.

Some MVCT research has been done that focuses not on the detector design, but rather on the photon beam itself. The linear accelerators (linacs) generally used to generate high energy photon beams operate by colliding electrons that have been accelerated to high energy into a metal target. The target is composed of a high atomic number material that will maximize the output of bremsstrahlung radiation. This method of photon production results in a continuous spectrum of photons from zero energy up to nearly the maximum energy of the incident electrons. However, the low energy components of that spectrum are mostly self-absorbed by the target. Medical linacs also employ a cone-shaped flattening filter in the path of the beam. The filter serves to give the radiation field used for treatment a flatter profile in the plane perpendicular to the axis of the linac, which makes treatment planning easier, but the filter preferentially attenuates the low energy components of the beam. While the loss of low energy components is beneficial for radiation therapy because they are the least penetrating, the loss of the low energy components reduces the contrast when the beam is used for imaging. It has been shown that image quality can be improved by using a low atomic number carbon target that generates a lower energy spectrum [Galbraith 1989; Ostapiak, et al. 1998; Faddegon, et al. 2008]. The flattening filter can be removed for imaging, and the linac can be de-tuned to produce a lower energy beam than that normally used for treatment. Some research has been done to investigate the dosimetric characteristics of such modified beams [Flynn, et al. 2009].

2.1.2 MVCT Advantages

One advantage of MVCT lies in the fact that it is relatively simple to implement on a linac used for external beam radiation therapy. Since MVCT uses the same beam generation system that is used for treatment, no additional photon source is required. This is different from increasingly common on-board imagers (OBIs) that use a secondary kV source. This advantage in simplicity could translate into lower costs for MVCT systems.

A further benefit to MVCT is that the attenuation of photons in low atomic number materials at megavoltage energies is almost entirely due to Compton scattering, a process in which an incident photon interacts with an electron in the medium causing a transfer of some of its energy to that electron. This results in a scattered electron as well as a scattered photon of lower energy than the incident photon. The amount of Compton scattering in a material is nearly proportional to the density of electrons in that material. This means that the attenuation measured by a MVCT system is proportional to electron density, which is not the case for kVCT.

A kilovoltage beam experiences a larger proportion of photo-electric interactions, which are highly dependent on the atomic number of the material, roughly proportional to Z^4 at low atomic number [Johns, et al, 1983]. Because of this the attenuation detected by a kVCT system does not increase linearly with electron density. Materials such as bone, which contains relatively high atomic number elements such as calcium, have a higher attenuation relative to their electron density. In radiation treatment planning, the attenuation observed in a kVCT scan is correlated to the electron density of the medium. These electron densities are in turn used to calculate the dose deposition in a high energy beam later used for treatment. Non-linearities in the correlation of attenuation to electron

density in the kVCT scans can therefore translate into less accurate treatment plans.

The goal of external beam radiation therapy treatment planning is to ensure that a region within a patient receives a prescribed dose of radiation in order to kill malignant cells, while minimizing the dose to healthy tissue. In order to do this it is necessary to calculate the dose deposited by a megavoltage therapy beam as it passes through a patient. The attenuation of the beam is often calculated using electron densities derived from a kVCT scan [Kijewski, et al. 1978; Parker, et al. 1979]. However, a MVCT scan that more accurately determines the electron density could improve the accuracy of these calculations by up to 1% [Ruchala, et al. 2000]. Ever better dosimetry protocols, such as the TG-51 protocol [Almond, et al. 1999] have been developed with the aim of calculating patient doses to well within 5% accuracy. Therefore, a 1% improvement due to superior dose calculations could be responsible for eliminating a significant fraction of the remaining error. The development of dosimetry protocols is motivated by evidence [Schultz, et al. 1983] that the treatment of some diseases may require a radiation dose accurately delivered to within 5%.

At kV energies, metal implants, such as prosthetic hips or dental fillings, can severely degrade image quality by causing streak artifacts, resulting in less accurate dose calculations [Keall, et al. 2003; Seco, et al. 2006; Wei, et al. 2006]. Because the attenuation coefficient of photons generally decreases with increasing energy, these implants preferentially absorb the low energy components of the beam in a process known as beam hardening. Because of this, the beam that exits a metal implant is of higher average energy than the beam that entered it. The exiting beam will then have lower attenuation as it travels through the rest of the patient, leading to reconstruction artifacts. Also, it is possible for a metal with a

high density and atomic number to absorb nearly all the kV photons incident on it, leaving an insufficient number to reach the detector. These metal artifacts are less severe in MVCT [Morin, et al. 2006, Hong, et al. 2007], because the MV spectrum is less prone to significant beam hardening and it would require a much larger amount of metal to cause nearly total attenuation of a MV beam.

2.1.3 MVCT Disadvantages

A key concept required to understand the limitations of MVCT is Detective Quantum Efficiency (DQE). Ideally, the input signal on an individual detector element in a CT system is a ray of photons traveling along a straight-line path from the radiation source to the detector element. The signal varies about some mean value due to statistical fluctuations in the number of photons being emitted by the source along that ray, as well as statistical fluctuations associated with possible interactions the photons in that ray could have with any objects it passes through as it travels from the source to the detector, such as a patient. The DQE of a detector is defined as the ratio of the squared output signal-to-noise ratio (SNR) to the squared input SNR. Qualitatively, the DQE is a measure of the ability of a detector to output the same SNR as the photon beam input. No system has the ability to do this perfectly (100% DQE) because not all incident photons interact with the detector (a lack of quantum efficiency) and the manner in which the photons are detected introduces further sources of noise.

DQE is a function of spatial frequency. Spatial frequency is a measure of how often a structure repeats in a given distance, typically measured in line pairs per millimeter or line pairs per centimeter. High spatial frequencies must be detected in order to detect small objects. The input

SNR is calculated from the spatial photon fluence distribution, usually uniform, incident on the detector. The output squared SNR as a function of spatial frequency is measured as the ratio of squared modulation transfer function to the noise power spectrum (NPS) calculated from the spatial signal distribution of the detector for the given incident fluence distribution. The modulation transfer function and output noise power spectrum respectively quantify detector response and noise as a function of spatial frequency.

The main disadvantage of MVCT is that it offers inherently lower contrast for a given dose to the patient [Morin, et al. 2006, Morin, et al. 2007, Morin, et al. 2009, Stutzel, et al. 2008]. Part of this can be attributed to the same lack of photoelectric interactions at MV energies that makes MVCT useful for electron density calculation. This eliminates the variations in atomic number among tissue types as a source of contrast, leaving changes in electron density as the sole source of contrast. Furthermore, the amount of energy deposited by a megavoltage beam is much greater than the amount of energy deposited by a kilovoltage beam of the same photon fluence. This is because the mass energy absorption coefficients vary only slightly between kilovoltage and megavoltage beams. For example, at 100 keV the mass energy absorption coefficient in water is 0.025 cm²/g, whereas it is 0.026 cm²/g at 2 MeV. However, the energy in the 2 MeV beam is 20 times greater for the same fluence.

Ruchala et al. [1999] quantified this effect by deriving a contrast maintaining dose factor (CMDf) that provides the amount by which the dose must increase in order to maintain a given contrast as the beam energy is changed. The CMDf is defined in Equation 2.1 where:

μ_{en} is the linear energy absorption coefficient;

μ is the attenuation coefficient;

E is the beam energy;

$\bar{\phi}_{phan}$ is the average fluence inside a cylindrical phantom;

ϕ_{det} is the fluence at the detector;

η is the DQE; and

The superscript MV and subscript kV indicate that the expression in the absolute value bracket is evaluated separately at MV and kV energies, and then a ratio of the MV and kV values is taken before being multiplied by the expression in parenthesis on the right.

$$CMDf = \left| \frac{\mu_{en} \cdot E \cdot \bar{\phi}_{phan}}{\eta \cdot \phi_{det}} \right|_{kV}^{MV} \left(\frac{\mu_{kV}}{\mu_{MV}} \right)^2 \quad (2.1)$$

A look at Equation 2.1 shows that the CMDf between kilovoltage and megavoltage energies will be large because the attenuation coefficient is much larger at lower energy, the energy itself is much greater for megavoltage beams, and the linear energy absorption coefficients are similar. The ratio of the fluence at the phantom to the fluence at the detector is fixed for a given energy, and is larger for higher energy beams. The only factor in Equation 2.1 that can be adjusted is the DQE. Current flat panel MVCT detectors have a very low DQE around 1% [Cremers, et al. 2004, El-Mohri, et al. 2001] primarily because they are thin and only interact with a tiny fraction of incident photons. This presents an opportunity for improving MVCT using higher DQE detectors.

2.1.4 Types of MVCT

Similar to kVCT systems, MVCT systems have been implemented in both fan beam and cone beam geometry. In fan beam geometry, the detectors are arranged in an arc that is rotated around the patient along with the photon source. Typically, the patient lies on a couch which is translated at a constant speed while the detector and source rotate around a fixed position, referred to as an isocenter. This approach is called helical CT. TomoTherapy is a commercial implementation of helical MVCT [Ruchala, et al. 1999].

Fan beam systems frequently have multiples rows of detectors in order to image multiple slices of the patient on each rotation of the source. This enables the imaging to be completed in fewer rotations and is referred to as multi-slice CT. Taken to an extreme, a very large area detector can be used instead of a detector arc. This allows for a large volume to be imaged on a single rotation and is known as cone-beam CT (CBCT) [Cho 1995, et al.; Jaffray 2000, et al.; Swindell, et al. 1983].

Because of their larger area coupled with the wider beams needed to image using CBCT, more scattered photons are incident on CBCT detectors than fan beam detectors (and multi-slice detectors detect more scatter than single-slice systems). This scatter originates both in the patient, where a wider beam creates more scattered photons, and in the detector itself. Despite their consequently reduced image quality, CBCT systems are useful because they allow a large volume to be imaged for each source rotation. This is particularly important for OBIs attached to radiation treatment gantries, because these gantries rotate extremely slowly compared to stand alone CT scanners and it is desirable to reduce imaging times in order to speed up the procedure for the patient, as well as increase patient throughput.

2.1.5 Other Applications of MVCT

MVCT has potential to be useful outside of medicine in industrial fields. The main disadvantage of MVCT, the low contrast for a given dose, may be less of a barrier for applications where the dose can be increased beyond what is acceptable for in-vivo use. Greater tolerance to radiation dose also makes multi-energy computed tomography, which provides more information about the composition of materials being imaged by imaging multiple times using beams of different energies, more feasible. The reduction of metal artifacts may be valuable for imaging metallic parts and machinery. Industrial users of MVCT would not need to be concerned about patient motion artifacts, and could therefore image more slowly using detector geometry that reduces the scatter reaching the detector. A couple of the many possible industrial uses of MVCT are for detecting defects in aircraft components [Azevodo, et al. 1993] and air cargo inspection [Bendahan, et al. 2008].

2.2 Thick Crystal Detectors

Flat panel detectors typically have low DQE because the copper plates or scintillators they employ are very thin (on the order of one millimeter). One way to increase the DQE of scintillator systems would be to increase the scintillator thickness. However, a thicker scintillator would allow more spreading of the optical photons before they are collected by the detector (Figure 2.1). This will result in a decrease of DQE as the thickness of scintillator increases. To reduce this, the scintillator can be segmented into small elements that are optically isolated from each other by optically opaque septa placed between the elements. These septa should preferably be reflective or have a reflective coating, so photons that contact the septa are not lost to absorption and are instead reflected back

into the scintillator where ideally they will eventually reach the detector, though possibly after many reflections. The length and width, referred to as the pitch, of the scintillator elements are made as small as possible, to allow for maximum resolution. In these studies, scintillator elements with a pitch as little as 1 mm and a thickness as large as 10 mm are used.

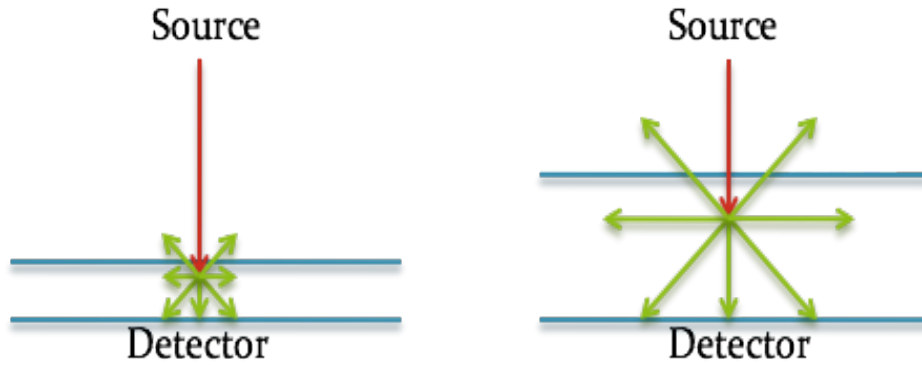


Figure 2.1: Qualitative diagram showing how increasing the thickness of a scintillator increases the potential for spreading of the optical photons before they reach the detector, resulting in reduced resolution.

2.2.1 Advantages of Cadmium Tungstate

The use of thick, high density scintillating crystals as detectors shows significant potential as a means to increase the DQE, and thereby the contrast, of MVCT systems. Of these, cadmium tungstate detectors show particular promise.

Cadmium tungstate has a high density of 7.9 g/cm³. The higher density compared with other crystals allows for more photon interactions in a given thickness of crystal. Cadmium tungstate also has a good optical yield of 20,000 photons per MeV absorbed and low optical absorption [Kobayashi, et al. 1994]. Over the last several years, several projects have been undertaken at the University of Alberta as well as other institutions to demonstrate cadmium tungstate MVCT systems.

2.2.2 Previous Work at the University of Alberta

Monte Carlo studies were conducted to investigate the system design parameters of a thick, segmented, MVCT system [Monajemi, et al. 2006 (1)]. In particular, the effect of beam divergence on the resolution of a thick, segmented detector was analyzed. Because the scintillator elements are much thicker than their width, rays that are incident on the detector at an oblique angle can pass through multiple detectors and thereby reduce resolution (Figure 2.2). It was found that for a flat detector array of 10 mm height and 1 mm pitch, a substantial loss of resolution occurs as little as 10° away from the central axis. Therefore, for a thick, segmented MVCT system to offer adequate resolution the detector array must be focused to the photon source to eliminate the effect of beam divergence.

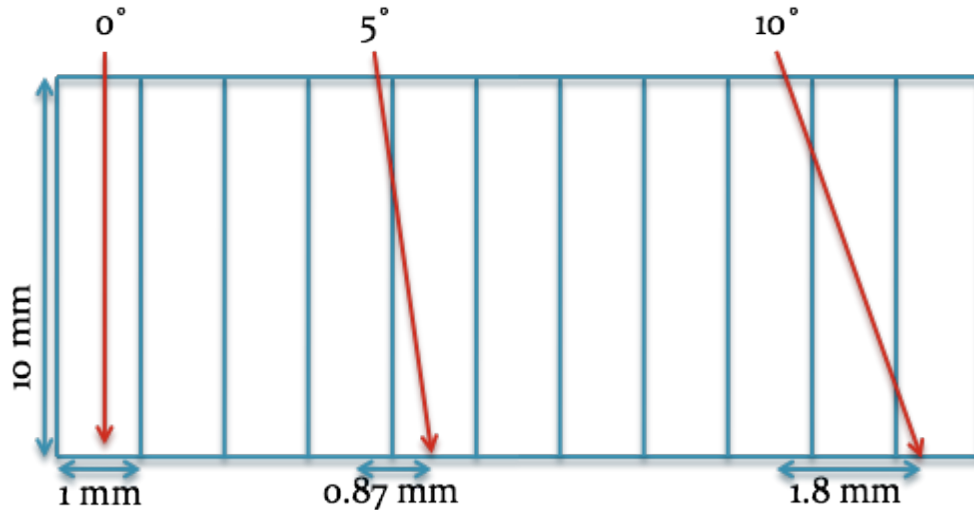


Figure 2.2: Qualitative diagram drawn to scale showing how resolution is lost in a thick, segmented detector when a ray is incident on the detector at an oblique angle. Monte Carlo studies show that at 10° the resolution is severely reduced. As the angle increases, a ray can cause direct interactions in multiple detectors.

The Monte Carlo studies also investigated the effects of increasing the scintillator thickness. Increasing the thickness increases the likelihood of photons interacting within the scintillator. However, the beam intensity is greatest at the surface proximal to the source both because that surface is closest to the source and because the attenuation of the scintillator itself reduces the beam intensity as it passes through the detector. Therefore, the most interactions occur at the proximal surface of the scintillator. For this reason, increasing the scintillator thickness moves more of the photon interactions further from the photodiode and increases the chance that the optical photons will be self-absorbed by the crystal or absorbed by the septa before they reach the photodiode. This variation in the amount of optical photons reaching the optical detector, as a function of the depth of emission in the scintillator, is referred to as the optical component of Swank noise and degrades the DQE [Wang, et al. 2009]. Therefore, although increasing the thickness will increase the probability of photon interactions, the gain is partially offset by the increase in Swank noise.

Nonetheless, the Monte Carlo studies show that 1 mm pitch detectors used in conjunction with septa of reflectivity greater than 0.975 will continue to see significant increases in DQE at least up to a thickness of 30 mm [Monajemi, et al. 2006 (1)]. For cost and practical considerations, our group has not used scintillators more than 10 mm thick.

A prototype imaging system was constructed using thick, segmented cadmium tungstate detectors [Monajemi, et al. 2006 (2); Rathee, et al. 2006]. That system used a single row of relatively large (2.75 mm x 8 mm pitch x 10 mm thickness) scintillating elements, each coupled to two photodiodes. That system had a zero frequency DQE on the order of 19% for a 6 MV photon beam, and it showed an ability to image objects having 1.5% contrast using 2 cGy dose in a ^{60}Co beam, with a DQE reaching 26%. It also demonstrated that the detector signal was only slightly affected by radiation damage, dropping approximately 1% after 25 Gy dose delivered and recovering that to within measurement error by the next day. However, the resolution was understandably poor because of the large detector pitch as well as the large size of the cobalt source. Also, that system was not tested with higher energy linacs that are much more frequently used in modern radiation therapy.

2.2.3 Current MVCT Prototype

The current prototype MVCT system evaluated in this thesis is based on the same technology as the previous system developed at the Cross Cancer Institute. It also employs cadmium tungstate photodiode detectors. However, for the current system the crystals have much smaller pitch, 1 mm x 1 mm, with a thickness of 10 mm. This gives the system superior spatial resolution compared with the previous system. The new prototype also has 16 rows of detectors instead of one, allowing it to be used for multi-slice imaging. The accompanying data acquisition system is optimized for use with a linac, allowing the system to be evaluated using the 6 MV beams commonly available on modern radiation treatment units. This prototype system is described in greater detail in Chapter 3.

2.3 Imaging Performance Tests

There are several tests which are commonly used to evaluate the performance of a tomographic imaging system. These tests focus on various aspects of imaging performance that are necessary in order for an imaging system to provide clinically useful data. [Bushberg, et al. 2002 p. 255] The current prototype MVCT system was evaluated based on as many of these performance tests as possible.

2.3.1 Uniformity

In order for an imaging system to yield quantitatively accurate data, it must be able to display uniform pixel values across an image of a uniform phantom. The presence of non-uniformity would mean that a given feature would appear different depending on where in the image it is located,

which would make it more difficult to interpret the images, as well as making it difficult to carry out accurate dose calculations.

There are many ways in which the uniformity of an image can be quantified. One way is to select several regions of interest (ROIs) on the reconstructed image of a uniform phantom, and measure the mean linear attenuation coefficient, μ , of each one. The uniformity index can then be defined as a percentage by Equation 2.2 [Meeks, et al. 2005], where μ_{\max} is the mean of the ROI with the highest mean and μ_{\min} is the mean of the ROI with the lowest mean.

$$\text{uniformity index} = 100 \left(1 - \frac{\mu_{\max} - \mu_{\min}}{\mu_{\max} + \mu_{\min}} \right) \quad (2.2)$$

Another way to quantify the uniformity of an image is to calculate the mean of several ROIs at the periphery of the phantom and calculate the maximum difference between them and an ROI placed at the centre of the image. This can also be expressed as a percentage as shown in Equation 2.3, where μ_{central} is the mean of a ROI placed at the centre of the phantom on the reconstructed image and μ_{\max} is the mean of the ROI that has the largest *difference* from the central ROI (μ_{\max} can be more or less than μ_{central}).

$$\text{uniformity difference} = 100 \frac{|\mu_{\max} - \mu_{\text{central}}|}{\mu_{\text{central}}} \quad (2.3)$$

2.3.2 Signal to Noise Ratio

The SNR in the images provided by a system is an important indicator of how well the system distinguishes features in the phantom being imaged from the background noise. Theoretically, The SNR at the center of a uniform object has been shown [Barrett, et al. p.534] to be:

$$SNR(0,0) = \frac{\mu_0}{\sqrt{\frac{M}{n_0} e^{2\mu_0 R_{obj}} \int_{-\infty}^{\infty} q_1^2(x_r') dx_r'}} \quad (2.4)$$

where:

μ_0 is the linear attenuation coefficient;

M is the number of projections collected over an angle of π radians;

n_0 is the number of incident photons;

R_{obj} is the radius of the object;

q_1 is an approximation to the impulse response function of the filter being used for back-projection;

The denominator in Equation 2.4 represents the variance, assuming that all noise is a result of photon counting statistics. If there is another source of noise, such as electronic noise, it would add another term to the variance. In the case where the electronic noise is insignificant compared to the photon counting noise, it has been shown [Barrett, et al. p.537] that the dose D is given by Equation 2.5:

$$D = \frac{2.26\mu_{en} E_x e^{\mu_0 R_{obj}} SNR^2(0,0)}{\eta\rho\Delta_z\mu_0^2\partial^3} \quad (2.5)$$

which includes the new variables:

E_x is the photon energy;

η is the detector efficiency;

ρ is the density of the medium;

Δ_z is the slice thickness;

∂^3 is full width at half maximum, a measure of the detector resolution.

Equation 2.5 shows that dose is proportional to the square of the SNR. Also noteworthy is the strong dependence between dose and object radius, meaning that larger patients need to be subjected to larger doses in order to be imaged at the same noise level.

The SNR can be measured according to Equation 2.6 using a reconstructed image of a uniform phantom, where μ is the mean of an ROI and σ is the standard deviation of that ROI. To reduce the uncertainty in the calculation of μ and σ , the ROI can be chosen to be as large as possible.

$$SNR = \frac{\mu}{\sigma} \quad (2.6)$$

As shown previously, a plot of SNR^2 vs. dose is expected to be a linear curve. However, the presence of electronic noise could be detected by non-linearity in the SNR^2 vs. dose curve that would appear worse at lower dose.

2.3.3 High Contrast Resolution

A MVCT system must provide adequate spatial resolution in order to visualize a patient's anatomy for setup purposes. The resolution of a system is limited by the size of each detector element, however in practice the resolution is even lower due to other factors. The larger the photon source, the lower the resolution will be. Any photon scatter in the phantom or the detector lowers the resolution. In a scintillating detector, the spreading of optical photons also reduces resolution.

Resolution is often characterized by the modulation transfer function (MTF) which provides the signal response of a system as a function of the spatial frequency, usually given in line pairs per unit distance (e.g. lp/cm). The MTF is normalized to 1 at zero spatial frequency and always approaches zero at infinite spatial frequency, since no real imaging system has unlimited resolution. The MTF is related to the line spread function (LSF), which is the response of the system to an input given as an infinitesimally thin line. In a circularly symmetrical system, the LSF can be used to completely characterize the detector response.

There are two common ways to measure the MTF of a CT system. One is to measure the line spread function by imaging a phantom containing a very thin wire of a very high contrast material compared to the rest of the phantom. However, such phantoms are typically optimized for kVCT systems that offer superior contrast and resolution to MVCT, and no

phantoms were available that contained a wire that could be resolved by the experimental MVCT system described in this thesis.

The other way of experimentally measuring the MTF uses a bar phantom [Droege, et al. 1982]. The phantom contains high contrast metal bars that, combined with the background material, comprise line pairs of known spatial frequency. Based on the modulation at a given frequency, $M(f)$, and the input modulation, M_0 , the MTF can be calculated according to Equation 2.7, where f_c is the cutoff frequency above which the MTF is 0.

$$MTF(f) = \frac{\pi\sqrt{2}}{4} \frac{M(f)}{M_0} \quad f \geq \frac{f_c}{3} \quad (2.7)$$

$M(f)$ is equivalent to the standard deviation of a ROI containing bar pairs of frequency f , corrected for noise as per Equation 2.8, where M' is the uncorrected standard deviation, and N is the standard deviation of a uniform ROI.

$$M = \sqrt{M'^2 - N^2} \quad (2.8)$$

The input modulation, M_0 , is given by Equation 2.9, where CT_1 is the mean pixel value of the line material (i.e. the metal bar) and CT_2 is the mean pixel value of the background material.

$$M_0 = \frac{|CT_1 - CT_2|}{2} \quad (2.9)$$

Unfortunately, the Droege method of calculating MTF runs up against several obstacles when applied to the prototype MVCT system. This method cannot calculate the MTF for frequencies below $\frac{1}{3}$ of the cutoff

frequency of the system. Since the available bar phantoms have 21 line pairs ranging in unit increments from 1 to 21 lp/cm, and the cutoff frequency is relatively low, around 6 lp/cm, only four bar pairs can be used with this method. In addition, the relatively low resolution of the system makes it difficult to measure the input modulation without substantial error, since even the largest metal bars are represented on the images by only a few pixels.

For these reasons, the resolution of the experimental MVCT system is only evaluated qualitatively by examining images of a bar phantom and estimating how many line pairs per centimeter can be resolved.

2.3.4 Low Contrast Definition

In order to visualize soft tissues, a MVCT system must be capable of differentiating between small differences in electron density. This is referred to in this thesis as the low contrast definition (LCD). The LCD is dependent on both the difference in electron density between an object to be visualized and the background, and the size of that object, with larger objects being easier to detect.

The LCD can be assessed visually by examining reconstructed images of a phantom containing plugs of variable contrast and size and determining whether each one is discernible. For a quantitative evaluation, the contrast to noise ratio (CNR) can be used. The CNR is defined by Equation 2.10 where μ_b and μ are the background and target mean pixel values and σ_b is the background standard deviation, which is taken to be similar to the target standard deviation. Since the noise is inversely proportional to the square of the dose, CNR can be expected to increase linearly with the square of the dose.

$$CNR = \frac{\mu - \mu_b}{\sigma_b} \quad (2.10)$$

LCD can also be assessed qualitatively. Typically an observer examines an image of a uniform phantom containing inserts of variable size and contrast, then makes a judgment as to which ones are observable.

2.3.5 CT Number Linearity

The pixel values of a CT image resulting from filtered back-projection image reconstruction are arbitrarily scaled attenuation coefficients of the pixels. The measured linear attenuation coefficient of various tissues is dependent upon the photon spectrum used in imaging. As a result, the contrast among tissue types also depends on the spectrum, making it difficult to compare an image taken with one CT scanner to that taken with another. In order to circumvent this problem to some extent, the displayed pixels in CT images are normalized with respect to water. The normalized pixels are typically calibrated to Hounsfield units [Hounsfield, 1973], also known as CT numbers. On the Hounsfield scale, water has a value of 0, while vacuum (zero attenuation) has a value of -1000 and a material with twice the attenuation of water has a value of +1000. The conversion from attenuation coefficients to Hounsfield units is given by Equation 2.11, where μ_x is the attenuation coefficient of the material in a given pixel x .

$$HU_x = 1000 \frac{\mu_x - \mu_{H_2O}}{\mu_{H_2O}} \quad (2.11)$$

Since the attenuation coefficients of water and soft tissue are expected to vary with energy in a similar manner, the CT numbers of various organs are relatively insensitive to small changes in the photon beam spectrum used for imaging.

For the purposes of this thesis, the actual calibration of Equation (2.10) was not performed. Instead, the linearity of the pixel values as a function of electron density in non-calibrated images was measured. If a system's raw pixel values increase linearly with electron density, the final calibrated values will do the same. As previously mentioned, at kV energies the attenuation of a beam is not strictly a function of electron density, but is also affected by the atomic number of a material. For this reason it is expected that a MVCT system will deliver a more linear response of pixel value vs. electron density.

References

Almond, P. R., Biggs, P. J., Coursey, B. M., Hanson, W. F., Huq, M. S., Nath, R. & Rogers, D. W. O. AAPM's TG-51 protocol for clinical reference dosimetry of high-energy photon and electron beams. *Medical physics* 26, 1847-1870 (1999).

Antonuk, L. E. Electronic portal imaging devices: A review and historical perspective of contemporary technologies and research. *Physics in Medicine and Biology* 47, R31-R65 (2002).

Azevedo, S. G., Martz, H. E. & Schneberk, D. J. *Potential of computed tomography for inspection of aircraft components* (1993).

Barrett & Swindell. in *Radiological Imaging* (Academic Press, San Diego, California, 1981).

Bendahan, J. & Garms, W. *Megavolt computed tomography for air cargo container inspection*, (2008).

Brahme, A., Lind, B. & Nafstadius, P. Radiotherapeutic computed tomography with scanned photon beams. *International Journal of Radiation Oncology Biology Physics* 13, 95-101 (1987).

Bushberg, J. T., Seibert, J. A., Leidholdt, E. M. & Boone, J. M. in *The Essential Physics of Medical Imaging* (2002).

Cho, P. S., Johnson, R. H. & Griffin, T. W. Cone-beam CT for radiotherapy applications. *Physics in Medicine and Biology* 40, 1863-1883 (1995).

Cremers, F., Frenzel, T., Kausch, C., Albers, D., Schonborn, T. & Schmidt, R. Performance of electronic portal imaging devices (EPIDs) used in radiotherapy: image quality and dose measurements. *Medical physics* 31, 985-996 (2004).

Droege, R. T. & Morin, R. L. A practical method to measure the MTF of CT scanners. *Medical physics* 9, 758-760 (1982).

El-Mohri, Y., Jee, K. W., Antonuk, L. E., Maolinbay, M. & Zhao, Q. Determination of the detective quantum efficiency of a prototype, megavoltage indirect detection, active matrix flat-panel imager. *Medical physics* 28, 2538-2550 (2001).

Faddegon, B. A., Wu, V., Pouliot, J., Gangadharan, B. & Bani-Hashemi, A. Low dose megavoltage cone beam computed tomography with an unflattened 4 MV beam from a carbon target. *Medical physics* 35, 5777-5786 (2008).

Flynn, R. T., Hartmann, J., Bani-Hashemi, A., Nixon, E., Alfredo, R., Siochi, C., Pennington, E. C. & Bayouth, J. E. Dosimetric characterization and application of an imaging beam line with a carbon electron target for megavoltage cone beam computed tomography. *Medical physics* 36, 2181-2192 (2009).

Ford, E. C., Chang, J., Mueller, K., Sidhu, K., Todor, D., Mageras, G., Yorke, E., Ling, C. C. & Amols, H. Cone-beam CT with megavoltage beams and an amorphous silicon electronic portal imaging device: Potential for verification of radiotherapy of lung cancer. *Medical physics* 29, 2913-2924 (2002).

Galbraith, D. M. Low-energy imaging with high-energy bremsstrahlung beams. *Medical physics* 16, 734-746 (1989).

Gayou, O., Parida, D. S., Johnson, M. & Miften, M. Patient dose and image quality from mega-voltage cone beam computed tomography imaging. *Medical physics* 34, 499-506 (2007).

Groh, B. A., Siewerdsen, J. H., Drake, D. G., Wong, J. W. & Jaffray, D. A. A performance comparison of flat-panel imager-based MV and kV cone-beam CT. *Medical physics* 29, 967-975 (2002).

Guanf, H. & Zhu, Y. Feasibility of megavoltage portal CT using an electronic portal imaging device (EPID) and a multi-level scheme algebraic reconstruction technique (MLS-ART). *Physics in Medicine and Biology* 43, 2925-2937 (1998).

Hesse, B. M., Spies, L. & Groh, B. A. Tomotherapeutic portal imaging for radiation treatment verification. *Physics in Medicine and Biology* 43, 3607-3616 (1998).

Hong, T. S., Welsh, J. S., Ritter, M. A., Harari, P. M., Jaradat, H., Mackie, T. R. & Mehta, M. P. Megavoltage computed tomography: an emerging tool for image-guided radiotherapy. *American journal of clinical oncology* 30, 617-623 (2007).

Hounsfield, G. N. Computerized transverse axial scanning (tomography): I. Description of system. *British Journal of Radiology* 46, 1016-1022 (1973).

Jaffray, D. A. & Siewerdsen, J. H. Cone-beam computed tomography with a flat-panel imager: Initial performance characterization. *Medical physics* 27, 1311-1323 (2000).

Johns H.E. & Cunningham J.R. in *The Physics of Radiology* (Thomas, Springfield, IL, 1983).

Keall, P. J., Chock, L. B., Jeraj, R., Siebers, J. V. & Mohan, R. Image reconstruction and the effect on dose calculation for hip prostheses. *Medical Dosimetry* 28, 113-117 (2003).

Kijewski, P. K. & Bjarngard, B. E. The use of computed tomography data for radiotherapy dose calculations. *International Journal of Radiation Oncology Biology Physics* 4, 429-435 (1978).

Kobayashi, M., Ishii, M., Usuki, Y. & Yahagi, H. Cadmium tungstate scintillators with excellent radiation hardness and low background. *Nuclear Inst. and Methods in Physics Research, A* 349, 407-411 (1994).

Mackie, T. R., Balog, J., Ruchala, K., Shepard, D., Aldridge, S., Fitchard, E., Reckwerdt, P., Olivera, G., McNutt, T. & Mehta, M. Tomotherapy. *Seminars in radiation oncology* 9, 108-117 (1999).

Mackie, T. R., Kapatoes, J., Ruchala, K., Lu, W., Wu, C., Olivera, G., Forrest, L., Tome, W., Welsh, J., Jeraj, R., Harari, P., Reckwerdt, P., Paliwal, B., Ritter, M., Keller, H., Fowler, J. & Mehta, M. Image guidance for precise conformal radiotherapy. *International Journal of Radiation Oncology Biology Physics* 56, 89-105 (2003).

Meeks, S. L., Harmon, J. F., Jr, Langen, K. M., Willoughby, T. R., Wagner, T. H. & Kupelian, P. A. Performance characterization of megavoltage computed tomography imaging on a helical tomotherapy unit. *Medical physics* 32, 2673-2681 (2005).

Mei, X., Rowlands, J. A. & Pang, G. Electronic portal imaging based on Cerenkov radiation: A new approach and its feasibility. *Medical physics* 33, 4258-4270 (2006).

Midgley, S., Millar, R. M. & Dudson, J. A feasibility study for megavoltage cone beam CT using a commercial EPID. *Physics in Medicine and Biology* 43, 155-169 (1998).

Monajemi, T. T., Fallone, B. G. & Rathee, S. Thick, segmented CdWO₄-photodiode detector for cone beam megavoltage CT: a Monte Carlo study of system design parameters. *Medical physics* 33, 4567-4577 (2006).

Monajemi, T. T., Steciw, S., Fallone, B. G. & Rathee, S. Modeling scintillator-photodiodes as detectors for megavoltage CT. *Medical physics* 31, 1225-1234 (2004).

Monajemi, T. T., Tu, D., Fallone, B. G. & Rathee, S. A bench-top megavoltage fan-beam CT using CdWO₄-photodiode detectors. II. Image performance evaluation. *Medical physics* 33, 1090-1100 (2006).

Morin, O., Aubry, J. -, Aubin, M., Chen, J., Descovich, M., Hashemi, A. - & Pouliot, J. Physical performance and image optimization of megavoltage cone-beam CT. *Medical physics* 36, 1421-1432 (2009).

Morin, O., Gillis, A., Chen, J., Aubin, M., Bucci, M. K., Roach, M., 3rd & Pouliot, J. Megavoltage cone-beam CT: system description and clinical applications. *Medical dosimetry : official journal of the American Association of Medical Dosimetrists* 31, 51-61 (2006).

Morin, O., Gillis, A., Descovich, M., Chen, J., Aubin, M., Aubry, J., Chen, H., Gottschalk, A. R., Xia, P. & Pouliot, J. Patient dose considerations for routine megavoltage cone-beam CT imaging. *Medical physics* 34, 1819-1827 (2007).

Mosleh-Shirazi, M. A., Evans, P. M., Swindell, W., Webb, S. & Partridge, M. A cone-beam megavoltage CT scanner for treatment verification in conformal radiotherapy. *Radiotherapy and Oncology* 48, 319-328 (1998).

Nakagawa, K., Aoki, Y., Akanuma, A., Onogi, Y., Terahara, A., Sakata, K., Muta, N., Sasaki, Y., Kawakami, H. & Hanakawa, K. Real-time beam monitoring in dynamic conformation therapy. *International Journal of Radiation Oncology Biology Physics* 30, 1233-1238 (1994).

Nakagawa, K., Aoki, Y., Akanuma, A., Sakata, K., Karasawa, K., Terahara, A., Onogi, Y., Hasezawa, K. & Sasaki, Y. Technological features and clinical feasibility of megavoltage CT scanning. *European radiology* 2, 184-189 (1992).

Ostapiak, O. Z., O'Brien, P. F. & Faddegon, B. A. Megavoltage imaging with low Z targets: Implementation and characterization of an investigational system. *Medical physics* 25, 1910-1918 (1998).

Parker, R. P., Hobday, P. A. & Cassell, K. J. The direct use of CT numbers in radiotherapy dosage calculations for inhomogeneous media. *Physics in Medicine and Biology* 24, 802-809 (1979).

Ramachandran, G. N. & Lakshminarayanan, A. V. Three-dimensional reconstruction from radiographs and electron micrographs: application of convolutions instead of Fourier transforms. *Proceedings of the National*

Academy of Sciences of the United States of America 68, 2236-2240 (1971).

Rathee, S., Tu, D., Monajemi, T. T., Rickey, D. W. & Fallone, B. G. A bench-top megavoltage fan-beam CT using CdWO₄-photodiode detectors. I. System description and detector characterization. *Medical physics* 33, 1078-1089 (2006).

Ruchala, K. J., Olivera, G. H., Kapatoes, J. M., Scloesser, E. A., Reckwerdt, P. J. & Makie, T. R. Megavoltage CT image reconstruction during tomotherapy treatments. *Physics in Medicine and Biology* 45, 3545-3562 (2000).

Ruchala, K. J., Olivera, G. H., Schloesser, E. A., Hinderer, R. & Mackie, T. R. Calibration of a tomotherapeutic MVCT system. *Physics in Medicine and Biology* 45, N27-36 (2000).

Ruchala, K. J., Olivera, G. H., Schloesser, E. A. & Mackie, T. R. Megavoltage CT on a tomotherapy system. *Physics in Medicine and Biology* 44, 2597-2621 (1999).

Samant, S. S., Gopal, A., Jain, J., Xia, J. & DiBianca, F. A. Design of a prototype tri-electrode ion-chamber for megavoltage X-ray imaging. *Nuclear Instruments and Methods in Physics Research, Section A: Accelerators, Spectrometers, Detectors and Associated Equipment* 573, 398-409 (2007).

Sawant, A., Antonuk, L. E., El-Mohri, Y., Li, Y., Su, Z., Wang, Y., Yamamoto, J., Zhao, Q., Du, H., Daniel, J. & Street, R. Segmented phosphors: MEMS-based high quantum efficiency detectors for megavoltage x-ray imaging. *Medical physics* 32, 553-565 (2005).

Schulz, R. J., Almond, P. R. & Cunningham, J. R. A protocol for the determination of absorbed dose from high-energy photon and electron beams. *Medical physics* 10, 741-771 (1983).

Seco, J. & Evans, P. M. Assessing the effect of electron density in photon dose calculations. *Medical physics* 33, 540-552 (2006).

Simpson, R. G., Chen, C. T., Grubbs, E. A. & Swindell, W. A 4-MV CT scanner for radiation therapy: The prototype system. *Medical physics* 9, 574-579 (1982).

Smith-Bindman, R., Lipson, J., Marcus, R., Kim, K. -, Mahesh, M., Gould, R., Berrington De González, A. & Miglioretti, D. L. Radiation dose associated with common computed tomography examinations and the

associated lifetime attributable risk of cancer. *Archives of Internal Medicine* 169, 2078-2086 (2009).

Stutzel, J., Oelfke, U. & Nill, S. A quantitative image quality comparison of four different image guided radiotherapy devices. *Radiotherapy and oncology : journal of the European Society for Therapeutic Radiology and Oncology* 86, 20-24 (2008).

Swindell, W., Simpson, R. G. & Oleson, J. R. Computed tomography with a linear accelerator with radiotherapy applications. *Medical physics* 10, 416-420 (1983).

Wang, Y. et al. *Theoretical investigation of very high quantum efficiency, segmented, crystalline detectors for low-contrast visualization in megavoltage cone-beam CT* Ser. 6142 II, (2006).

Wang, Y., Antonuk, L. E., El-Mohri, Y. & Zhao, Q. A Monte Carlo investigation of Swank noise for thick, segmented, crystalline scintillators for radiotherapy imaging. *Medical physics* 36, 3227-3238 (2009).

Wang, Y., Antonuk, L. E., El-Mohri, Y., Zhao, Q., Sawant, A. & Du, H. Monte Carlo investigations of megavoltage cone-beam CT using thick, segmented scintillating detectors for soft tissue visualization. *Medical physics* 35, 145-158 (2008).

Wei, J., Sandison, G. A., Hsi, W. -, Ringor, M. & Lu, X. Dosimetric impact of a CT metal artefact suppression algorithm for proton, electron and photon therapies. *Physics in Medicine and Biology* 51, 5183-5197 (2006).

Zubal, I. G., Harrell, C. R., Smith, E. O., Rattner, Z., Gindi, G. & Hoffer, P. B. Computerized three-dimensional segmented human anatomy. *Medical physics* 21, 299-302 (1994).

Chapter 3: MATERIALS AND METHODS

This chapter describes the hardware and software components of the prototype MVCT system. The detector system is described in detail along with scintillator properties and its coupling with the photodiode array. Synchronization of the data acquisition with the pulsed radiation beam is required to read every radiation pulse separately. On a clinical linac, the user does not have control over dose per pulse. As a result, it was felt that a conventional 6 MV clinical photon beam could not be used to test the MVCT system performance at low radiation dose. Thus, this chapter describes a unique method of using very low intensity Bremsstrahlung radiation produced by the clinical 6 MeV electron beam for imaging purposes. The characteristics of this Bremsstrahlung beam were studied using both measurements and Monte Carlo simulation. The phantoms imaged on the prototype system were also imaged on a TomoTherapy system in order to allow comparisons with a commercial MVCT system. Finally, the data processing methods used to correct for beam hardening and errors due to small air gaps between detector blocks are described, along with the particular implementation of filtered back-projection used for image reconstruction.

3.1 System Description

The prototype MVCT system described in this chapter consists of a focused array of cadmium tungstate scintillators. Each scintillator is optically isolated from the others and optically coupled to a photodiode array. The photodiode array in turn is connected to a data acquisition system (DAS) via long cables. The DAS is controlled by specially written software. Phantoms being imaged are placed on a rotating stage between the source and detectors.

3.1.1 Detectors

The prototype MVCT system used in these experiments consists of a 2D array of 1 mm x 1 mm (pitch) x 10 mm (thickness) Cadmium Tungstate (CdWO_4) detectors arranged in a 320 x 16 detector arc (Fig. 3.1). These detectors are mounted as twenty 16 x 16 detector blocks (SCA-CA256ES, Semicoa, Costa Mesa, CA). Each block is attached to a 16 x 16 photodiode array by optical glue. The signal from the photodiodes is then read out by the DAS (Analogic Corporation, Peabody, OH)



Figure 3.1: A 2D array (320 x 16) of 1 x 1 x 10 mm³ CdWO_4 scintillators is arranged in an arc of radius 92.5 cm. Each of the twenty 16 x 16 array blocks is mounted on a 2D photodiode array. The arrays are mounted on long printed circuit boards which are connected to the data acquisition system (DAS) via long cables (not shown) to reduce the scattered radiation reaching the electronics in the DAS.

3.1.1.1 Cadmium Tungstate Scintillator

Cadmium tungstate has several properties that combine to make it a good choice of scintillation material for megavoltage photon detection. It has a density of 7.9 g/cm^3 , an average atomic number of 64, and an optical yield of 20,000 photons per MeV absorbed. It also is relatively unaffected by ionizing radiation and has low optical absorption [Kobayashi, et al. 1994]. In a previous study, cadmium tungstate crystals of 10 mm thickness were found to have a detective quantum efficiency (DQE) of 19% in a 6MV beam and 26% in a ^{60}Co beam [Monajemi, et al. 2004].

During imaging, the cadmium tungstate detectors are covered by black paper to prevent optical photons, such as those from room lighting, from entering the detectors and contributing noise to the system. This also eliminates one source of experimental setup variation.

3.1.1.2 Septa

In the scintillation process, the optical photons are produced in isotropic directions and then travel towards the optical detector. The purpose of the septa is two fold. Firstly, they are required to geometrically constrain all the optical photons within the detection element in which they are produced. This improves the spatial resolution as the crystal height is increased by preventing the signal spread from one detection element to another. This task requires the septa material to have very high opacity. Secondly, the optical photons traveling down the scintillation crystal will reflect many times at the septa surfaces. If the reflectivity of the septa surfaces is poor, a great number of photons will be lost in the septa and the optical transfer from the scintillation material to the photodiode will become highly

dependent on depth in the material at which scintillation events take place (optical Swank noise).

It has been shown that septa made from high atomic number materials (i.e. Tungsten) which maintain high transparency and reflectivity also counteract the loss of DQE due to the replacement of scintillation material with the septa material. Fill factor is usually defined as the fraction of the active detector area in each detection element. Each 1 mm x 1 mm x 10 mm detector in the present system consists of a cadmium tungstate crystal of dimensions 0.85 mm x 0.85 mm x 10 mm surrounded on all sides by 0.075 mm septa. The septa consist of a white paint of reflectivity greater than 0.975 and serve to optically isolate each detector element from its neighbors, thereby reducing Swank noise. This gives a cadmium tungstate fill factor of 72%. Compared to a theoretical system with a 100% fill factor and no optical loss, the lower fill factor has been shown in Monte Carlo simulations to reduce the DQE from 20% to 14.5% in a 6MV beam, assuming the septa to be made of polystyrene having a reflectivity of 0.975 [Monajemi, et al. 2006 (2)].

3.1.1.3 Detector Block Focusing

The twenty detector blocks are tiled in 2D along an arc of a circle focused to a point 92.5 cm away from any detector. This distance is set by the geometry of the flex-rigid cable-connector system that connects the detector blocks to the DAS. This eliminates the substantial effect of beam divergence on the detector resolution [Monajemi, et al. 2004].

3.1.1.4 Photodiode and Optical Coupling

The 16 x 16 photodiode arrays are based on crystalline silicon technology. They are optically coupled to the detector blocks by optical glue that matches the refractive indices of the scintillating material and the glass window of the photodiode. If r_1 , r_2 and r_3 are the refractive indices of scintillation material, optical glue, and photodiode respectively, then:

$$r_2 = \sqrt{r_1 * r_3} \quad (3.1)$$

This refractive index is chosen because according to Fresnel's equations, the fraction of light transmitted, T , at a boundary from one medium 1 to medium 2 is, assuming normal incidence, given by Equation 3.2.

$$T_{12} = \frac{4r_1r_2}{(r_1 + r_2)^2} \quad (3.2)$$

We can then calculate the fraction of light passing from medium 1 to medium 2 and through to medium 3 by Equation 3.3.

$$T_{13} = T_{12}T_{23} = \frac{4r_1r_2}{(r_1 + r_2)^2} \frac{4r_2r_3}{(r_2 + r_3)^2} \quad (3.3)$$

The maximum transmission in Equation 3.3 can be found by calculating the derivative and setting it to zero. In so doing, it is shown that the value for r_2 given by Equation 3.1 produces the maximum transmission and is therefore the ideal refractive index for a coupling glue.

3.1.1.5 Radiation Damage vs Detector Response

The effects of radiation on the cadmium tungstate crystals and photodiodes were not investigated for this system. However, an investigation of a previous cadmium tungstate detector system using similar photodiodes found that the output signal from the photodiodes dropped less than 1% after 25 Gy of dose delivered. The signal was recovered within experimental error by the following day. Thus the detector exhibits some short-term loss of signal due to accumulated radiation damage. However, this is not a major issue and was mitigated by obtaining air scans two or more times a day to correct for the loss of signal.

3.1.2 Data Acquisition System

The DAS was custom designed by Analogic Corporation (Imaging Subsystems Division, Peabody, MA). It is designed to collect data at either 180 or 360 Hz with an integration time of 333 μ s. The DAS has 10 analog to digital converter boards (ADCs). It has a total of 11,328 output channels. A total of 5,120 channels are used for the photodiode output (320 detectors per slice times 16 slices is 5,120 detectors) and 6,144 channels are currently unused (they could be used for more detectors). The remaining 64 channels are reserved for diagnostic information such as DAS temperature, voltage, fan speed, etc (some of these channels are unused as well).

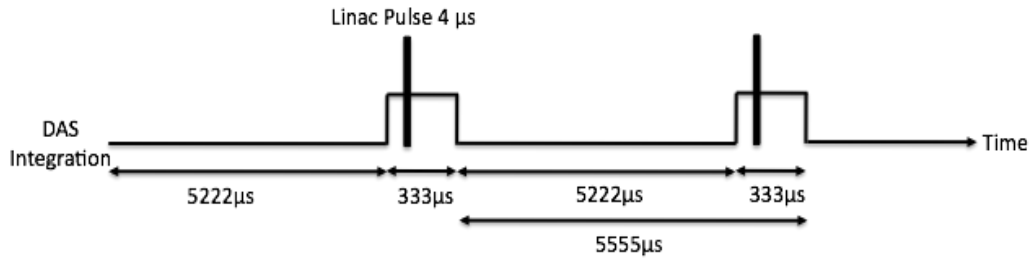


Figure 3.2: The timings for the DAS when running at 180 Hz as per Analogic Corporation documentation. The DAS integrates for only a small portion of each cycle, which measures the signal produced by a single linac pulse.

3.1.2.1 Sync Pulse

The DAS synch input is attached via a coaxial cable to the sync pulse of a linac. This allows for the synchronization of the DAS integration phase of to the radiation pulse of the linac. Therefore, exactly one pulse of radiation is integrated per cycle of the DAS, and each pulse of radiation produced by the linac is read out separately.

3.1.2.2 Long Cables

If the DAS were directly exposed to a megavoltage photon beam, irreparable damage is a probable result as the electronics are based on commercial crystalline silicon. To prevent this, the DAS is connected to the photodiodes via long cables. The DAS itself is positioned well outside the radiation field of the photon beam.

3.1.3 Rotating Stage

In this system, the photon source and detectors remain fixed, while the phantom being imaged is rotated on a 15 cm diameter precision rotating stage (200RT, Daedal Division, Parker Hannifin Corp., Irwin, PA). The

stage is rotated by a stepper motor (ZETA57-83, Compumotor Division, Parker Hannifin Corp, Rohnet Park, CA). It takes 15.5 seconds for the stage to complete one rotation, so for a linac with a pulse rate of 180 Hz, 2790 pulses (i.e. projections) can be acquired per rotation. During imaging the stage is placed as far as possible from the detector array to minimize the amount of phantom scatter reaching the detectors.

3.1.3.1 Rotating Stage Centering

It is critical that the rotating stage be centered along the axis that joins the photon beam source to the centre of the detector array. Even an offset from this axis by the width of a single detector (less than one millimeter) will cause visible centre of rotation artifacts [Gullberg, et al. 1986] on the final image (Figure 3.3). During experiments, every effort was made to centre the stage as precisely as possible.

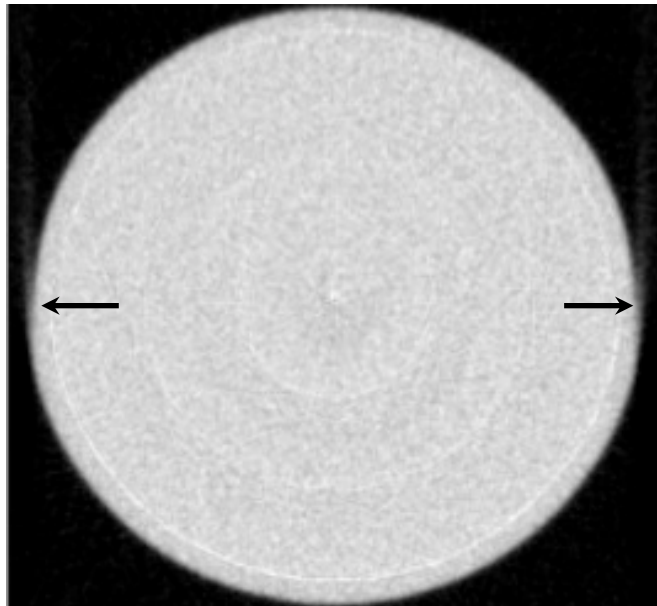


Figure 3.3: Uniform phantom image showing a centering artifact. The lower portion of the phantom appears to bulge and vertical streaks are seen. The effect is most apparent at the left and right sides denoted by arrows.

By placing a thin vertical metal wire in the centre of the rotating stage, the stage was centered visually by lining up the shadow produced by the linac light field with the centre of the detector array. However, the shadow of the wire has a small thickness and penumbra that often causes this method of centering to be unsuccessful on its own.

To further aid in stage centering, the image of a uniform phantom placed on the rotating stage was reconstructed using only the minimum number of projections required for fan beam geometry, 180° plus the fan angle, in this case 200° worth of projections. Two images were then acquired with the rotating stage at starting positions of 0° and 180° respectively. The centroid of each reconstructed image was then calculated using MATLAB software (The MathWorks, Natick, Massachusetts). If the stage is perfectly centered, the centroid will be the same for both images. However, if there is any centering error the centroids will be different i.e. the two images will not superimpose exactly over each other.

3.1.4 LabView Software

The DAS and rotating stage are controlled via a software program written in LabVIEW (Version 6i, National Instruments, Austin, Texas). This software allows for the user to control the number of projections collected, to start and stop the rotating stage, to save the data from the detectors, and to view diagnostic information from the DAS.

3.2 6 MeV Imaging Beam

Experiments using a 6MV linac have shown that the estimated dose required for imaging a phantom using even the minimum 200° of rotation is in excess of 60 cGy. This dose is far too much to be used in daily *in vivo* imaging such as would be necessary to verify the patient setup prior to external beam radiation therapy. This is primarily because treatment linacs are designed to have as high a dose per pulse as practical in order to reduce treatment times. While our linacs do allow the user to control the dose rate, this is done by preventing some of these pulses from producing radiation (pulse dropping), not by reducing the amount of radiation in a given pulse. The imaging dose could be reduced artificially by throwing away the data from some radiation pulses (or causing the linac to drop pulses) and reconstructing an image with the remaining pulses. However, because the linac's pulses are extremely short in duration (see Figure 3.2), the use of a reduced number of pulses, for example one pulse per degree of rotation, does not average the projection data over that one degree angular interval, but rather gives an instantaneous projection. This results in visible artifacts long before the desired cumulative dose range of 2 cGy or less is achieved (Figure 3.4). Therefore, a better method of achieving an imaging beam with reduced dose was required.

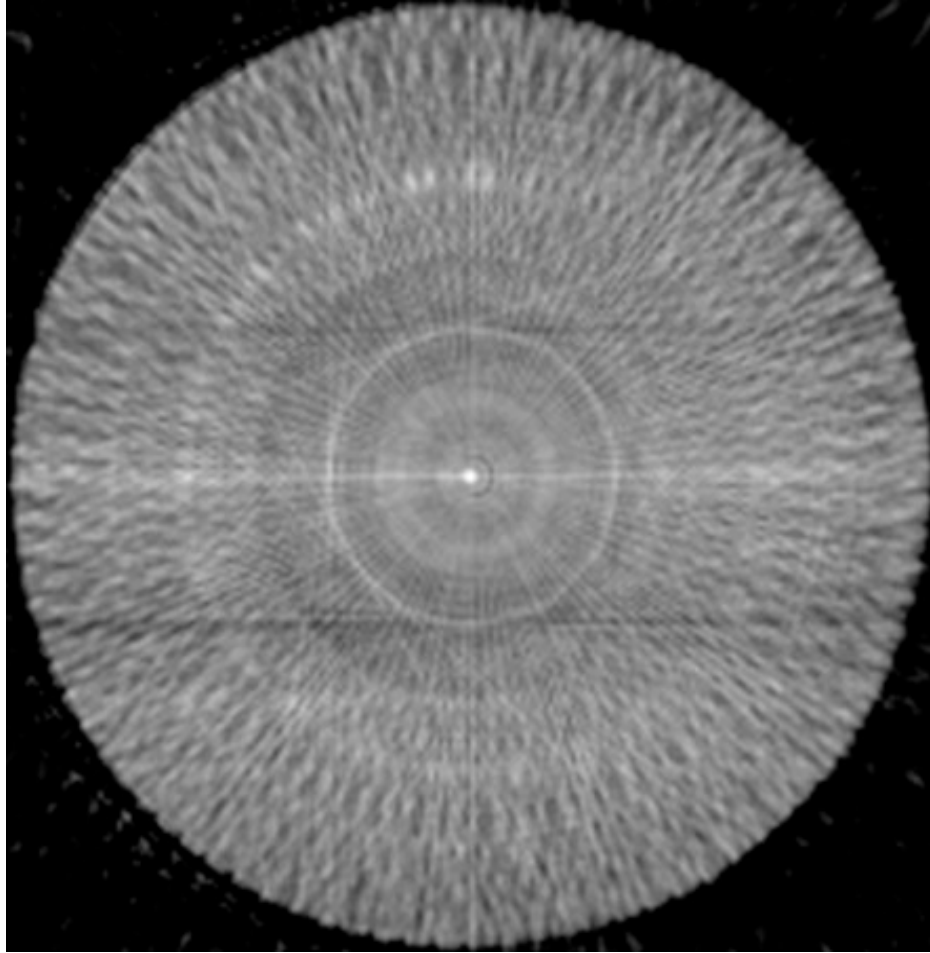


Figure 3.4: A bar phantom imaged with a 6 MV treatment beam. 90% of the pulses were dropped, resulting in just under one pulse being collected per degree of rotation. The dose delivered to produce this image is estimated to be around 6 cGy.

Since it was not possible to reduce the electron gun current on a working clinical linac, the experimental MVCT system was instead tested using the bremsstrahlung component of a 6 MeV electron beam. This has been previously studied for 2D treatment verification purposes and found to produce useful images [Faddegon, et al. 2008].

3.2.1 6 MeV Setup

A 6 MeV electron beam produced by a Varian 2300EX linac was used (Varian Medical Systems, Palo Alto, California). The linac was operated in total body irradiation mode or in service mode, either of which allows for an electron beam without an applicator cone or cutout. Furthermore, the linac was set to the highest dose rate and the dose rate servo was disabled, so that radiation was produced on every single timing pulse. Bremsstrahlung photons are produced in several parts of the linac including the exit window, primary collimator, jaws, light field mirror, and monitor chambers, however more than half of them originate in the upper and lower scattering foils. [Jarry, et al. 2005] It is these photons that were responsible for forming an image in our experiments. Hereafter, this operating mode will be referred to as the 6 MeV imaging beam to prevent confusion with the linac's 6 MV treatment beam.

3.2.1.1 Solid Water

6 MeV electrons have a continuous slowing down approximation (CSDA) range of 3.05 cm according to current NIST data [Berger, et al. 2005]. To ensure that nearly all the incident electrons were removed from the 6 MeV imaging beam, 4 cm of solid water was placed in the path of the beam. This leaves a beam consisting only of the bremsstrahlung photons mentioned in the previous paragraph, and scattered photons and electrons produced in the solid water due to Compton scattering events. To reduce the number of these latter electrons reaching the detector, the solid water was placed as close as possible to the linac in the accessory tray. This puts the scatter source as far as possible from the detector array.

3.2.1.2 Field Sizes

Experiments were conducted using two field sizes. A 29 x 2 cm² field size, referred to as the fan beam geometry, was used in addition to a 29 x 12 cm² field size, referred to as the cone beam geometry. These field sizes are defined by the linac's jaws at isocenter (100 cm from the photon beam target). The 29 x 2 cm² fan beam field size was chosen so that the light field would barely encompass the detector array. In reality, the field size is slightly larger than the detector array as the 6 MeV bremsstrahlung source (primarily the scattering foils) is closer to the jaws than the photon target. However, it is difficult to set up an experiment using the true field size as there is no light field for it and the penumbra is large. Therefore 29 x 2 cm² was taken to be sufficiently close to a multi-slice fan beam geometry, in which the minimum field size to cover an arc detector is used.

The 29 x 12 cm² field size approximates a cone beam geometry. In cone beam geometry, an area detector is used along with a wider beam. More scatter is generated in the phantom due to the wider beam, which degrades image quality. Also, an area detector will have additional scatter events within the detector that degrade the detector MTF due to the spreading of scattered x-rays. However, at megavoltage energies with high density detectors there is relatively little loss of resolution due to scatter within the detector. A previous Monte Carlo study [Monajemi, et al. 2004] including complete optical transport found that the pre-sampling LSF of this detector reached a relative magnitude of 0.05 at 1.5 mm from the center of the line. Since the detector array in these experiments is 16 mm wide, detectors more than a few millimeters from the outside edges of the array, such as the central 10 detector rows, fully account for the scatter within a detector and give performance representative of what could be achieved with a full cone beam detector. This field size thus evaluates a

fan-beam detector in cone beam geometry to study the effect of phantom scatter on imaging performance.

3.2.2 Wellhöfer PDD at 6 MeV

In order to obtain a general assessment of the quality of the 6 MeV imaging beam, a percent depth dose (PDD) profile in water was measured. This was done with an IC-10 ion chamber (Scanditronix Wellhöfer North America, Bartlett, TN) in a Wellhöfer water tank. While the Wellhöfer system is capable of automatically scanning the probe through the tank and generating a PDD using its own electrometer, this feature was not used as the integration time is too short for the 6 MeV imaging beam dose rates, resulting in excessive noise. Instead, the ion chamber was attached to a Capintec 192 electrometer (Capintec Inc, Ramsey, NJ) and manually stepped through a range of depths, from the surface to 20 cm. The source to surface distance (SSD) was 100 cm and the field size defined by the jaws at isocenter was 25 x 25 cm². This large field size was chosen to minimize the interaction of the beam with the jaws, which is difficult to account for due to the uncertainty in the field size discussed in section 3.2.1.2. In all other respects the conditions were the same as the 6 MeV imaging beam- 4 cm of solid water was placed in the path of the beam, and no electron cone or cutout was used.

3.2.3 Source Location Estimation

It is essential to know the location of the origin of the bremsstrahlung photons in order to place the detector array at the correct location such that it is focused to this source. This was done using the inverse square law in air. A PR-06 ion chamber (Capintec Inc, Ramsey, NJ) with a suitable

buildup cap and Capintec 192 electrometer was used to take a series of measurements along the central axis of the beam covering a large range of distances from the source. This data was then linearized and used to calculate the effective source location as follows. If the machine isocenter is the reference point, 'z' is the distance of the measurement point from the reference point along the machine central axis, 's' is the unknown distance from the reference point to the source, D_{ref} is the chamber reading at the reference point, and D_z is the chamber reading at point z (Figure 3.5), then Equation 3.4 holds.

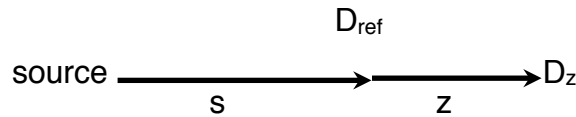


Figure 3.5: Geometry of the source location estimate. The ratio of the readings D_z to D_{ref} must be equivalent to the ratio of the total squared distances to those locations.

$$(z + s)^2 = s^2 \frac{D_{ref}}{D_z} \quad (3.4)$$

Equation 3.4 can be re-arranged as follows:

$$z = s \sqrt{\frac{D_{ref}}{D_z}} - s \quad (3.5)$$

In Equation 3.5, if z is plotted against the square root of the quotient of the reference chamber reading and the chamber reading at point z, a linear

graph is obtain whose slope is s and whose intercept is $-s$, thereby providing two estimates of the source location.

Based on the results of this method, the detector array was positioned with the centre of the detector crystals at 111.5 cm from the linac's 6 MV photon source as measured on the linac's optical distance indicator (ODI). This point was chosen to be 92.5 cm (the detector radius of curvature) away from the effective photon source location of the 6 MeV imaging beam.

3.2.4 Penumbra and Flatness

While the Wellhöfer system was set up to measure the PDD, it was also used to investigate the penumbra and flatness of the x-ray radiation field produced by the 6 MeV imaging beam. This was done using the built-in electrometer by scanning the IC-10 ion chamber automatically at a constant 10 cm depth across the water tank.

3.3 6 MV Treatment Beam

It is expected that the 6 MeV imaging beam will not produce the highest possible quality images for this prototype system. In particular, the resolution will suffer as there are multiple photon sources at different distances (especially the upper and lower scattering foils). Also, the electron beam hitting the lower scattering foil has been broadened and produces a larger bremsstrahlung focal spot than the target in a typical 6 MV treatment beam. These issues particularly impact the resolution of the system.

To better measure the true potential resolution using this detector, it was also tested in a 6 MV treatment beam from a Varian 600C linac (Varian Medical Systems, Palo Alto, California). However, as mentioned earlier, the radiation dose required to obtain the resolution image is very high.

3.3.1 Irradiation Setup

The detector array was positioned at 92.5 cm from the 6 MV photon target using the ODI. The rotating stage was centered using the same metal wire and computed centroid techniques as the 6 MeV beam.

The target to detector distance is 92.5 cm for the 6 MV treatment beam, compared with 111.5 cm for the 6 MeV imaging beam. This is because in the treatment beam the photons originate primarily at the target, whereas in the imaging beam there is no target and most photons originate in the scattering foils. Because the target to detector distance is less for the 6 MV beam, nominally larger field sizes were used. For a fan beam geometry a field size of 35 x 2.5 cm² defined at the machine isocenter was used that barely covers the detector array, while for cone beam geometry a field size of 35 x 15 cm² was used. These field sizes were chosen so that the field size at the detector was the same in both the 6 MV treatment beam and the 6 MeV imaging beam.

3.4 Beam Hardening

As the imaging beam passes through a phantom, the lower energy components of the photon energy spectrum are preferentially attenuated due to their higher attenuation coefficients. Therefore, as the beam passes through the object its mean energy continually increases with depth, a

phenomenon referred to as beam hardening. This causes a curve of attenuation vs. phantom thickness to deviate from linear. Left uncorrected, this will cause beam hardening artifacts in the reconstructed images that make thick regions, such as the centre of a uniform phantom, appear darker (less dense) than they really are [Brooks, et al. 1976]. By measuring the attenuation vs. thickness relationship for uniform slabs of material, we can apply corrections that will reduce this effect.

The attenuation vs. thickness curve must be measured for every detector, since each detector may have incident upon it a beam of slightly different energy spectrum, and lower energy beams can be expected to exhibit a greater amount of beam hardening. This lateral variation in the spectrum can be quite significant when using a treatment beam, since the conical flattening filter causes the beam at the centre to be noticeably harder than the beam at the edges. To a lesser degree, the spectrum may vary because of the angular dependence of the bremsstrahlung spectrum.

3.4.1 Solid Water Phantoms

To measure the attenuation vs. thickness curve, the signal was measured for the 6 MeV imaging beam containing mainly the bremsstrahlung spectrum. Then solid water slabs were added in the path of the beam in the form of 2 cm thick circular solid water phantoms, all of which were from the same production batch to ensure consistent properties among them. The solid water thickness was varied from 0 to 20 cm. The circular solid water phantoms were placed as far away as possible from the detectors to minimize the scatter reaching the detectors, in a position roughly where the rotating stage would be during imaging. The solid water phantoms were not large enough to block the imaging beam path to all the detectors at once, so it was not possible to measure the attenuation vs. thickness

curve for twenty detectors at each end of the 320 detector arc. This was not an issue, since these detectors are outside the field of view required to image the phantoms that were used to test the system.

A similar procedure was used to measure attenuation vs. thickness in the 6 MV treatment beam. The only difference in the setup was the lack of the 4 cm of solid water that was used to remove the electrons in the 6 MeV imaging beam, since this is not used when imaging with the 6 MV beam.

These attenuation vs. thickness curves were later used for beam hardening correction as described in section 3.7.5.

3.5 Imaging Dose Estimation

To measure the dose to the phantom centre, a Protea ion chamber (Protea Systems Corporation, Benicia, CA) was used along with the Capintec 192 electrometer. The chamber reading per monitor unit (reading/MU) was obtained under the reference conditions (see section 3.4.1 and 3.4.2). The linac is pre-calibrated such that 1 MU gives 1 cGy radiation for the reference condition. This is verified annually via the TG-51 absolute dosimetry method [Almond, et al. 1999] and daily by routine output checks. The chamber reading per MU was also obtained for each imaging beam in imaging geometry condition. The dose was then related back to the calibration condition of 1 cGy / MU to find the dose per MU under imaging conditions as follows:

$$\frac{\text{dose}}{\text{MU}} = 1 \frac{\text{cGy}}{\text{MU}} \left(\frac{\text{reading}}{\text{MU}} \right) \bigg|_{\text{reference}}^{\text{imaging}} \quad (3.6)$$

The dose per MU is then related to the actual dose by:

$$\text{Dose} = \frac{\text{dose}}{\text{MU}} (\text{dose rate})(\text{time}) \quad (3.7)$$

where the time is 15.5s for a complete stage revolution or 8.6s for a minimum 200° rotation, and the “dose rate” is around 1080 MU per minute for a Varian 2300EX operating at the maximum 6 MeV pulse rate with the dose servo disabled (disabling the dose servo causes the indicated dose rate to fluctuate slightly, hence the 1080 MU per minute is an estimate) The dose rate is 250 MU per minute for a Varian 600C at the highest 6 MV dose rate with the dose servo on.

This method of estimating the imaging dose is expected to be inaccurate as the scatter conditions are different inside the cylindrical phantoms that were used for evaluating image performance. More significantly, this method will be inaccurate for the 6 MeV imaging beam because that beam has a substantially different energy spectrum than the 6 MV beam that it is being referenced to. For this reason, further Monte Carlo studies were performed.

3.5.1 Reference Conditions

The reference ion chamber reading was taken for both the Varian 2300EX and 600C linacs using a 6 MV beam at 100 cm source to chamber distance (SCD) at a 1.5 cm depth in a solid water phantom. There was at least 10 cm of solid water backscatter material.

3.5.2 Imaging Conditions

The ion chamber readings for the 6 MeV beam used imaging were taken at 7.5 cm depth (corresponding to the phantom centre) in a solid water phantom. The chamber was 83 cm from the photon target. This is the same position where the phantom centre would be during imaging. The 4 cm thick solid water slab utilized to remove electrons was placed in the accessory tray and the 6 MeV electron beam was used, exactly as it would be during imaging. Readings were taken for both fan and cone beam field sizes.

For the 6MV beam, the imaging condition ion chamber readings were again measured at 7.5 cm depth in solid water with the chamber placed where the centre of the phantom would be during imaging. Once again, readings were taken for both fan and cone beam field sizes.

3.6 Monte Carlo Investigations

The 6 MeV imaging beam is expected to have a different energy spectrum than a 6 MV treatment beam. The 6 MeV bremsstrahlung originates primarily in the scattering foils. The upper foil is composed of tantalum ($Z=73$), while the lower foil is aluminum ($Z=13$). The aluminum is much lower atomic number than the tungsten ($Z=74$) target used to generate the 6 MV treatment beam, so it is expected to have a lower energy spectrum. Furthermore, both scattering foils are very thin (0.05 mm for the upper foil and 1.4 mm for the lower foil). This will create a thin target spectrum [Gur, et al. 1979] that incorporates more of the lower energy components due to the lack of self-attenuation inside the target.

To gain a better understanding of the 6 MeV imaging beam energy spectrum a Monte Carlo simulation of the imaging beam was conducted. In addition to calculating the spectrum, this model also allowed an estimate of the dose delivered by the 6 MeV beam.

3.6.1 BEAMnrc Accelerator Model

A Varian 2300EX linac was modeled using the BEAMnrc component of the standard EGSnrc software package [Kawrakow, et al. 2006]. BEAMnrc is a package containing code that can be customized easily via an included GUI in order to simulate common linac components. The following components were included in the simulation:

- a) Primary collimator: The primary collimator was modeled as a 6 cm thick tungsten slab out of which a cone is cut for the beam to pass through.
- b) Exit window: The exit window model consisted of a beryllium slab of 0.254 mm thickness.
- c) Scattering foil: In place of a flattening filter, a scattering foil model was added based on the manufacturer's specifications. The upper foil consists of a tantalum disk 0.5 cm in radius and 0.051 mm in thickness. The lower foil is composed of an aluminum support piece and two aluminum disks totaling a thickness of 1.397 mm.
- d) Monitor chambers: A dual monitor unit chamber was modeled using kapton for the chamber walls and air inside the chamber cavities.
- e) Light field mirror: The mirror was modeled as a mylar slab 0.0508 mm thick inclined 55° relative to the z-axis (the direction the electrons travel).
- f) Shielding: The linac shielding was modeled as a 2 cm thick tungsten slab from which a circular opening of 10 cm radius is cut.

- g) Jaws: The jaws were modeled as slabs of tungsten focused to where the x-ray target would be for a photon beam. The size of the opening was determined automatically based on the desired field size.
- h) Multi-Leaf Collimator (MLC): A MLC model was included, however as the leaves are in their most open position for all simulations the beam does not interact significantly with it. The MLC model has 120 tungsten leaves of thickness 5.83 cm with rounded ends.
- i) Applicator: A square electron applicator model was created that simulated two scrapers and four supporting posts. The scrapers were aluminum with a thickness of 1.6 cm for the upper scraper and 2 cm for the bottom one. The applicator was not included when simulating the imaging beam.
- j) Cutout: A cutout model was created that consists of a cerrobend block. The cutout defines a field size of 10 x 10 cm at 100 cm SSD. The cutout was not included when simulating the imaging beam.
- k) Solid water: In addition to the above linac model, 4 cm of solid water was added when simulating the 6 MeV imaging beam.

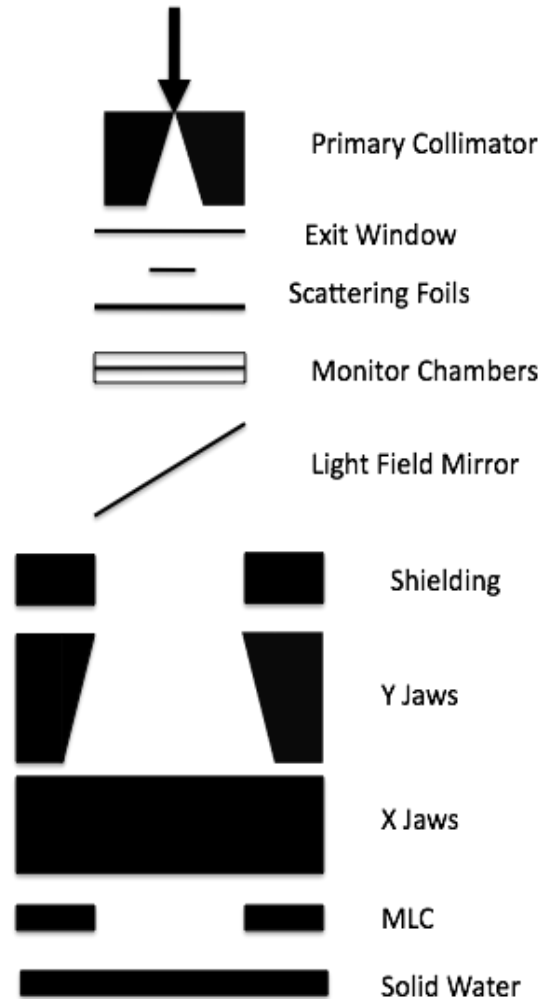


Figure 3.6: Overview schematic of the components that were included in the Monte Carlo simulations for a 6 MeV imaging beam.

3.6.2 Phase Space Simulation

Four Monte Carlo simulations were run. For each of them, the particle energy, charge, position and directional cosines were scored in a plane and saved to a phase space file. For all simulations the electron transport cut-off energy (ECUT) was 0.7 MeV and the photon transport cut-off energy (PCUT) was 0.01 MeV. The incident beam on the target was always mono-energetic 6 MeV electrons in a pencil beam of radius 1 mm. The purpose of each run was as follows:

- a) Wellhöfer: A run was conducted to simulate as closely as possible the conditions in which the PDD was measured on the Wellhöfer system. By comparing these two PDDs some validation of the Monte Carlo model is possible.
- b) Fan beam: This run was intended to simulate the conditions of the fan beam geometry.
- c) Cone beam: This run was intended to simulate the conditions of the cone beam geometry.
- d) Reference: This run simulates the conditions under which a clinical 6 MeV electron beam using the standard electron applicator and cutout is operated. It is necessary in order to obtain an estimate of the dose deposited. The field size was 10 x 10 cm², using a 10 x 10 applicator and cutout. The dose is measured to a small volume on the central beam axis at the depth of maximum dose (d_{max}) at 100 cm SSD.

The details of each run are given by the following table:

Run Name	Field Size (cm)	Scoring Plane Distance (cm)	Number of Histories, i.e. primary electrons (millions)	4 cm Solid Water	Applicator and Cutout
Wellhöfer	25 x 25	100	110	yes	no
Fan Beam	29 x 2	75.5	200	yes	no
Cone Beam	29 x 12	75.5	200	yes	no
Reference	10 x 10	100	150	no	yes

Table 3.1: Parameters used to calculate phase space data for each of four different runs using the Monte Carlo model.

3.6.3 BeamDP Spectrum

The photon spectrum for the phase space file for each run was calculated using the BeamDP model of the EGSnrc software package. The estimated real fluence was calculated in 200 evenly spaced energy bins from zero to 6 MeV. Only the photons were included. This analysis is only required for the simulation of the imaging beam.

3.6.4 DOSXYZnrc PDD Calculations

The dose was calculated for each run using the DOSXYZnrc user code of the EGSnrc software package. The dose was calculated in a 20 cm thick water slab beginning from the location of the scoring plane in the original BEAMnrc simulation. The scoring voxels were a series of cuboids extending along the central axis of the beam. The parameters used are given in the following table:

Run Name	Number of Histories (millions)	Scoring Voxel size (length x width x height in cm)
Wellhöfer	3,200	2 x 2 x 0.2
Fan Beam	10,000	1 x 1 x 0.2
Cone Beam	10,000	1 x 1 x 0.2
Reference	20	2 x 2 x 0.1

Table 3.2: Dose scoring parameters used in the Monte Carlo dose simulations.

The number of histories required for the 6 MeV beam under reference conditions is low because the electron beam deposits nearly all of its energy in the simulated water phantom, whereas a photon beam deposits only a fraction of its energy. To increase the accuracy of the values used in

the dose calculations, the fan and cone beam simulations were run with a smaller voxel size more representative of what happens along the central axis of a beam, and more histories to increase statistical accuracy.

3.6.5 Dose Calculation

The DOSXYZnrc module calculates the dose to each voxel per incident particle in the original beam. That is to say it relates the dose back to the dose per history in the BEAMnrc simulation involving the incidence of primary electrons on the scattering foils. The simulation geometry in BEAMnrc for the imaging beam and reference beam simulations is the same until the bottom of the x and y jaws is reached. Thus the number of electrons per MU is essentially the same in both the imaging and reference conditions, as the monitor chamber will read the same fluence in both cases. Moreover, since the dose to the reference point (i.e. at d_{max} and 100 cm SSD for 10 cm x 10 cm electron applicator) is calibrated to be 1 cGy per MU, the dose at the calculation point in the imaging beam is 1 cGy times the ratio of the dose per history in the two situations.

$$\text{dose} = 1\text{cGy} \frac{\text{dose}_{\text{imaging}}}{\text{history}_{\text{reference}}} \quad (3.8)$$

3.7 Phantoms

A variety of phantoms were imaged to test the uniformity, SNR, high contrast resolution, low contrast definition, and CT number linearity of the experimental MVCT system.

3.7.1 CATPHAN Phantoms

A CATPHAN500 (The Phantom Library, Salem, New York) CT phantom normally consists of a 2.5 cm thick cylindrical casing containing 5 cylindrical inserts within a 15 cm diameter, for a total diameter of 20 cm. It is not practical to image the CATPHAN this way since the field of view subtended by the detector array in the experimental MVCT system is barely sufficient, and the outer diameter of the complete CATPHAN is too large for the rotating stage. Instead, the 15 cm inserts were removed from the casing and imaged individually.

3.7.1.1 Uniformity

The uniform insert from the CATPHAN phantom was imaged to measure the SNR and uniformity of the reconstructed pixel values over the phantom diameter for the experimental MVCT system. It consists of a uniform cylinder 15 cm in diameter designed to have an electron density within 2% of that of water.

3.7.1.2 Ramp Phantom

The CATPHAN ramp insert contains eight 1 cm diameter cylindrical objects of variable electron density. The length of the objects is 2.5 cm. It

was imaged to measure the linearity of the pixel value (and therefore CT number) with electron density. The phantom also contains metal wires that can be used to measure the thickness of reconstructed tomographic slices, however these wires cannot be resolved on this system as the contrast and resolution is lower than the kVCT systems for which the phantom was designed.

3.7.1.3 High Contrast Resolution

The CATPHAN high contrast resolution phantom was also imaged. It contains high contrast bar patterns at spatial frequencies ranging from 1 to 21 line pairs per cm.

3.7.2 Low Contrast Definition

The CATPHAN low contrast phantom was not imaged since the contrast of the targets is optimized for kVCT and none of the targets can be seen in MVCT images at low dose. Instead, a custom made phantom was used that consisted of variably sized objects of nominal 1.5%, 2.5%, and 3% contrast at ^{60}Co energy. For each contrast level there are cylindrical targets of diameters of 20, 4, 5, 6, 7, 8 and 15 mm as well as a 4 mm spherical central target at a contrast of 1.5% (not visible in all slices due to its limited vertical extent).

3.8 Reconstruction

The raw detector data was processed by a script written in MATLAB (The MathWorks, Natick, Massachusetts) in order to perform the final image reconstruction. The attenuation of each ray as it travels from the source to

detector was calculated, adjusted for beam hardening, converted to parallel beam geometry, and then back-projected via the inverse Radon transform [Ramachandran, et al. 1971]. Furthermore, a calibration procedure is required to eliminate ring artifacts caused by air gaps between the detector blocks.

The attenuation $A(i,j)$ of a given ray in a particular projection, i , for a particular detector, j , where I_0 is the signal for that particular detector in an open field, I_d is the dark current signal, and I_i is the signal for that detector and that projection, is given by:

$$A(i,j) = \log\left(\frac{I_{0,j} - I_{d,j}}{I_{i,j} - I_{d,j}}\right) \quad (3.9)$$

3.8.1 Dark Field and Flood Field Averaging

The dark current was measured for each detector every day the imaging was done. A total of 2,500 projections in a dark field (beam off) were taken and averaged together.

The flood field (i.e. I_0 readings in equation 3.9) was calculated by averaging together 2,500 projections taken with the exact same detector and linac setup used for imaging, but with no phantom placed on the rotating stage.

Since the standard deviation in a typical flood field measurement is 1%, even 100 averages will reduce the standard deviation of the mean to less than 0.1%. However, the computational cost of collecting and using extra

measurements is negligible, so 2500 was chosen as roughly the largest number that the system could collect and process in a single revolution of the stage (since the stage does not stop instantly and must start from the same position each time, collecting the 2790 projections that comprise a full revolution would result in two rotations of the stage). For the dark field, there is no variation in the linac output, which is the principal source of noise in the flood field, so the standard deviation of a measurement is already less than 0.1% and the averaging carried out is largely unnecessary.

3.8.2 Drop Pulse Elimination

For the 6 MV treatment beam, one of every six sync pulses is dropped (produces no radiation) in addition to other pulses as determined by the dose rate servo, in order to keep the “dose rate” at the desired 250 MU per minute. It is not possible to disable pulse dropping completely on the Varian 600C linac, nor is it possible to predict exactly which pulses will be dropped since even with the dose rate servo disabled the linac occasionally drops or produces an extra pulse. The dropped pulses were instead detected and excluded from the flood field average by the use of a threshold in which every pulse that produced a signal less than 5 times a typical value of a dark field measurement was considered to be a dropped pulse.

The dropped pulses in the phantom scan data were identified using the same threshold method. To eliminate them, the scan data was averaged over one degree of stage rotation (7.75 pulses) and the dropped pulses were excluded from this average. The average value for each degree was then used for back-projection when reconstructing 6 MV images, as

opposed to each individual projection as done with the 6 MeV imaging beam, for which pulse dropping did not occur.

3.8.3 Multiple Rotation Averaging

In order to be able to vary the dose delivered to the phantom to measure SNR vs. dose curves and contrast to noise ratio (CNR) vs. dose, the data from multiple rotations of the stage was averaged together projection by projection. In these experiments, the data from up to ten full rotations was averaged together to reconstruct a single image, however this approach could be used to reconstruct an image based on an arbitrarily large dose.

3.8.4 Multiple Slice Averaging

A single row of detectors images a slice that, projected back to the centre of the stage, has a slice thickness of about 0.7 mm. This is considerably smaller than that of other systems to which this MVCT system can be compared. For example, the TomoTherapy Hi-Art II system uses a collimator setting of 4 or 5 mm at isocenter. To adjust the slice thickness, the data from two or more rows of detectors can be averaged together. Unless it was desired to use all 16 rows of detectors, typically the data for the desired number of rows was averaged from adjacent detector rows as close to the center of the detector as possible, since edge detectors detect less scatter from within the detector and therefore perform slightly differently.

3.8.5 Beam Hardening Correction

As discussed in Section 3.4, the attenuation vs. solid water thickness curve was measured for each detector (except for 20 detectors on the extreme ends of each row) in 2 cm increments from 0 to 20 cm thickness. This curve is nearly linear, as shown by the example in Figure 3.7, but is slightly concave at its upper end. This is because the attenuation at greater thicknesses is not as much as predicted by a linear trend-line (Figure 3.7), since beam hardening has reduced the average attenuation coefficient of the beam due to its increased effective energy as it travels through the phantom.

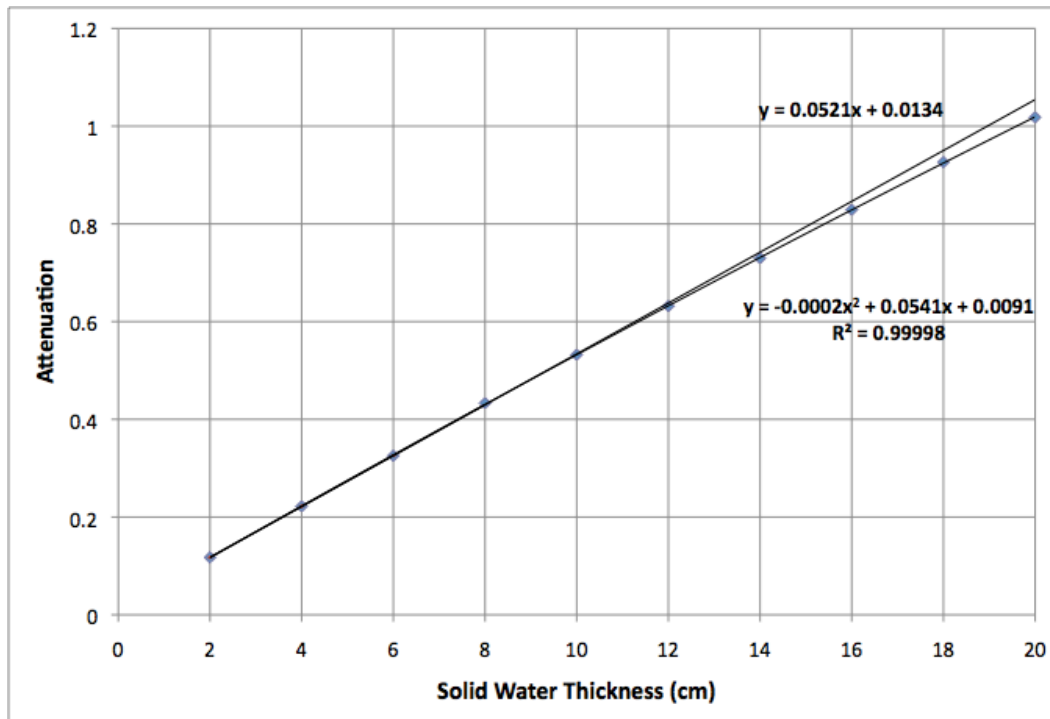


Figure 3.7: Attenuation vs. thickness curve for a typical detector. A linear trend-line for the first three data points is shown alongside a second order polynomial trend-line for the full dataset.

3.8.5.1 Determination of Equivalent Solid Water Thicknesses

A second order polynomial was fitted to the attenuation vs. thickness curve. The first order component represents the linear portion of the attenuation, while a much smaller negative second order component reflects the degree to which the attenuation at greater thickness is reduced due to beam hardening. Using this second order polynomial, the equivalent solid water thickness (that is, the solid water thickness that would produce the observed attenuation if the beam hardening effect did not exist) for the observed attenuation in every measured projection was calculated. It is these equivalent thicknesses that were eventually back projected.

The end detectors for which it is not possible to measure the beam hardening parameters were assigned the average first order beam hardening parameter for reconstruction. Since these detectors are outside the field of view required to image a 15 cm phantom, they never see a reduction in fluence due to attenuation and so this approximation has no effect on the final reconstructed images.

3.8.6 Fan to Parallel Beam Conversion

At this point in the reconstruction process, the projection data is in the form of beam hardening corrected equivalent solid water thicknesses. These projections are in fan beam geometry. In order to use the MATLAB implementation of the inverse Radon transform, it is necessary to convert them to parallel beam projections. This was done via linear interpolation using MATLAB's built in fan2para function.

3.8.6.1 Fan to Parallel Conversion Bug Workaround

When MATLAB's fan2para function is given the data for a full 360° rotation, it does not use all the data. Rather, it uses a minimal amount of data, fan angle + 180°, and discards the rest. This is an issue because the discarded data will result in an image with a lower SNR than could be obtained for a given dose.

To work around this limitation, the fan2para function was called twice. The second time, the fan beam projections were rotated 180°, so as to begin with the rotating stage in the opposite to starting position. This causes the MATLAB software to do the conversion using the data that was discarded the first time. The resulting parallel beam data from the two fan2para calls was then summed.

3.8.7 Inverse Radon Transform

From here the inverse Radon transform was carried out using the MATLAB iradon function. This is an implementation of the filtered back-projection method. It was carried out using the Ram-Lak filter [Ramachandran, et al. 1971]. This ramp filter provides the best spatial resolution, though passes more noise, than other filters have that been developed to attenuate high spatial frequency components.

3.8.8 Uniform Factor Correction

The images produced using the method described above contain visible concentric ring artifacts. These artifacts result from the tiny air gaps between the 16 x 16 detector blocks (Figure 3.8).

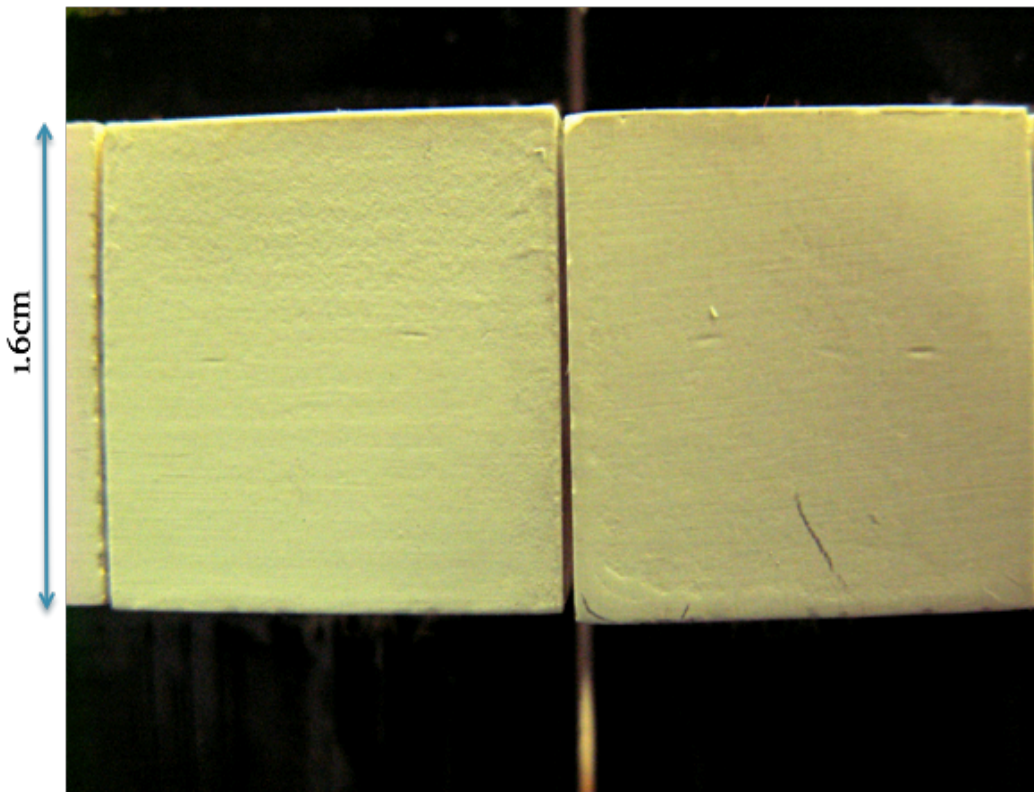


Figure 3.8: Close-up view of the detector blocks showing the sub-millimeter gaps between the blocks.

These gaps alter the line spread function (LSF) of detectors near them due primarily to changes in the propagation of scattered x-rays passing through them. One way to correct for this would be to fill the gaps with a radiologically equivalent material. However, this proved challenging to implement due to the manufacturing constraints of these prototype systems [Monajemi, et al. 2006 (1)]. To correct these artifacts, a calibration procedure similar to what our group has used in the past was implemented [Monajemi, et al. 2006 (1)]. For each phantom that imaged, a uniform phantom of the same dimensions was also imaged. We then reconstructed an image of the uniform phantom and created a mathematical uniform phantom of the same dimensions using MATLAB (i.e. a uniform circle of the same size and location). The mathematical phantom was re-projected using the Radon transform and the angular mean of these mathematical projections was divided by the angular mean of the measured projections of the uniform phantom to determine calibration factors for each detector (Figure 3.9). All of the experimental data for that detector was then multiplied by the detector's calibration factor. Except for the detectors near the air gaps at the edges of 16 x 16 blocks, the uniform calibration factors have a value of unity (Figure 3.10). The uniform factors also diverge from unity near the edges of the phantom. This is due to the difficulty of perfectly superimposing (ie. registering) the simulated mathematical phantom on top of the image of the real phantom, particularly since the mathematical phantom has no penumbra whereas the real one does because the real photon sources do not have an infinitesimally small size. If the mathematical phantom is even slightly off center relative to the projection data there is a dip at one edge and a rise at the other (Figure 3.10). For any other phantom of the same size, the projection data was corrected by the uniform calibration factors.

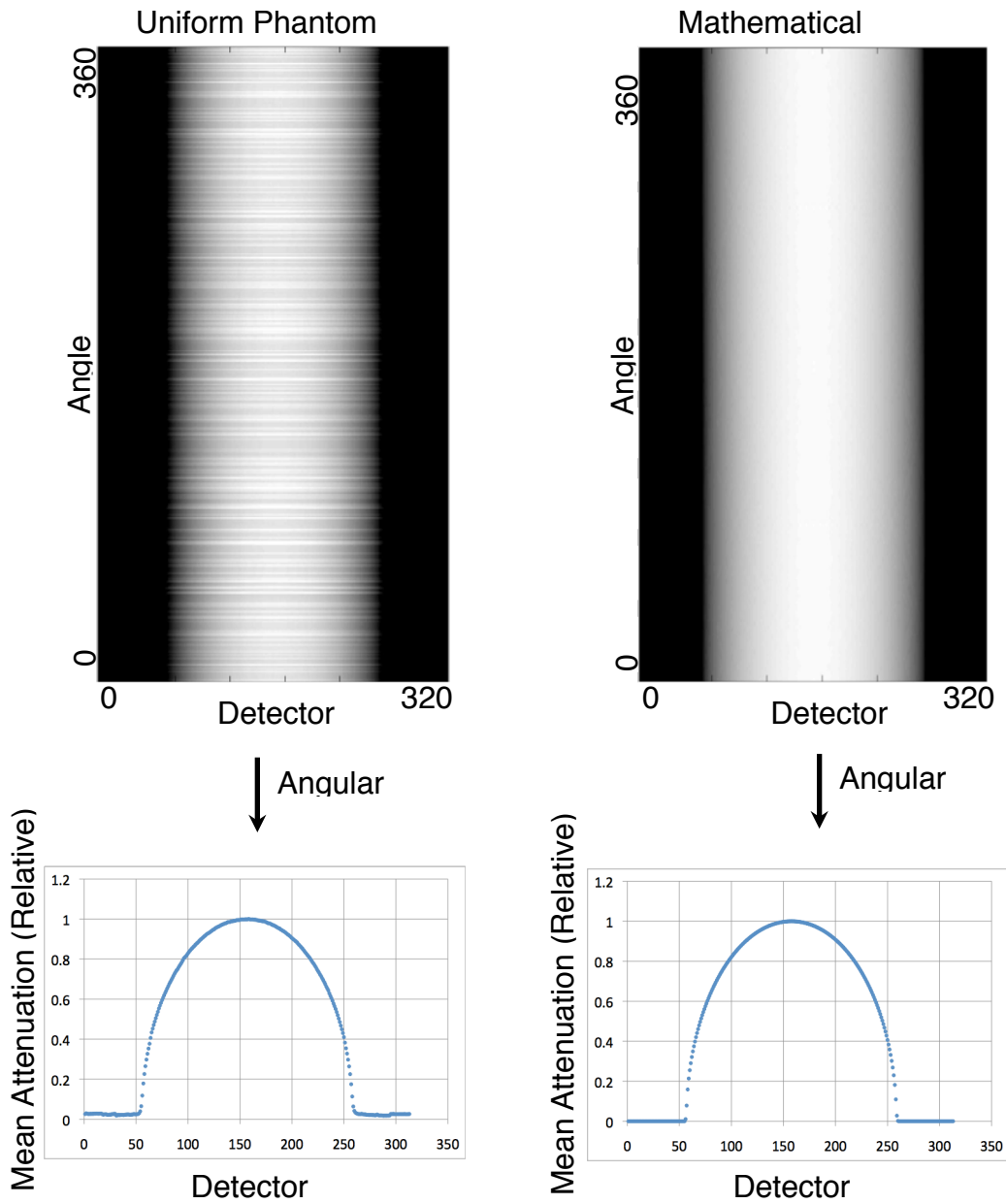


Figure 3.9: Process used to create uniform factors. The data for each detector is averaged over all views and normalized. This is done for both the real data from a uniform phantom and mathematically generated ideal data for a same size uniform phantom. The final factors for each detector are generated by dividing the mathematical mean for that detector by the mean of the measured data for that detector.

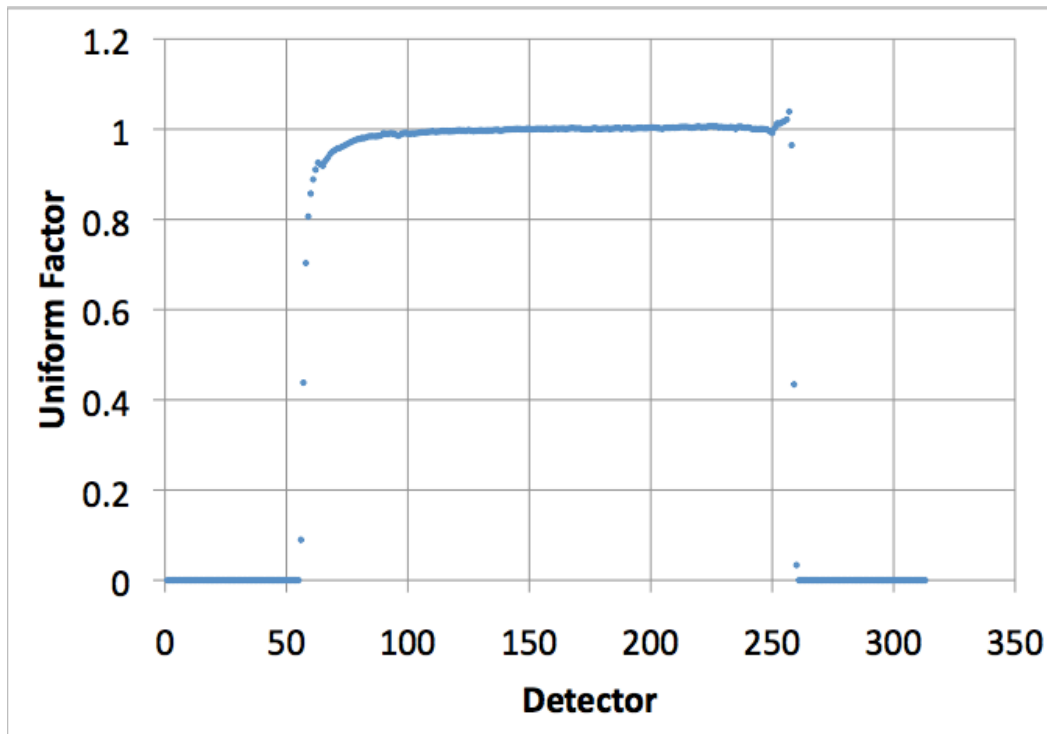


Figure 3.10: Uniform factors for each detector. The uniform factors are generally unity, with the exception of detectors near the air gaps and the phantom edges.

3.9 Image Analysis

The final images produced by the MATLAB scripts were 220 x 220 pixel bitmaps (64 bits deep). These images were then analyzed using open source OsiriX software [Rosset 2004]. This software allowed for the calculation of the mean and standard deviation of a ROI, as well as other standard image analysis tools.

3.9.1 Conversion Process

The bitmap images produced by MATLAB have an arbitrary scale resulting from the process of filtered back-projection. These 64 bit double precision pixel values were then converted to a 16 bit unsigned integer format compatible with OsiriX by re-scaling them to use the entire possible dynamic range of a 16 bit integer as follows, where i is the original image, $i_{x,y}$ is a given pixel in that image, and $i_{x,y \text{ scaled}}$ is the new 16 bit image.

$$i_{x,y \text{ scaled}} = \left(2^{16} - 1\right) \left(\frac{(i_{x,y} - \min(i))}{\max(i) - \min(i)} \right) \quad (3.10)$$

No significant loss of accuracy results from this operation, because the original image i is typically composed of four digit decimal numbers ranging from -0.1000 to 0.2000 and therefore the dynamic range of a 16 bit integer (0 to 65535) is sufficient.

3.10 TomoTherapy

For comparison purposes, the same phantoms were imaged in a commercial TomoTherapy Hi-Art II system (TomoTherapy Inc, Madison WI). This system acquires helical MVCT images with a single slice xenon gas detector in a 3.5 MV photon beam. The slice thickness is 0.5 cm defined by the primary collimator at the phantom center. The only user adjustable parameters are the reconstruction matrix, set to 512 x 512 pixels, and the pitch (couch travel per rotation/slice thickness), set to 1.0 (high quality mode). Literature estimates of the TomoTherapy dose in “high quality” mode range widely from 1 cGy [Meeks, et al. 2005] to 3 cGy [Stutzel, et al. 2008; Yartsev, et al. 2007] .

References

Almond, P. R., Biggs, P. J., Coursey, B. M., Hanson, W. F., Huq, M. S., Nath, R. & Rogers, D. W. O. AAPM's TG-51 protocol for clinical reference dosimetry of high-energy photon and electron beams. *Medical physics* 26, 1847-1870 (1999).

Berger, M. J., et al. Stopping-Power and Range Tables for Electrons, Protons, and Helium Ions. in National Institute of Standards and Technology [database online]. 2005 Available from <http://www.nist.gov/login.ezproxy.library.ualberta.ca/physlab/data/star/index.cfm>.

Brooks, R. A. & Di Chiro, G. Beam hardening in X-ray reconstructive tomography. *Physics in Medicine and Biology* 21, 390-398 (1976).

Faddegon, B. A., Wu, V., Pouliot, J., Gangadharan, B. & Bani-Hashemi, A. Low dose megavoltage cone beam computed tomography with an unflattened 4 MV beam from a carbon target. *Medical physics* 35, 5777-5786 (2008).

Gullberg, G. T., Crawford, C. R. & Tsui, B. M. W. Reconstruction Algorithm for Fan Beam with a Displace Center-of-rotation. *IEEE Transactions on Medical Imaging* MI-5, 23-29 (1986).

Gur, D., Bukovitz, A. G. & Serago, C. Photon contamination in 8-20-MeV electron beams from a linear accelerator. *Medical physics* 6, 145-146 (1979).

Jarry, G. & Verhaegen, F. Electron beam treatment verification using measured and Monte Carlo predicted portal images. *Physics in Medicine and Biology* 50, 4977-4994 (2005).

Kawrakow, I., and Rogers, D. W. O. The EGSnrc Code System: Monte Carlo Simulation of Electron and Photon Transport. in National Research Council of Canada [database online]. 2006 Available from <http://irs.inms.nrc.ca/login.ezproxy.library.ualberta.ca/software/egsnrc/documentation/pirs701/index.html>.

Kobayashi, M., Ishii, M., Usuki, Y. & Yahagi, H. Cadmium tungstate scintillators with excellent radiation hardness and low background. *Nuclear Inst. and Methods in Physics Research*, A 349, 407-411 (1994).

Meeks, S. L., Harmon, J. F., Jr, Langen, K. M., Willoughby, T. R., Wagner, T. H. & Kupelian, P. A. Performance characterization of megavoltage computed tomography imaging on a helical tomotherapy unit. *Medical physics* 32, 2673-2681 (2005).

Monajemi, T. T., Fallone, B. G. & Rathee, S. Thick, segmented CdWO₄-photodiode detector for cone beam megavoltage CT: a Monte Carlo study of system design parameters. *Medical physics* 33, 4567-4577 (2006).

Monajemi, T. T., Steciw, S., Fallone, B. G. & Rathee, S. Modeling scintillator-photodiodes as detectors for megavoltage CT. *Medical physics* 31, 1225-1234 (2004).

Monajemi, T. T., Tu, D., Fallone, B. G. & Rathee, S. A bench-top megavoltage fan-beam CT using CdWO₄-photodiode detectors. II. Image performance evaluation. *Medical physics* 33, 1090-1100 (2006).

Ramachandran, G. N. & Lakshminarayanan, A. V. Three-dimensional reconstruction from radiographs and electron micrographs: application of convolutions instead of Fourier transforms. *Proceedings of the National Academy of Sciences of the United States of America* 68, 2236-2240 (1971).

Rosset, A., Spadola, L. & Ratib, O. OsiriX: An open-source software for navigating in multidimensional DICOM images. *Journal of Digital Imaging* 17, 205-216 (2004).

Stutzel, J., Oelfke, U. & Nill, S. A quantitative image quality comparison of four different image guided radiotherapy devices. *Radiotherapy and oncology : journal of the European Society for Therapeutic Radiology and Oncology* 86, 20-24 (2008).

Yartsev, S., Kron, T. & Van Dyk, J. Tomotherapy as a tool in image-guided radiation therapy (IGRT): Theoretical and technological aspects. *Biomedical Imaging and Intervention Journal* 3 (2007).

Chapter 4: RESULTS AND DISCUSSION

This chapter describes the results and discusses observations related to the characteristics of the photon beams used for evaluating the prototype MVCT system, the impact of artifact correction on the images produced, and the evaluation of the properties of the MVCT system. The photon beams are characterized by their effective energy from both physical measurement and Monte Carlo analysis, their spectrum, and their radiation dose rate. The imaging system is evaluated based on the uniformity of images that it produces, the signal to noise ratio of a uniform image, the high contrast resolution, the low contrast definition, and the CT number linearity.

4.1 Beam Characteristics

The results of several experiments designed to better understand the properties of the 6 MeV imaging beam are discussed in this section, as well as the results of experiments designed to estimate the dose delivered in both the 6 MeV imaging beam and the 6 MV treatment beam. In particular, this section presents an estimated location of the source of the imaging beam, beam hardening measurements for both the beams, PDD measurements for the imaging beam, a Monte Carlo derived imaging beam spectrum, and a profile for the imaging beam.

4.1.1 Source Location Estimation

The effective source location of the bremsstrahlung photons in the 6 MeV imaging beam was measured by the inverse square in air method, as discussed in Section 3.2.3. Figure 4.1 shows the distance below the

machine isocenter (z) vs. the square root of the quotient of the reference chamber reading at machine isocenter to the chamber reading at point z . The horizontal error bars are based on the error in the chamber reading propagated by limit error, while the vertical error bars, due to errors in setting the distance, are too small to see. Since the horizontal error is less than 0.5% for all data points and the vertical error is minimal, the slope and intercept calculated by the least squares method can be considered to be accurate. As per Equation 3.3, the slope of 80.8 ± 0.6 cm corresponds to the distance from the isocenter to the location of the effective source, and the intercept corresponds to the negative of the effective source location, giving a second estimate of 81.1 ± 0.7 cm. The two estimates are in agreement within error.

Since the isocenter of the linacs used in these experiments is 100 cm from the photon target (the target was retracted for the imaging beam), these two estimates suggest that the effective bremsstrahlung source for the imaging beam is 19 cm below the photon target. This would place the effective source slightly above the upper scattering foil, which is located 24.1 cm below the photon target. The 19 cm estimate is in agreement with measurements made by Zhu [Zhu, et al. 2001] and is similar to the effective source location of a 6 MeV electron beam on a similar linac measured during commissioning tests. Based on this information, the detectors were positioned 92.5 cm (the detector radius of curvature) from this point in order to eliminate the effect of beam divergence. This put the detector at 111.5 cm from the photon target in order to focus the detector to the effective source location. While it seems that this method places the detector such that it focuses to within 1 cm of the effective source location, it should be noted that since the source of the imaging beam is actually two scattering foils separated by 3.5 cm, the detector is not perfectly focused to either one. Fortunately, an error of 5 cm in positioning the detector alters the angle from the source to one of the end detectors by

less than 0.5° . For detectors closer to the center, the change in angle caused by a 5 cm error is even less. Since it seems likely that the detector was placed in such a manner as to focus to within 5 cm of the sources of most of the photons, and a 0.5° beam divergence has negligible effect, we can conclude that the setup effectively eliminates the effect of beam divergence.

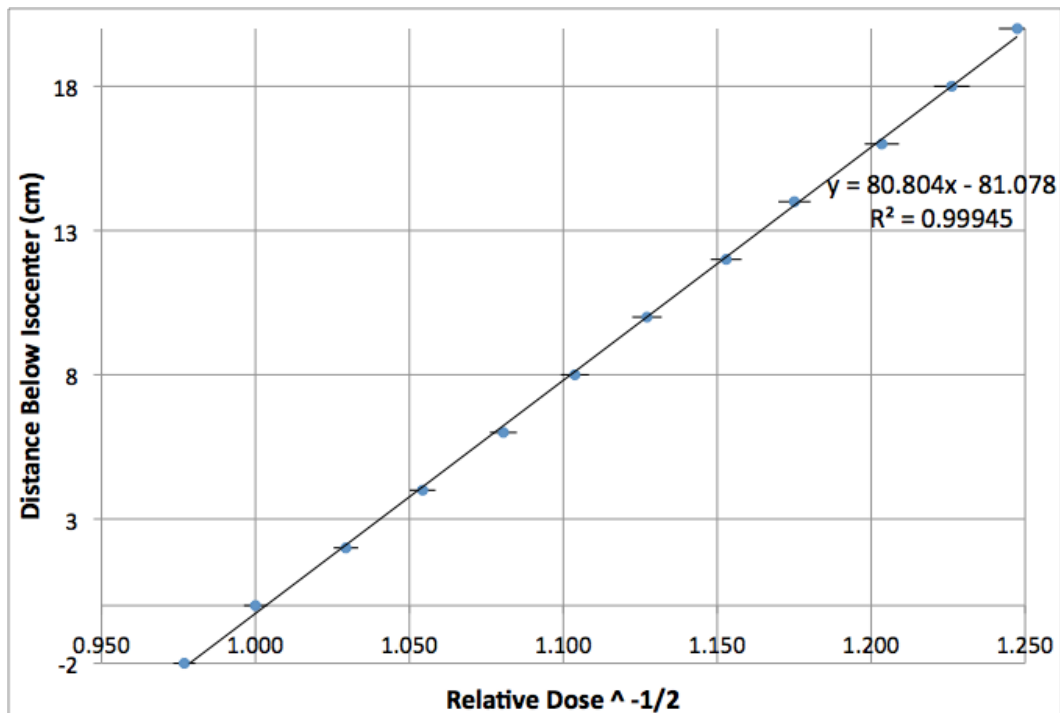


Figure 4.1: The distance below isocenter (z) plotted as a function of the square root of the quotient of the reference chamber reading at isocenter to the chamber reading at point z . The slope corresponds to the distance from the effective bremsstrahlung source to the linac isocenter, while the y -intercept is the negative of this distance.

4.1.2 Beam Hardening

An attenuation vs. thickness curve similar to that in Figure 3.7 was measured for all detectors except those on the extreme ends of the detector array. These curves were then fit to a second order polynomial. The first and second order coefficients of these polynomials in the 6 MeV

imaging beam for the detectors in one of the central rows are plotted in Figure 4.2, while those for the 6 MV treatment beam are plotted in Figure 4.3.

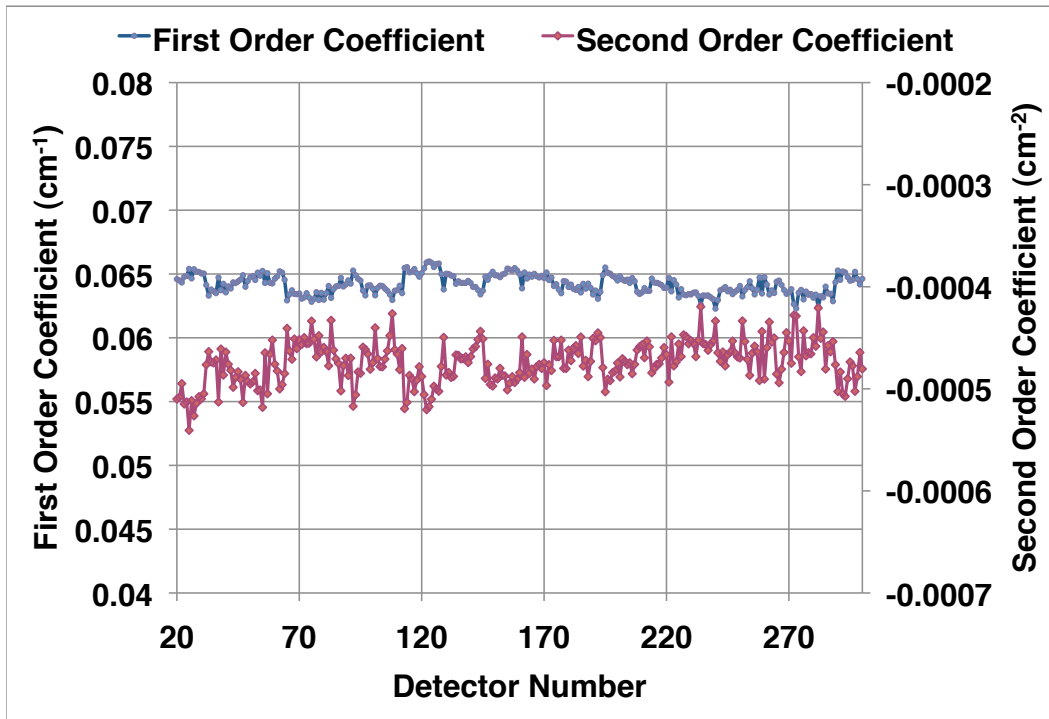


Figure 4.2: The first and second order coefficients of the polynomial fit to the beam hardening calibration data for the 6 MeV imaging beam. The parameters are shown for one of the central rows along the detector arc.

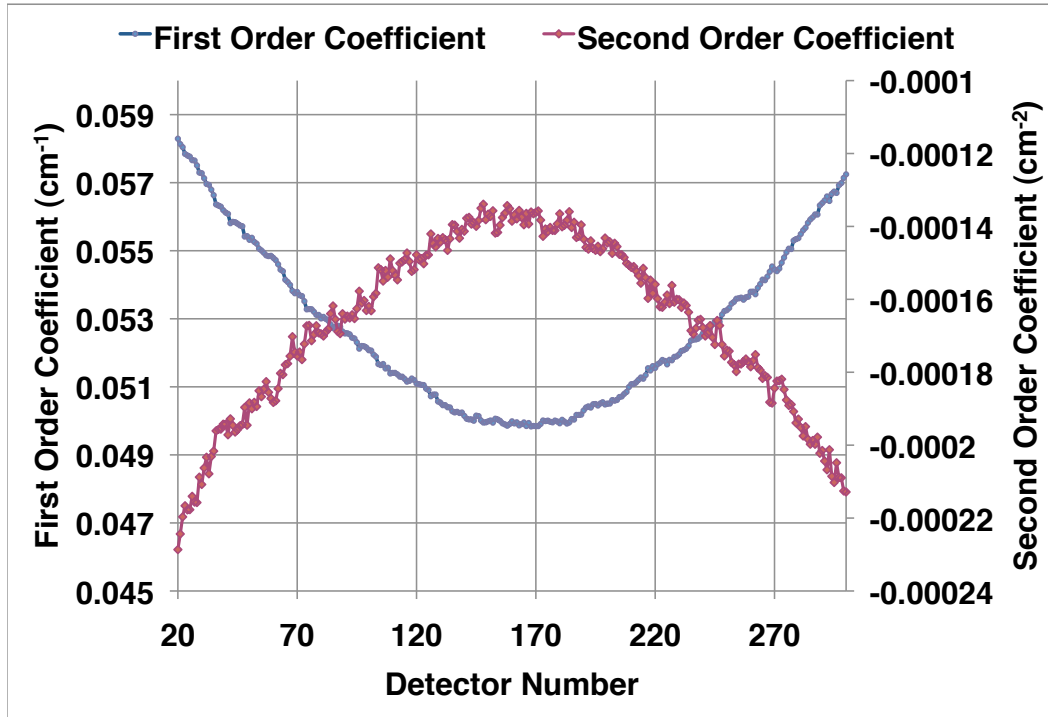


Figure 4.3: The first and second order coefficients of the polynomial fit to the beam hardening calibration data for the 6 MV treatment beam. The parameters are shown for one of the central rows along the detector arc.

4.1.2.1 Parameters in 6 MeV Imaging Beam

In the 6 MeV imaging beam, the first order beam hardening coefficient is nearly constant across the detector (Figure 4.2), with a mean value of $0.0642 \pm 0.0007 \text{ cm}^{-1}$. This corresponds to the linear attenuation parameter for a 1.25 MeV photon (Attenuation parameters provided by NIST data) for water. The second order coefficients are similarly uniform, with a mean of $-0.00047 \pm 0.00002 \text{ cm}^{-2}$. The negative sign of the second order coefficient means that the curve bends more and more downward from linear curve as the thickness is increased.

The uniformity of the coefficients suggests that the beam spectrum incident upon each detector is essentially the same. As will be discussed in the following section, this is quite different from a treatment beam. The only visible structure to the beam hardening data are the very slight differences in the properties of the detectors on the edges of each 16 x 16 detector block, which can be seen as slight jumps and dips in Figure 4.2.

4.1.2.2 Parameters in 6 MV Treatment Beam

For the 6 MV treatment beam (Figure 4.3), the beam hardening parameters are significantly different compared to the 6 MeV imaging beam. The first order coefficient increases from a minimum of 0.05 cm^{-1} at the centre, to 0.058 cm^{-1} at the edges. These values correspond to photon energies of about 2 MeV at the centre and 1.5 MeV at the sides, respectively, for water. The magnitude of the second order component is two or three times less than that of the 6 MeV imaging beam, suggesting lesser amount of beam hardening in the phantom.

The change in effective energy from the centre to the sides in a flattened treatment beam has been understood for a long time [Hanson, et al. 1980]. Because the flattening filter is thicker at the center there is more beam hardening within the flattening filter at the centre of the radiation field and less toward the edges resulting into lower first order coefficient at the center as seen above. The presence of the flattening filter also results in less beam hardening in phantom compared to the imaging beam.

The beam hardening data implies a higher energy for the 6 MV beam compared to the 6 MeV imaging beam. This is to be expected, since the bremsstrahlung in the 6 MV beam is produced by a higher atomic number material (tungsten as opposed to aluminum and tantalum), the target is

thicker and therefore causes more self-attenuation, and the flattening filter hardens the beam.

All of these factors that increase the effective energy of the beam are undesirable for imaging since the contrast is less at higher energy. For this reason, Faddegon [Faddegon, et al. 2008] has shown that a treatment linac can feasibly be adjusted to produce a better beam for imaging by de-tuning the energy as low as possible, in their case to 4 MV, by using a low Z carbon target, and by removing the flattening filter. In our case, the 6 MeV imaging beam benefits from being lower in energy than the treatment beam and not having the angle dependent beam hardening created by the flattening filter.

It should also be noted that the imaging artifact due to variation in the first order coefficient may be more severe than that due to the second order coefficient. The negative magnitude of the second order coefficient is indicative of the beam hardening occurring in the solid water while the variation in these coefficients across the detectors is due to the presence of the flattening filter.

4.1.3 PDD measurements

The PDD obtained in water using the IC-10 ion chamber in the Wellhöfer water phantom and the PDD produced by the Monte Carlo Simulation for the 6 MeV imaging beam can be seen in Figure 4.4. Both the measured and calculated results are for a 25 x 25 cm² field size and 100 SSD, to verify the Monte Carlo model against measurement. Excluding those points that lie closest to the surface, for which the ion chamber measurements are the least accurate due to the finite size of the chamber, there is less than 1% discrepancy between the simulated and measured

data. This is within the error in the measured data in most cases, although the simulated PDD does seem to trend slightly lower. This suggests that the Monte Carlo model is valid, although there is reason for suspicion that the Monte Carlo beam is slightly lower in energy than the actual measured beam.

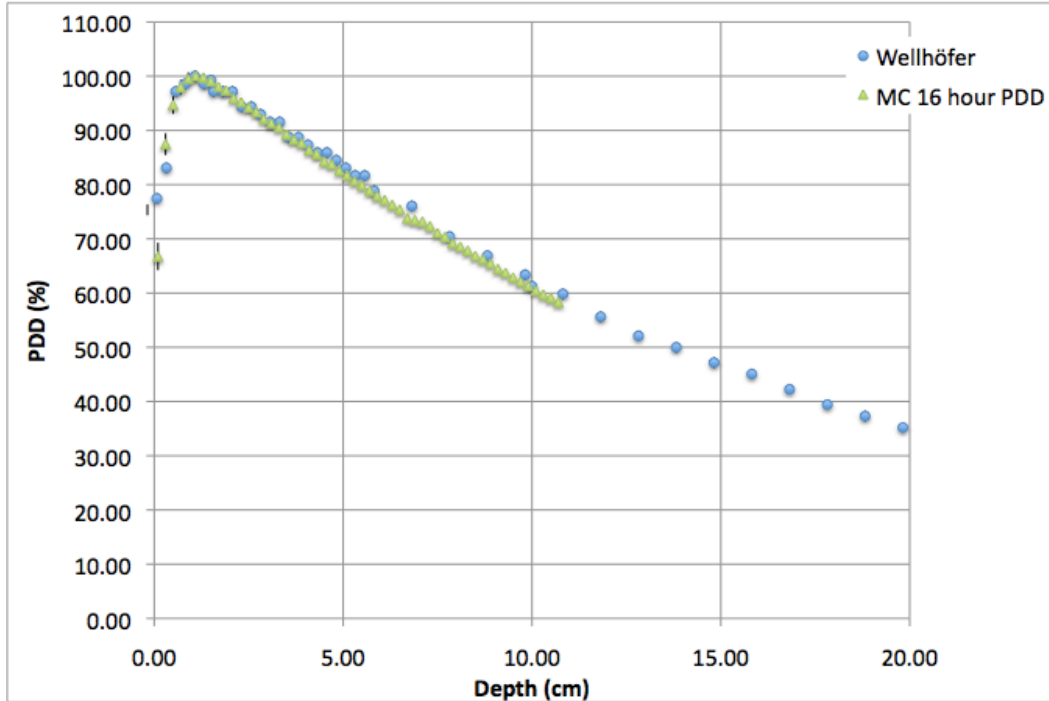


Figure 4.4: Measured and simulated PDD in 6 MeV imaging beam. In both cases the SSD is 100 cm, the field size is 25 x 25 cm², and the curves are normalized at 1.1 cm (the depth of the maximum dose in both cases). Where error bars are not seen they are smaller than the data points.

4.1.4 Monte Carlo Spectrum

The Monte Carlo derived energy spectrum of the 6 MeV imaging beam in fan beam geometry is seen in Figure 4.5. The spectrum peaks at very low energy (50 keV). This is expected since the self-attenuation in the scattering foils is much less than in a tungsten target and there is no beam hardening caused by a flattening filter. There are 59%, 24%, 9%, 4.3%

and 3.4% of photons in the ranges of 0-0.5 MeV, 0.5-1.5 MeV, 1.5- 2.5 MeV and 2.5-3.5 MeV respectively.

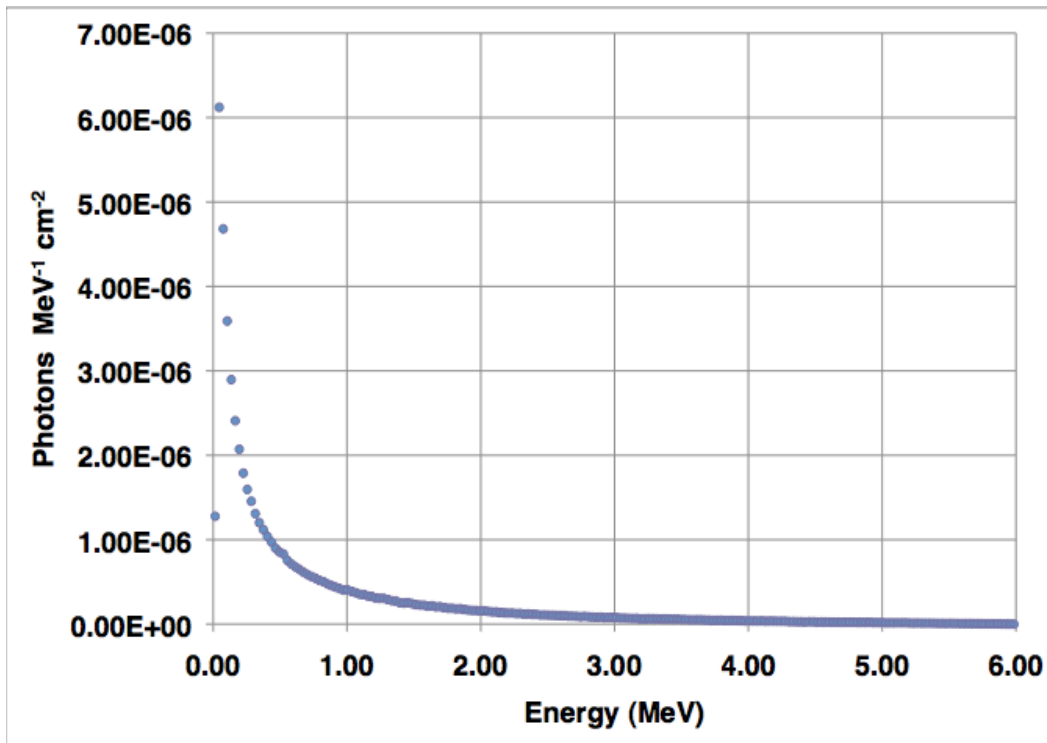


Figure 4.5: Photon fluence per incident electron on the scattering foil as a function of energy in a 6 MeV imaging beam. There are 59%, 24%, 9%, 4.3% and 3.4% of photons in the range of 0-0.5 MeV, 0.5-1.5 MeV, 1.5- 2.5 MeV and 2.5-3.5 MeV respectively.

The spectrum has an average energy of 0.770 MeV due to many low energy photons, however it has small components all the way up to 6 MeV. Monte Carlo simulations for the same type of accelerator (Varian 2100EX) published by Jarry [Jarry, et al. 2005] obtained average energy values of 1.1 MeV and 0.9 MeV for the upper and lower scattering foils respectively in large field sizes similar to these simulations. It is not clear why this noticeable difference exists, however it could be because of

different approximations used to create the virtual linac models or different modeling of the scattering foil. The lower energy bremsstrahlung produced in the 4 cm layer of solid water used to remove electrons in the 6 MeV imaging beam could be another reason, however Monte Carlo photon spectra measured with and without the solid water show no appreciable difference. In any case, it is clear that the imaging beam has more low energy components than the flattened treatment beam does. This means that images produced with the imaging beam will likely have better contrast that would be obtained with the treatment beam.

4.1.5 Ratio Dose Estimate

The dose delivered during imaging was measured (Table 4.1) using ion chamber readings via the ratio of the reading under imaging conditions compared to calibration conditions as per Section 3.4.

Beam	Dose per MU (cGy)	Dose Rate (MU/min)	Rotation Time (s)	Dose per Image (cGy)
6 MeV Fan Beam	0.0035	1080	15.5	0.97
6 MeV Cone Beam	0.0048	1080	15.5	1.35
6 MV Fan Beam	1.7	250	8.6	62.4

Table 4.1: Dose Estimates for a single image created in the 6 MeV imaging beam and 6 MV treatment beam. The dose for the imaging beam is estimated for a full rotation, while the dose for the treatment beam is estimated for a minimal 200° rotation in order to reduce the dose as much as possible.

It is clear from Table 4.1 that even for a minimal rotation of 180° plus the 20° fan angle, the dose from the 6 MV treatment beam is too much for in-vivo use. Furthermore, to obtain the 250 MU/min dose rate, the Varian 600C drops more than 1 out of each 6 pulses on average. The large dose per pulse means that any attempt to reduce the dose by dropping more pulses (or throwing away the data from pulses) will cause artifacts. For example, to get a 1 cGy image would require dropping 96% of pulses- far more than can be done without causing visible artifacts. It should be noted that for the scanning system described in the previous chapter, the detector reading for every pulse may correspond to a measured fan or cone beam projection of the object being scanned. Therefore, reducing linac pulse rate or artificially throwing away acquired data for certain number of pulses to reduce the dose per image really entails throwing away projection data. Too few projections means spoke type artifacts will appear in the image [Joseph, et al. 1982]. Thus it is much more desirable to reduce the dose per pulse than to reduce the pulse frequency in order to reduce the imaging dose. This was the primary motivation for using the bremsstrahlung component of the electron beam for imaging, although this beam is considered to be a contaminant in electron beam radiotherapy.

4.1.6 Monte Carlo Dose Estimate

The Monte Carlo dose simulations for the 6 MeV imaging beam (Section 3.5) produced the results seen in Table 4.2. The Monte Carlo dose estimates for fan and cone beam geometry come out 19% and 24% larger than the ion chamber estimates, respectively. Such disagreement is to be expected due to the limitations of each method. The ion chamber ratio method does not account for the difference in photon spectrum between the imaging beam and the 6 MV treatment beam. The response of the ion chamber cannot be assumed to be the same in both spectra and thus

taking the ratio of ion chamber readings is inaccurate. The Monte Carlo model assumes that the linac produces mono-energetic electrons uniformly in a 1 mm radius pencil beam that strikes the scattering foil and disregards the electrons that are scattered back into the monitor chambers. Electrons scattered back to the monitor chambers due to the solid water in the imaging beam would cause the linac to overestimate the dose delivered, resulting in a lower actual dose for the real imaging beam. However, this is likely not an issue since the main difference between the reference 6 MeV beam and the imaging beam is the solid water, which is located 46 cm from the monitor chambers. Even if the electrons hit the solid water and scattered isotropically (in reality forward directions would be far more likely), the chance of hitting the 4.8 cm radius monitor chamber from that distance is only 0.2%. Preliminary Monte Carlo calculations showed no difference in dose to the monitor chamber with the solid water. The models also make simplifications about the linac design such as not considering the supporting members of the scattering foil assembly or the presence of the accessory tray in which the solid water is mounted. These simplifications are thought to have negligible effect.

Beam	Dose per Incident Particle (10^{-16} Gy)	Dose per MU (cGy)	Dose per Image (cGy)
6 MeV Reference Conditions	556	1.00	N/A
6 MeV Fan Beam	2.30	0.0041	1.15
6 MeV Cone Beam	3.38	0.0061	1.69

Table 4.2: Dose Estimates for a single image created with the 6 MeV imaging beam based on Monte Carlo simulations. In both geometries a dose rate of 1080 MU/min was assumed, and the dose per image is given for a full 360° rotation.

In both cases the dose in cone beam geometry was about 40% more than in fan beam geometry. However, to image the same volume that can be imaged in one rotation of a cone beam detector, multiple fan beam rotations would be needed, each of which would contribute scattered radiation to the entire volume. This means that the dose for a complete scan in fan beam geometry compared with cone beam geometry would be more similar.

Highly accurate dose calculations for individual radiotherapy patients are difficult and are seldom carried out, because the dose delivered in-vivo depends on the size and anatomy of each patient, the volume being imaged, as well as other factors such as the presence of prostheses. The dose estimates in this thesis provide a general indication of what the dose for a fully integrated MVCT system based on this technology could be. For consistency, the dose estimates based on the ion chamber data are used exclusively for the rest of this work.

4.1.7 Penumbra and Flatness

A profile of the 6 MeV imaging beam is seen in Figure 4.6. The profile is measured at 10 cm depth for a 25 x 25 cm² field size. The corresponding profile for the 6 MV treatment beam is also shown. In both cases there is 4 cm of solid water in the path of the beam, so that any change in beam quality resulting from the solid water is the same in both cases. The 6 MV treatment beam delivers fairly uniform dose across the field due to the use of a flattening filter. The slight dip towards the center is a result of the flattening filter being optimized for 10 cm depth in a 10 x 10 cm² field size, while the actual field size was much larger and the depth, when taking into account the 4 cm of solid water, is deeper.

While the 6 MeV beam data has a very large amount of noise due to the dose rate being far below what the Wellhöfer scanning system is optimized for, it is clear that the 6 MeV beam drops by more than $\frac{1}{2}$ from the centre of the beam to the edge. Furthermore, while the treatment beam drops quickly from 80% to 20% in 9 mm, the 6 MeV beam has a shallower slope in the penumbra (drop-off) regions. This is because the source in the 6 MeV imaging beam is closer to the detector and so the jaws (collimators) in the linac are not focused to it. For the same reason, the field size in the 6 MeV beam is noticeably larger despite using the same jaw settings. The presence of a larger penumbra caused by the jaws being mis-focused has no effect on the imaging since the field size is large enough that the penumbra does not fall on the detectors, though it contributes some scatter that would be absent in a more closely collimated beam.

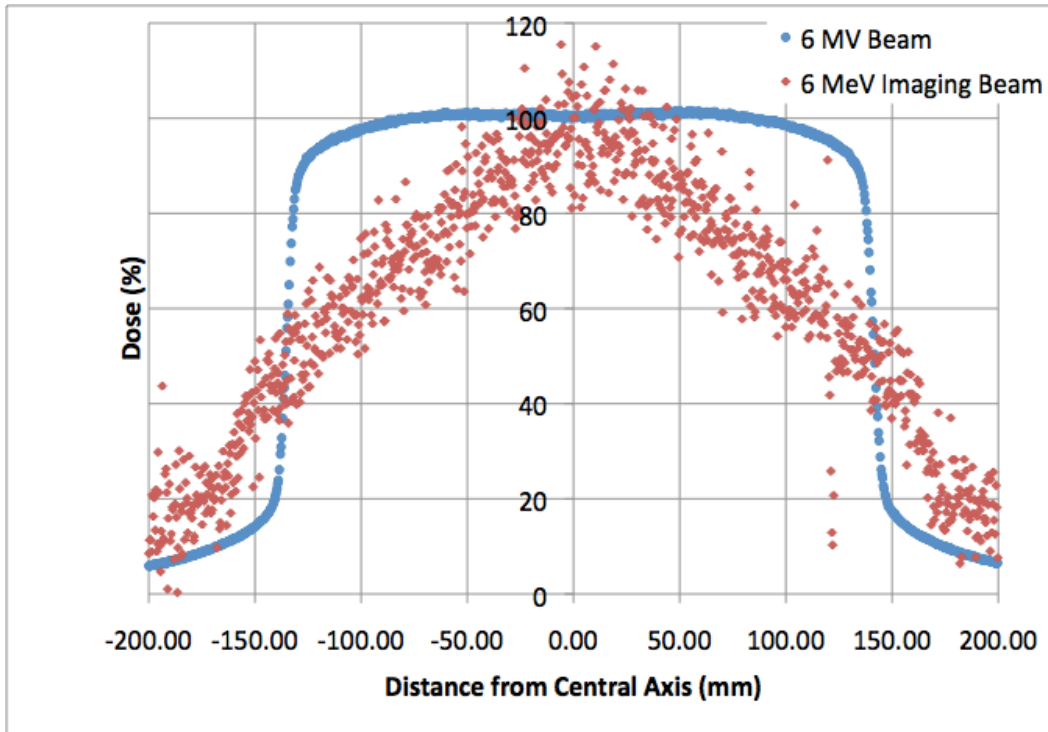


Figure 4.6: The profiles at 10 cm depth for the 6 MeV imaging beam and 6 MV treatment beam. The profiles were measured using a Wellhöfer IC-10 ion chamber being scanned across a 25 x 25 cm² field at a rate determined by Wellhöfer software.

To a lesser extent, the penumbra of the imaging beam may also be larger due to the focal spot, the region of the scattering foils from which most of the photons originate, being larger than that for a treatment beam. This would reduce the resolution of resulting images. While the focal spot size of the imaging beam was not studied, the resolution of the system was measured in a treatment beam as well as the imaging beam, because the treatment beam has a smaller focal spot.

The lack of flatness in the 6 MeV imaging beam is not a problem for imaging purposes since the attenuation observed by any given detector is always based on the open field signal for that particular detector. However, it could cause the noise, indicated by the standard deviation of the pixels in the image of a uniform phantom, to be greater towards the edges of the

field of view where the fluence is lower. In practice, most phantoms and patients being imaged are thicker at the center than at the periphery, reducing the fluence there and offsetting this effect. The prototype system is similar in this way to kVCT systems that purposely place a bow tie filter to create a similar looking fluence profile, and the MVCT TomoTherapy systems that do not employ flattening filters for imaging.

4.2 Artifact Correction

The projection data for the phantoms was corrected for both beam hardening, using the measured attenuation vs. thickness curve for each detector, as well as for the air gaps between detector blocks, using the uniform factor method. Taken together, the two corrections were able to produce a final image with no visible artifacts.

In Figure 4.7, the top left most image shows a reconstructed image of a uniform phantom without correction for either beam hardening or uniform factors. Concentric ring artifacts are very pronounced, and a gradual darkening can be seen if one observes the image from an outer edge and works toward the centre. The darker rings near the centre provide the illusion that the centre is lighter than more outer regions, however actual pixel values show an overall decrease toward the center, referred to as a beam hardening cupping artifact. A similar but far more pronounced effect is seen in the 6 MV image (bottom left), where there is beam hardening more from the flattening filter than from the phantom.

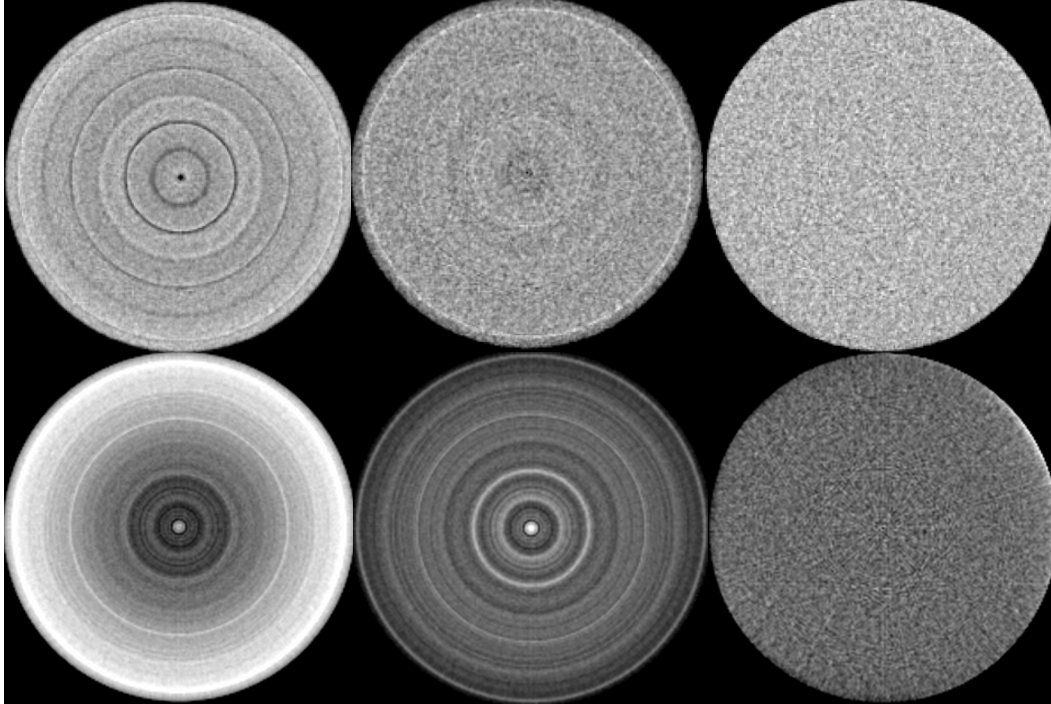


Figure 4.7: Uniform phantom imaged using the 6 MeV imaging beam (top row) and 6 MV treatment beam (bottom row) in fan beam geometry. The phantom is seen without beam hardening or uniform factor correction (left column), with only beam hardening correction (centre column), and with both beam hardening and uniform factor correction (right column). The brightness and contrast were adjusted separately for each image in order to maximize the visibility of the artifacts.

The centre images in Figure 4.7 show that the beam hardening correction is largely able to eliminate the cupping effect, although some circular artifacts remain.

Finally, after the data has undergone the uniform factor correction (right images in Figure 4.7), the ring artifacts are essentially gone and cannot be detected at any window and level settings. The uniform factor and beam hardening corrections were similarly effective for both the 6 MeV and 6 MV beams, in both fan beam and cone beam geometry. In the image done with the treatment beam using the uniform factor correction (bottom right in Figure 4.7), there is a slight brightening of the outer rim. This is an

artifact of the uniform factor process caused by the uniform phantom not being placed in the exact same position as the phantom being imaged. It is possible that this type of artifact could be reduced by using a slightly larger uniform phantom to calculate the uniform factors than the phantom being imaged.

4.3 Uniformity

The uniform factor correction shown in Figure 4.7 was successfully able to increase the uniformity index of the images from 99.5% before correction to 99.8% after correction. The maximum difference between the mean pixel value of a peripheral ROI and the central ROI, expressed as a percentage of the central ROI mean was 0.4% at 2 cGy dose.

The corrected uniformity index compares favorably to a published value of 99.5% for a commercial TomoTherapy MVCT system [Meeks, et al. 2005]. Because the TomoTherapy detector is focused to a radius of curvature of 110 cm while the actual source to detector distance is 145 cm, [Meeks, et al. 2005] it is more difficult to calibrate so as to obtain a uniform image. The maximum variation in mean pixel values between the central and peripheral ROIs of 0.4% is less than the 0.6% measured for the Siemens MVision flat panel system [Gayou et al. 2007 (2)] and 1% for MVCT on TomoTherapy [Meeks, et al. 2005].

For comparison, performance evaluations of typical kVCT systems [Garcia-Ramirez, et al. 2000; McCollough, et al. 1999] show a standard deviation in a uniform phantom of around 5 Hounsfield units, which corresponds to a uniformity of about 99.5%. The prototype MVCT system and clinical kVCT systems are therefore similar in this regard.

4.3.1 Signal to Noise Ratio

The signal to noise ratio of the system over a range of doses is seen in Figure 4.8. SNR^2 increases linearly with dose over the range of 2 to 20cGy. SNR^2 for the 6 MV treatment beam image at 62 cGy dose is about 45600 which will lie below the extrapolated straight line for the fan beam geometry of the 6 MeV beam in Figure 4.8. The point is not shown in the graph because the scales would shrink the other portion of the graph. Since the DQE decreases with energy, it is expected that the SNR would be lower in a 6 MV treatment than the 6 MeV imaging beam for the same dose.

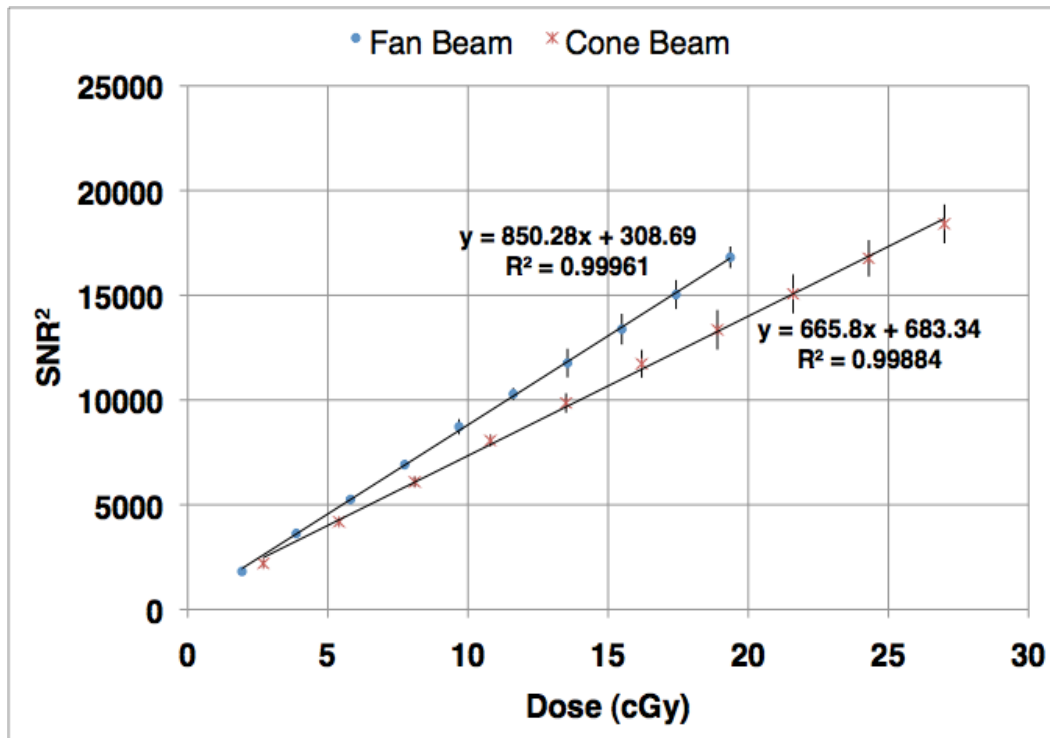


Figure 4.8: SNR^2 vs. dose in fan-beam and cone-beam geometry. The error bars are calculated using propagation of errors in estimating mean signal and noise (i.e. standard deviation) of pixels. R^2 is 0.9996 for fan beam and 0.999 for cone beam geometry.

The high degree of linearity of SNR^2 with dose ($R^2 > 0.999$) shows that the noise in our system comes primarily from photon counting statistics, not from electronic noise. In the cone beam geometry, we see that the SNR^2 is lower at a given dose due to higher noise. However, the dose estimates for the fan-beam are for a single rotation. In practice, the cone beam would require a single rotation, however, the multiple rotations at different locations in the phantom will be required in case of fan-beam geometry to cover the same volume. The accumulated total scan dose for the fan beam would therefore be larger than shown due to scatter, and the two curves might be closer together. Nonetheless, in cone beam geometry more scattered photons are detected than in multiple rotations of a fan beam detector, because a fan beam detector covers a smaller solid angle. For this reason it is expected that the SNR will be lower for a cone beam scan than a fan beam scan, even when multiple rotations are considered.

4.4 High Contrast Resolution

Figure 4.9 shows the images of the bar pattern insert of a CATPHAN500 obtained with the 6 MeV imaging beam, 6 MV treatment beam and TomoTherapy MVCT. The bar patterns are arranged in 1 line pair per cm (lp/cm) to 21 lp/cm. The prototype system can resolve at least 4 lp/cm (left image) and 5 lp/cm (center image) in the imaging and nominal treatment beams respectively. The TomoTherapy MVCT can resolve at least 4 lp/cm (right image). Both TomoTherapy and the prototype system have considerably poorer resolution than typical kVCT systems [Garcia-Ramirez, et al. 2000; McCollough, et al. 1999] that can resolve around 7 lp/cm while using the smoothing convolution kernels. There were no discernible differences in the high contrast resolution of our system when the fan-beam and cone-beam geometries were compared.

As the imaging photons were generated by bremsstrahlung in the electron scattering foils, the source is diffused, especially those photons that originate from the lower scattering foil. This limits the resolution to less than the capability of the detector array shown in the 6 MV image. In the 6 MeV imaging beam, the limiting spatial resolution is comparable to TomoTherapy MVCT and better than the published value of 3 lp/cm for the Siemens MVision flat panel MVCBCT system [Gayou, et al. 2007 (1)]. Although the dose is very high (60cGy) for our 6 MV image, the 6 MV bar pattern image has slightly superior resolution at 5 lp/cm compared to both 6 MeV and TomoTherapy MVCT images. In the 6 MV case, considerable scatter may be detected from the flattening filter, and the resolution is affected by the focal spot size of the Varian 600C linac. As our detector array is focused to the source, the resolution is expected to be uniform across the resulting images and should not degrade away from the center.

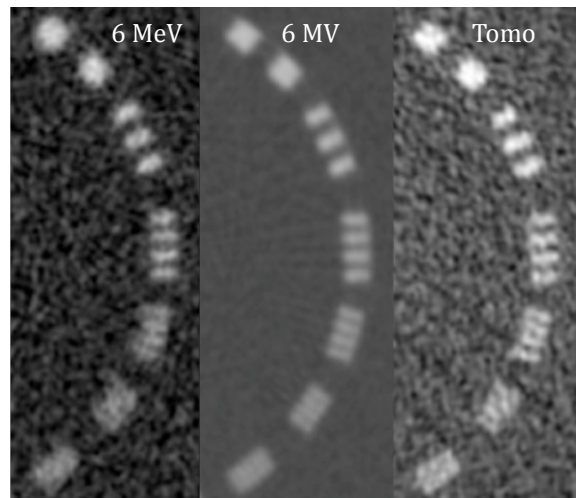


Figure 4.9: Portion of a CATPHAN500 resolution phantom having bar patterns ranging from 1 to 6 line pairs per cm. Images from left to right using: 6 MeV imaging beam at 2 cGy, 6 MV treatment beam at 60 cGy and TomoTherapy imaging beam with pitch =1.0.

The resolution of the prototype MVCT system is not expected to change throughout the field of view as the detector array is focused to the source. However, it was not possible to test this on the prototype system as the field of view is not large enough to permit the phantom to be moved more than a couple centimeters from the center.

4.5 Low Contrast Definition

Images of the low contrast detail insert of CATPHAN500 are shown in Figure 4.10 obtained with the prototype system with 2 cGy and 4 cGy doses, along with an image obtained with the MVCT on TomoTherapy. TomoTherapy dose estimates range from about 1.5 to 3 cGy [Hong, et al. 2007], so we are estimating about 2 cGy for our TomoTherapy images. Prototype images are taken in fan-beam geometry. Visibility of low contrast targets in 6 MeV beam prototype images at 2 cGy is comparable to the MVCT on TomoTherapy. The central white region with black center is an artifact in the TomoTherapy image. Low contrast details in our prototype image at 4 cGy are clearly better than the TomoTherapy image. Our cone-beam images were similar to our fan-beam images but had visibly inferior contrast at comparable dose level. In Figure 4.11, the contrast to noise ratio (CNR) is shown as a function of dose for the prototype system using the 6 MeV imaging beam in fan-beam and cone-beam geometry.

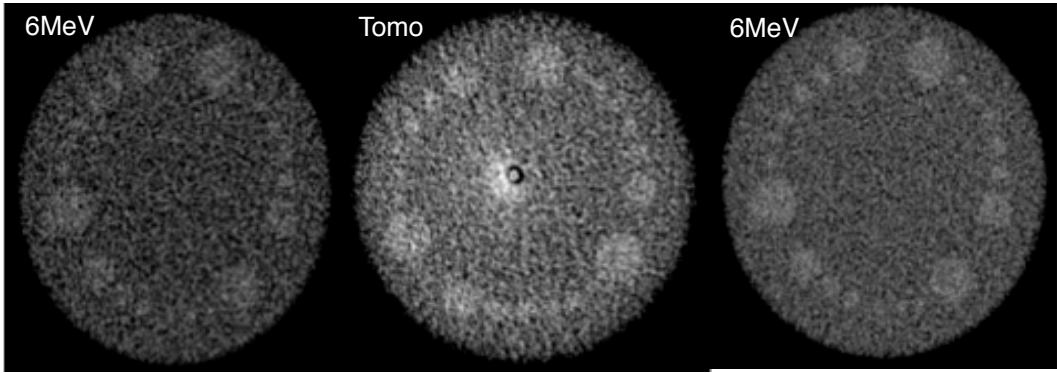


Figure 4.10: Custom designed low contrast phantom of CATPHAN500 showing plugs of 3.0%, 2.5%, and 1.5% contrast (clockwise from left). For each contrast level there are cylinders of 20, 4, 5, 6, 7, 8, and 15 mm diameter. Images from left to right: 6 MeV imaging beam at 2 cGy and 8 mm slice thickness, Tomo beam with pitch = 1.0 and 5 mm slice thickness, and 6 MeV imaging beam at 4 cGy and 8 mm slice thickness.

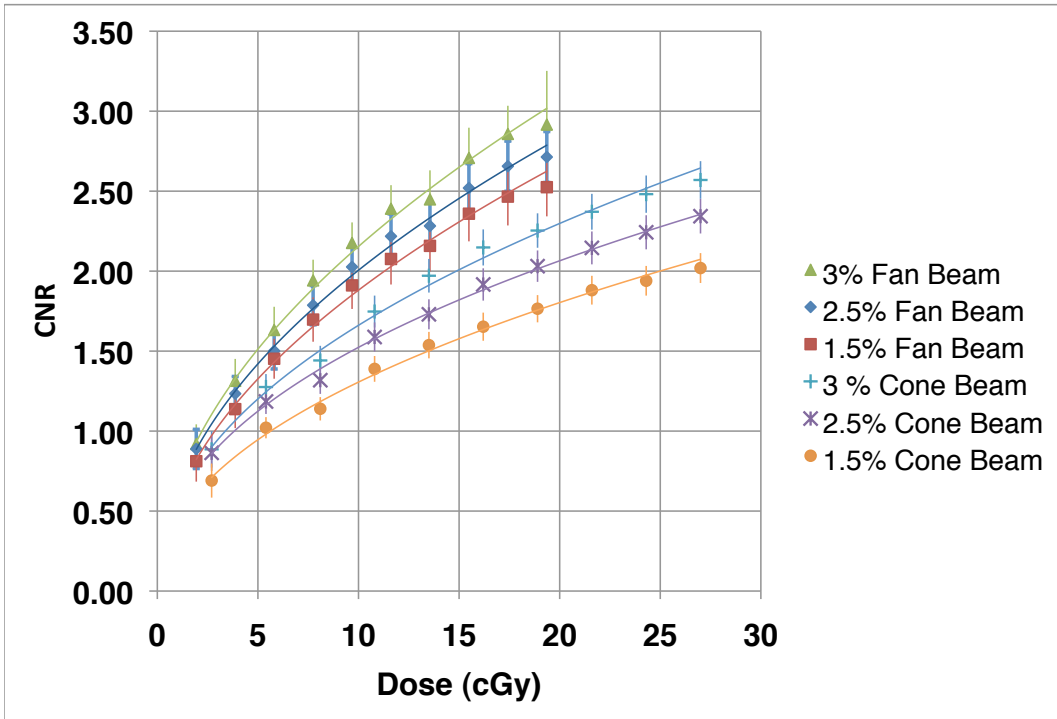


Figure 4.11: CNR as a function of scan dose in fan and cone beam geometry. Nominal contrast values for cobalt energy are given in the legend.

Our prototype system shows similar low contrast detectability to TomoTherapy at similar dose. The superior DQE of the thick crystal detectors is quite apparent when comparing our prototype to thin scintillator flat panel imagers. Our system could detect a 20 mm object at 1.5% contrast at 2 cGy dose, whereas 10 cGy was required to detect a 20 mm object at 1% contrast in a Siemens MVision system [Gayou, et al. 2007 (2)]. The 6 MeV image is better in part due to the lower energy photons as shown in the calculated spectrum. The images taken in the 6 MeV beam may slightly suffer due to the scatter radiation produced in the 4 cm solid water block used for removing electrons from the beam. The reduced CNR for cone-beam geometry is to be expected due to the lower contrast and increased noise in the presence of increased scatter radiation [Siewerdsen, et al. 2001].

4.6 CT Number Linearity

The mean pixel value vs. electron density curve in Figure 4.12 shows a very high degree of linearity ($R^2 > 0.9998$) in both fan and cone beam geometries over a range of electron densities. This is expected for a MVCT system. The slope of the mean pixel value curve is greater for fan-beam geometry, which gives an indication of the higher contrast in fan-beam geometry compared with cone-beam geometry.

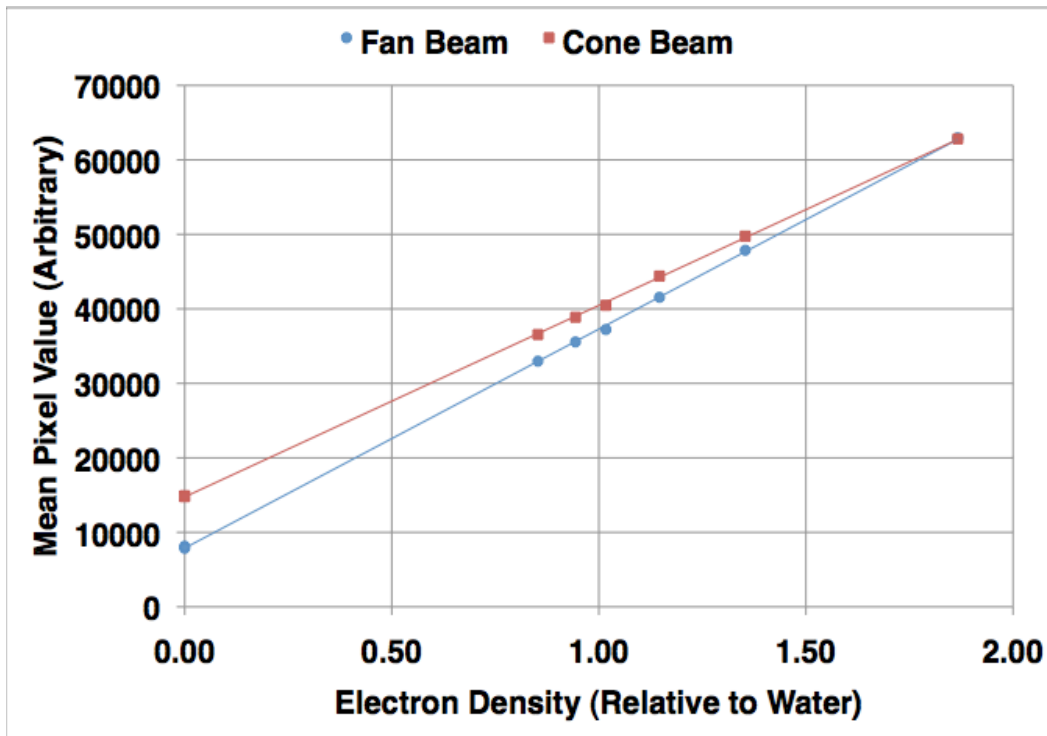


Figure 4.12: Mean pixel value as a function of electron density for fan beam and cone beam geometry. $R^2 = 0.9998$ for both geometries. The error bars are smaller than the size of the data points.

To illustrate the magnitude of the improvement in CT number linearity, a locally measured CT number vs. electron density curve for a kVCT system is shown in Figure 4.13. The non-linearity of the CT numbers makes it difficult to obtain accurate electron density values required to calculate dose in a treatment planning application. In practice, a “piece-wise linear” approximation of the curve seen in Figure 4.13 is used, wherein the CT numbers for air to approximately the electron density of water are considered to lie on one line, while those above a relative density of one are considered to lie on another line. This approach is limited, because in a kVCT scan CT number is not only a function of electron density, but also of atomic composition. Thus any such attempt to derive electron densities from a kVCT scan must rely on assumptions about the atomic composition of a tissue. It is possible in kVCT to gain knowledge about the composition of a tissue by doing multiple CT scans at different energies in a process called multi-energy CT that could improve the electron density calculation [Bazalova 2008]. However, it is unlikely that kVCT could match the inherent ability of MVCT to determine electron density as seen in Figure 4.12.

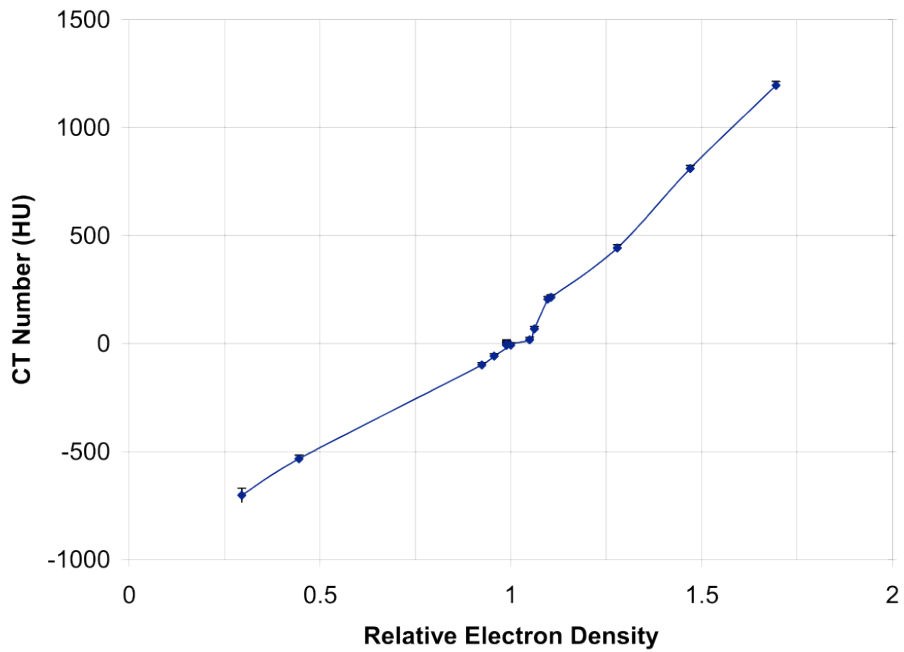


Figure 4.13: Mean pixel value as a function of relative electron density for a diagnostic CT scanner that uses an X-ray tube operating at 120 KV potential. The data is obtained for the system (Brilliance Big Bore, Philips Medical Systems) installed in the radiotherapy department of the Cross Cancer Institute. The data is generally not linear and has a discontinuity around a relative electron density of 1.0

References

Bazalova, M., Carrier, J., Beaulieu, L. & Verhaegen, F. Tissue segmentation in Monte Carlo treatment planning: A simulation study using dual-energy CT images. *Radiotherapy and Oncology* 86, 93-98 (2008).

Faddegon, B. A., Wu, V., Pouliot, J., Gangadharan, B. & Bani-Hashemi, A. Low dose megavoltage cone beam computed tomography with an unflattened 4 MV beam from a carbon target. *Medical physics* 35, 5777-5786 (2008).

Gayou, O. & Miften, M. Commissioning and clinical implementation of a mega-voltage cone beam CT system for treatment localization. *Medical physics* 34, 3183-3192 (2007).

Gayou, O., Parida, D. S., Johnson, M. & Miften, M. Patient dose and image quality from mega-voltage cone beam computed tomography imaging. *Medical physics* 34, 499-506 (2007).

Hanson, W. F., Berkley, L. W. & Peterson, M. Off-axis beam quality change in linear accelerator x-ray beams. *Medical physics* 7, 145-146 (1980).

Hong, T. S., Welsh, J. S., Ritter, M. A., Harari, P. M., Jaradat, H., Mackie, T. R. & Mehta, M. P. Megavoltage computed tomography: an emerging tool for image-guided radiotherapy. *American journal of clinical oncology* 30, 617-623 (2007).

Jarry, G. & Verhaegen, F. Electron beam treatment verification using measured and Monte Carlo predicted portal images. *Physics in Medicine and Biology* 50, 4977-4994 (2005).

Joseph, P. M. & Spital, R. D. The effects of scatter in x-ray computed tomography. *Medical physics* 9, 464-472 (1982).

Meeks, S. L., Harmon, J. F., Jr, Langen, K. M., Willoughby, T. R., Wagner, T. H. & Kupelian, P. A. Performance characterization of megavoltage computed tomography imaging on a helical tomotherapy unit. *Medical physics* 32, 2673-2681 (2005).

Siewerdsen, J. H. & Jaffray, D. A. Cone-beam computed tomography with a flat-panel imager: Magnitude and effects of x-ray scatter. *Medical physics* 28, 220-231 (2001).

Zhu, T. C., Das, I. J. & Bjärngård, B. E. Characteristics of bremsstrahlung in electron beams. *Medical physics* 28, 1352-1358 (2001).

CHAPTER 5: CONCLUSIONS

The image quality of an experimental MVCT system was comprehensively evaluated for this thesis. The MVCT system was an evolution of a previous cadmium tungstate photodiode detector based system designed and tested at the University of Alberta. The key attribute of this system is that it uses a focused 320 by 16 element array of 10 millimeter thick cadmium tungstate photodiode detectors. These detectors measure one millimeter by one millimeter in the plane facing the photon beam source, giving them the smallest cross section of any cadmium tungstate system tested so far. Unlike previous prototype systems constructed at the University of Alberta, this system is capable of multi-slice imagery (up to sixteen slices per rotation) and can be easily used with a medical linear accelerator as the beam source.

The use of cadmium tungstate detectors allows for significant improvement in DQE over flat panel imagers. This is expected to result in improved contrast in the images for a given dose. The low contrast definition of the prototype system was evaluated, along with its high contrast resolution, uniformity, and CT number linearity.

The prototype MVCT system was found to be able to detect a 15 mm diameter target of 1.5% contrast material using 2 cGy dose. This is an encouraging result and a clear improvement over flat panel imagers. A comparison with the gas chamber based TomoTherapy detector is ambiguous because the prototype system was tested in a beam of different spectral composition to the 3.5 MV imaging beam used in TomoTherapy. Previously published Monte Carlo simulations suggest that the contrast of this system could be improved even further by increasing

the detector thickness beyond 10 millimeters. Also, because of the small cross section of the detectors in this system, a significant portion of the cross section consists of the septa material between the detector elements, reducing the fill factor of the cadmium tungstate to 72%. The fill factor, and by extension the DQE and therefore the contrast, could be increased by using larger detector pitch. This is particularly true in the slice thickness direction, since the small slice thickness provided by this system of one millimeter at the detector may not be required for clinical applications. The detector pitch in the imaging plane could also be increased since the spatial resolution of the MVCT is also affected by the x-ray source focal spot.

The system has demonstrated resolution of at least 5 lp/cm. Because the detector is focused to the photon source, this resolution is expected to be uniform across the field of view and does not degrade at points away from the central axis of the beam. This is an advantage over flat panel imagers as well as the current mis-focused detector used in TomoTherapy. Furthermore, the system may have an even higher resolution than this if it is used with a linac having a very small focal spot and without a flattening filter.

The high uniformity index, 99.8%, shows that the system can be calibrated for artifacts resulting from beam hardening and the air gaps between detector blocks. The system shows excellent linearity of mean pixel value with electron density ($R^2=0.9998$), which is an advantage of MVCT systems for treatment planning, especially in situations where metal artifacts are a problem.

Because this prototype system is composed of tiled 16 by 16 detector blocks, it would be possible to tile the blocks on a portion of a sphere in three dimensions to construct a focused area detector. This area detector

could be used for cone-beam computed tomography, which is useful for detecting setup errors in image guided radiotherapy. Such a detector would also fulfill the roles of an EPID, allowing for better quality planar images than current EPIDs at a given dose, as well as recording images during treatment that can be used for dose verification.

In conclusion, a cadmium tungstate MVCT system was demonstrated to have better low contrast definition at a given dose than flat panel MVCT systems. This allows for greater soft tissue visualization at a given dose than other systems. This system is therefore better able to distinguish between soft tissues. A fan beam or cone beam detector similar to this system could be useful for treatment planning, radiation therapy setup, and dose verification.

BIBLIOGRAPHY

Almond, P. R., Biggs, P. J., Coursey, B. M., Hanson, W. F., Huq, M. S., Nath, R. & Rogers, D. W. O. AAPM's TG-51 protocol for clinical reference dosimetry of high-energy photon and electron beams. *Medical physics* 26, 1847-1870 (1999).

Anastasio, M. A., Shi, D., Pan, X., Pelizzari, C. & Munro, P. A preliminary investigation of local tomography for megavoltage CT imaging. *Medical physics* 30, 2969-2980 (2003).

Antonuk, L. E. Electronic portal imaging devices: A review and historical perspective of contemporary technologies and research. *Physics in Medicine and Biology* 47, R31-R65 (2002).

Azevedo, S. G., Martz, H. E. & Schneberk, D. J. *Potential of computed tomography for inspection of aircraft components* (1993).

Barrett & Swindell. in *Radiological Imaging* (Academic Press, San Diego, California, 1981).

Bazalova, M., Carrier, J., Beaulieu, L. & Verhaegen, F. Tissue segmentation in Monte Carlo treatment planning: A simulation study using dual-energy CT images. *Radiotherapy and Oncology* 86, 93-98 (2008).

Bendahan, J. & Garms, W. *Megavolt computed tomography for air cargo container inspection* (2008).

Berger, M. J., et al. Stopping-Power and Range Tables for Electrons, Protons, and Helium Ions. in National Institute of Standards and Technology [database online]. 2005 Available from <http://www.nist.gov/login.ezproxy.library.ualberta.ca/physlab/data/star/index.cfm>.

Bjarngard, B. E. & Shackford, H. Attenuation in high-energy x-ray beams. *Medical physics* 21, 1069-1073 (1994).

Brahme, A., Lind, B. & Nafstadius, P. Radiotherapeutic computed tomography with scanned photon beams. *International Journal of Radiation Oncology Biology Physics* 13, 95-101 (1987).

Brooks, R. A. & Di Chiro, G. Beam hardening in X-ray reconstructive tomography. *Physics in Medicine and Biology* 21, 390-398 (1976).

Budgell, G. Intensity modulated radiotherapy (IMRT) - An introduction. *Radiography* 8, 241-249 (2002).

Bushberg, J. T., Seibert, J. A., Leidholdt, E. M. & Boone, J. M. in *The Essential Physics of Medical Imaging*, 2002).

Chesler, D. A., Riederer, S. J. & Pelc, N. J. Noise due to photon counting statistics in computed X ray tomography. *J.COMPUT.ASSISTED TOMOGRAPHY* 1, 64-74 (1977).

Cheung, J., Aubry, J. F., Yom, S. S., Gottschalk, A. R., Celi, J. C. & Pouliot, J. Dose Recalculation and the Dose-Guided Radiation Therapy (Dgrt) Process using Megavoltage Cone-Beam CT. *International journal of radiation oncology, biology, physics* (2009).

Cho, P. S., Johnson, R. H. & Griffin, T. W. Cone-beam CT for radiotherapy applications. *Physics in Medicine and Biology* 40, 1863-1883 (1995).

Clayton, J. E., Virshup, G. & Davis, A. *Enhanced Image capabilities for industrial radiography applications using megavoltage X-ray sources and digital flat panels* (2008).

Cremers, F., Frenzel, T., Kausch, C., Albers, D., Schonborn, T. & Schmidt, R. Performance of electronic portal imaging devices (EPIDs) used in radiotherapy: image quality and dose measurements. *Medical physics* 31, 985-996 (2004).

Droege, R. T. & Morin, R. L. A practical method to measure the MTF of CT scanners. *Medical physics* 9, 758-760 (1982).

El-Mohri, Y., Jee, K. W., Antonuk, L. E., Maolinbay, M. & Zhao, Q. Determination of the detective quantum efficiency of a prototype, megavoltage indirect detection, active matrix flat-panel imager. *Medical physics* 28, 2538-2550 (2001).

Faddegon, B. A., Wu, V., Pouliot, J., Gangadharan, B. & Bani-Hashemi, A. Low dose megavoltage cone beam computed tomography with an unflattened 4 MV beam from a carbon target. *Medical physics* 35, 5777-5786 (2008).

Fallone, B. G., Murray, B., Rathee, S., Stanescu, T., Steciw, S., Vidakovic, S., Blosser, E. & Tymofichuk, D. First MR images obtained during megavoltage photon irradiation from a prototype integrated linac-MR system. *Medical physics* 36, 2084-2088 (2009).

Flynn, R. T., Hartmann, J., Bani-Hashemi, A., Nixon, E., Alfredo, R., Siochi, C., Pennington, E. C. & Bayouth, J. E. Dosimetric characterization and

application of an imaging beam line with a carbon electron target for megavoltage cone beam computed tomography. *Medical physics* 36, 2181-2192 (2009).

Ford, E. C., Chang, J., Mueller, K., Sidhu, K., Todor, D., Mageras, G., Yorke, E., Ling, C. C. & Amols, H. Cone-beam CT with megavoltage beams and an amorphous silicon electronic portal imaging device: Potential for verification of radiotherapy of lung cancer. *Medical physics* 29, 2913-2924 (2002).

Galbraith, D. M. Low-energy imaging with high-energy bremsstrahlung beams. *Medical physics* 16, 734-746 (1989).

Garcia-Ramirez, J. L., Mutic, S., Dempsey, J. F., Low, D. A. & Purdy, J. A. Performance evaluation of an 85-cm-bore X-ray computed tomography scanner designed for radiation oncology and comparison with current diagnostic CT scanners. *International Journal of Radiation Oncology Biology Physics* 52, 1123-1131 (2002).

Gayou, O. & Miften, M. Commissioning and clinical implementation of a mega-voltage cone beam CT system for treatment localization. *Medical physics* 34, 3183-3192 (2007).

Gayou, O., Parda, D. S., Johnson, M. & Miften, M. Patient dose and image quality from mega-voltage cone beam computed tomography imaging. *Medical physics* 34, 499-506 (2007).

Groh, B. A., Siewerdsen, J. H., Drake, D. G., Wong, J. W. & Jaffray, D. A. A performance comparison of flat-panel imager-based MV and kV cone-beam CT. *Medical physics* 29, 967-975 (2002).

Guanf, H. & Zhu, Y. Feasibility of megavoltage portal CT using an electronic portal imaging device (EPID) and a multi-level scheme algebraic reconstruction technique (MLS-ART). *Physics in Medicine and Biology* 43, 2925-2937 (1998).

Gullberg, G. T., Crawford, C. R. & Tsui, B. M. W. Reconstruction Algorithm for Fan Beam with a Displace Center-of-rotation. *IEEE Transactions on Medical Imaging* MI-5, 23-29 (1986).

Gur, D., Bukovitz, A. G. & Serago, C. Photon contamination in 8-20-MeV electron beams from a linear accelerator. *Medical physics* 6, 145-146 (1979).

Hanson, W. F., Berkley, L. W. & Peterson, M. Off-axis beam quality change in linear accelerator x-ray beams. *Medical physics* 7, 145-146 (1980).

Hesse, B. M., Spies, L. & Groh, B. A. Tomotherapeutic portal imaging for radiation treatment verification. *Physics in Medicine and Biology* 43, 3607-3616 (1998).

Hong, T. S., Welsh, J. S., Ritter, M. A., Harari, P. M., Jaradat, H., Mackie, T. R. & Mehta, M. P. Megavoltage computed tomography: an emerging tool for image-guided radiotherapy. *American journal of clinical oncology* 30, 617-623 (2007).

Hounsfield, G. N. Computerized transverse axial scanning (tomography): I. Description of system. *British Journal of Radiology* 46, 1016-1022 (1973).

Ishmael Parsai, E., Pearson, D. & Kvale, T. Consequences of removing the flattening filter from linear accelerators in generating high dose rate photon beams for clinical applications: A Monte Carlo study verified by measurement. *Nuclear Instruments and Methods in Physics Research, Section B: Beam Interactions with Materials and Atoms* 261, 755-759 (2007).

Jaffray, D. A. & Siewerdsen, J. H. Cone-beam computed tomography with a flat-panel imager: Initial performance characterization. *Medical physics* 27, 1311-1323 (2000).

Jans, H. S., Syme, A. M., Rathee, S. & Fallone, B. G. 3D interfractional patient position verification using 2D-3D registration of orthogonal images. *Medical physics* 33, 1420-1439 (2006).

Jarry, G. & Verhaegen, F. Electron beam treatment verification using measured and Monte Carlo predicted portal images. *Physics in Medicine and Biology* 50, 4977-4994 (2005).

Johns H.E. & Cunningham J.R. in *The Physics of Radiology* (Thomas, Springfield, IL, 1983).

Joseph, P. M. & Spital, R. D. The effects of scatter in x-ray computed tomography. *Medical physics* 9, 464-472 (1982).

Kawrakow, I., and Rogers, D. W. O. The EGSnrc Code System: Monte Carlo Simulation of Electron and Photon Transport. in National Research Council of Canada [database online]. 2006 Available from <http://irs.inms.nrc.ca/login.ezproxy.library.ualberta.ca/software/egsnrc/documentation/pirs701/index.html>.

Keall, P. J., Chock, L. B., Jeraj, R., Siebers, J. V. & Mohan, R. Image reconstruction and the effect on dose calculation for hip prostheses. *Medical Dosimetry* 28, 113-117 (2003).

Keller, H., Glass, M., Hinderer, R., Ruchala, K., Jeraj, R., Olivera, G. & Rock Mackie, T. Monte Carlo study of a highly efficient gas ionization detector for megavoltage imaging and image-guided radiotherapy. *Medical physics* 29, 165-175 (2002).

Kijewski, P. K. & Bjarngard, B. E. The use of computed tomography data for radiotherapy dose calculations. *International Journal of Radiation Oncology Biology Physics* 4, 429-435 (1978).

Kirvan, P. F., Monajemi, T. T., Fallone, B. G. & Rathee, S. Performance characterization of a MVCT scanner using multislice thick, segmented cadmium tungstate-photodiode detectors. *Medical physics* 37, 249-257 (2010).

Kobayashi, M., Ishii, M., Usuki, Y. & Yahagi, H. Cadmium tungstate scintillators with excellent radiation hardness and low background. *Nuclear Inst. and Methods in Physics Research, A* 349, 407-411 (1994).

Lattanzi, J., McNeeley, S., Pinover, W., Horwitz, E., Das, I., Schultheiss, T. E. & Hanks, G. E. A comparison of daily CT localization to a daily ultrasound-based system in prostate cancer. *International Journal of Radiation Oncology Biology Physics* 43, 719-725 (1999).

Mackie, T. R., Balog, J., Ruchala, K., Shepard, D., Aldridge, S., Fitchard, E., Reckwerdt, P., Olivera, G., McNutt, T. & Mehta, M. Tomotherapy. *Seminars in radiation oncology* 9, 108-117 (1999).

Mackie, T. R., Kapatoes, J., Ruchala, K., Lu, W., Wu, C., Olivera, G., Forrest, L., Tome, W., Welsh, J., Jeraj, R., Harari, P., Reckwerdt, P., Paliwal, B., Ritter, M., Keller, H., Fowler, J. & Mehta, M. Image guidance for precise conformal radiotherapy. *International Journal of Radiation Oncology Biology Physics* 56, 89-105 (2003).

McCollough, C. H. & Zink, F. E. Performance evaluation of a multi-slice CT system. *Medical physics* 26, 2223-2230 (1999).

Meeks, S. L., Harmon, J. F., Jr, Langen, K. M., Willoughby, T. R., Wagner, T. H. & Kupelian, P. A. Performance characterization of megavoltage computed tomography imaging on a helical tomotherapy unit. *Medical physics* 32, 2673-2681 (2005).

Mei, X., Rowlands, J. A. & Pang, G. Electronic portal imaging based on Cerenkov radiation: A new approach and its feasibility. *Medical physics* 33, 4258-4270 (2006).

Midgley, S., Millar, R. M. & Dudson, J. A feasibility study for megavoltage cone beam CT using a commercial EPID. *Physics in Medicine and Biology* 43, 155-169 (1998).

Monajemi, T. T., Fallone, B. G. & Rathee, S. Thick, segmented CdWO₄-photodiode detector for cone beam megavoltage CT: a Monte Carlo study of system design parameters. *Medical physics* 33, 4567-4577 (2006).

Monajemi, T. T., Steciw, S., Fallone, B. G. & Rathee, S. Modeling scintillator-photodiodes as detectors for megavoltage CT. *Medical physics* 31, 1225-1234 (2004).

Monajemi, T. T., Tu, D., Fallone, B. G. & Rathee, S. A bench-top megavoltage fan-beam CT using CdWO₄-photodiode detectors. II. Image performance evaluation. *Medical physics* 33, 1090-1100 (2006).

Morin, O., Aubry, J. -, Aubin, M., Chen, J., Descovich, M., Hashemi, A. - & Pouliot, J. Physical performance and image optimization of megavoltage cone-beam CT. *Medical physics* 36, 1421-1432 (2009).

Morin, O., Gillis, A., Chen, J., Aubin, M., Bucci, M. K., Roach, M., 3rd & Pouliot, J. Megavoltage cone-beam CT: system description and clinical applications. *Medical dosimetry : official journal of the American Association of Medical Dosimetrists* 31, 51-61 (2006).

Morin, O., Gillis, A., Descovich, M., Chen, J., Aubin, M., Aubry, J., Chen, H., Gottschalk, A. R., Xia, P. & Pouliot, J. Patient dose considerations for routine megavoltage cone-beam CT imaging. *Medical physics* 34, 1819-1827 (2007).

Moseley, D. J., White, E. A., Wiltshire, K. L., Rosewall, T., Sharpe, M. B., Siewerdsen, J. H., Bissonnette, J. P., Gospodarowicz, M., Warde, P., Catton, C. N. & Jaffray, D. A. Comparison of localization performance with implanted fiducial markers and cone-beam computed tomography for on-line image-guided radiotherapy of the prostate. *International journal of radiation oncology, biology, physics* 67, 942-953 (2007).

Mosleh-Shirazi, M. A., Evans, P. M., Swindell, W., Webb, S. & Partridge, M. A cone-beam megavoltage CT scanner for treatment verification in conformal radiotherapy. *Radiotherapy and Oncology* 48, 319-328 (1998).

Munro, P. Portal imaging technology: Past, present, and future. *Seminars in radiation oncology* 5, 115-133 (1995).

Nakagawa, K., Aoki, Y., Akanuma, A., Onogi, Y., Terahara, A., Sakata, K., Muta, N., Sasaki, Y., Kawakami, H. & Hanakawa, K. Real-time beam

monitoring in dynamic conformation therapy. *International Journal of Radiation Oncology Biology Physics* 30, 1233-1238 (1994).

Nakagawa, K., Aoki, Y., Akanuma, A., Sakata, K., Karasawa, K., Terahara, A., Onogi, Y., Hasezawa, K. & Sasaki, Y. Technological features and clinical feasibility of megavoltage CT scanning. *European radiology* 2, 184-189 (1992).

Ostapiak, O. Z., O'Brien, P. F. & Faddegon, B. A. Megavoltage imaging with low Z targets: Implementation and characterization of an investigational system. *Medical physics* 25, 1910-1918 (1998).

Parker, R. P., Hobday, P. A. & Cassell, K. J. The direct use of CT numbers in radiotherapy dosage calculations for inhomogeneous media. *Physics in Medicine and Biology* 24, 802-809 (1979).

Peng, C., Kainz, K., Lawton, C. & Li, X. A. A comparison of daily megavoltage CT and ultrasound image guided radiation therapy for prostate cancer. *Medical physics* 35, 5619-5628 (2008).

Ramachandran, G. N. & Lakshminarayanan, A. V. Three-dimensional reconstruction from radiographs and electron micrographs: application of convolutions instead of Fourier transforms. *Proceedings of the National Academy of Sciences of the United States of America* 68, 2236-2240 (1971).

Rathee, S., Tu, D., Monajemi, T. T., Rickey, D. W. & Fallone, B. G. A bench-top megavoltage fan-beam CT using CdWO₄-photodiode detectors. I. System description and detector characterization. *Medical physics* 33, 1078-1089 (2006).

Rosset, A., Spadola, L. & Ratib, O. OsiriX: An open-source software for navigating in multidimensional DICOM images. *Journal of Digital Imaging* 17, 205-216 (2004).

Ruchala, K. J., Olivera, G. H., Kapatoes, J. M., Schloesser, E. A., Reckwerdt, P. J. & Makie, T. R. Megavoltage CT image reconstruction during tomotherapy treatments. *Physics in Medicine and Biology* 45, 3545-3562 (2000).

Ruchala, K. J., Olivera, G. H., Schloesser, E. A., Hinderer, R. & Mackie, T. R. Calibration of a tomotherapeutic MVCT system. *Physics in Medicine and Biology* 45, N27-36 (2000).

Ruchala, K. J., Olivera, G. H., Schloesser, E. A. & Mackie, T. R. Megavoltage CT on a tomotherapy system. *Physics in Medicine and Biology* 44, 2597-2621 (1999).

Samant, S. S., Gopal, A., Jain, J., Xia, J. & DiBianca, F. A. Design of a prototype tri-electrode ion-chamber for megavoltage X-ray imaging. *Nuclear Instruments and Methods in Physics Research, Section A: Accelerators, Spectrometers, Detectors and Associated Equipment* 573, 398-409 (2007).

Sawant, A., Antonuk, L. E., El-Mohri, Y., Li, Y., Su, Z., Wang, Y., Yamamoto, J., Zhao, Q., Du, H., Daniel, J. & Street, R. Segmented phosphors: MEMS-based high quantum efficiency detectors for megavoltage x-ray imaging. *Medical physics* 32, 553-565 (2005).

Sawant, A., Antonuk, L. E., El-Mohri, Y., Zhao, Q., Li, Y., Su, Z., Wang, Y., Yamamoto, J., Du, H., Cunningham, I., Klugerman, M. & Shah, K. Segmented crystalline scintillators: An initial investigation of high quantum efficiency detectors for megavoltage x-ray imaging. *Medical physics* 32, 3067-3083 (2005).

Schroeder, C., Stanescu, T., Rathee, S. & Fallone, B. G. Lag measurement in an a-Se active matrix flat-panel imager. *Medical physics* 31, 1203-1209 (2004).

Schulz, R. J., Almond, P. R. & Cunningham, J. R. A protocol for the determination of absorbed dose from high-energy photon and electron beams. *Medical physics* 10, 741-771 (1983).

Seco, J. & Evans, P. M. Assessing the effect of electron density in photon dose calculations. *Medical physics* 33, 540-552 (2006).

Seppi, E. J., Munro, P., Johnsen, S. W., Shapiro, E. G., Tognina, C., Jones, D., Pavkovich, J. M., Webb, C., Mollov, I., Partain, L. D. & Colbeth, R. E. Megavoltage cone-beam computed tomography using a high-efficiency image receptor. *International journal of radiation oncology, biology, physics* 55, 793-803 (2003).

Shi, D., Anastasio, M. A., Pan, X., Pelizzari, C. & Munro, P. *Investigation of megavoltage local tomography for detecting setup errors in radiation therapy* Ser. 5029, 2003).

Siewerdsen, J. H. & Jaffray, D. A. Cone-beam computed tomography with a flat-panel imager: Magnitude and effects of x-ray scatter. *Medical physics* 28, 220-231 (2001).

Sillanpaa, J., Chang, J., Mageras, G., Yorke, E., De Arruda, F., Rosenzweig, K. E., Munro, P., Seppi, E., Pavkovich, J. & Amols, H. Low-dose megavoltage cone-beam computed tomography for lung tumors using a high-efficiency image receptor. *Medical physics* 33, 3489-3497 (2006).

Simpson, R. G., Chen, C. T., Grubbs, E. A. & Swindell, W. A 4-MV CT scanner for radiation therapy: The prototype system. *Medical physics* 9, 574-579 (1982).

Smith-Bindman, R., Lipson, J., Marcus, R., Kim, K. -, Mahesh, M., Gould, R., Berrington De González, A. & Miglioretti, D. L. Radiation dose associated with common computed tomography examinations and the associated lifetime attributable risk of cancer. *Archives of Internal Medicine* 169, 2078-2086 (2009).

Stutzel, J., Oelfke, U. & Nill, S. A quantitative image quality comparison of four different image guided radiotherapy devices. *Radiotherapy and oncology : journal of the European Society for Therapeutic Radiology and Oncology* 86, 20-24 (2008).

Swindell, W. A 4-MV CT scanner for radiation therapy: Spectral properties of the therapy beam. *Medical physics* 10, 347-351 (1983).

Swindell, W., Simpson, R. G. & Oleson, J. R. Computed tomography with a linear accelerator with radiotherapy applications. *Medical physics* 10, 416-420 (1983).

Thomas, T. H., Devakumar, D., Purnima, S. & Ravindran, B. P. The adaptation of megavoltage cone beam CT for use in standard radiotherapy treatment planning. *Physics in Medicine and Biology* 54, 2067-2077 (2009).

van Elmpt, W., Nijsten, S., Petit, S., Mijnheer, B., Lambin, P. & Dekker, A. 3D in vivo dosimetry using megavoltage cone-beam CT and EPID dosimetry. *International journal of radiation oncology, biology, physics* 73, 1580-1587 (2009).

Verellen, D., De Ridder, M. & Storme, G. A (short) history of image-guided radiotherapy. *Radiotherapy and oncology : journal of the European Society for Therapeutic Radiology and Oncology* 86, 4-13 (2008).

Wang, Y. et al. *Theoretical investigation of very high quantum efficiency, segmented, crystalline detectors for low-contrast visualization in megavoltage cone-beam CT* Ser. 6142 II, 2006).

Wang, Y., Antonuk, L. E., El-Mohri, Y. & Zhao, Q. A Monte Carlo investigation of Swank noise for thick, segmented, crystalline scintillators for radiotherapy imaging. *Medical physics* 36, 3227-3238 (2009).

Wang, Y., Antonuk, L. E., El-Mohri, Y., Zhao, Q., Sawant, A. & Du, H. Monte Carlo investigations of megavoltage cone-beam CT using thick,

segmented scintillating detectors for soft tissue visualization. *Medical physics* 35, 145-158 (2008).

Wei, J., Sandison, G. A., Hsi, W. -, Ringor, M. & Lu, X. Dosimetric impact of a CT metal artefact suppression algorithm for proton, electron and photon therapies. *Physics in Medicine and Biology* 51, 5183-5197 (2006).

Welsh, J. S., Bradley, K., Ruchala, K. J., Mackie, T. R., Mañon, R., Patel, R., Wiederholt, P., Lock, M., Hui, S. & Mehta, M. P. Megavoltage computed tomography imaging: A potential tool to guide and improve the delivery of thoracic radiation therapy. *Clinical Lung Cancer* 5, 303-306 (2004).

Yang, D., Chaudhari, S. R., Goddu, S. M., Pratt, D., Khullar, D., Deasy, J. O. & El Naqa, I. Deformable registration of abdominal kilovoltage treatment planning CT and tomotherapy daily megavoltage CT for treatment adaptation. *Medical physics* 36, 329-338 (2009).

Yartsev, S., Kron, T. & Van Dyk, J. Tomotherapy as a tool in image-guided radiation therapy (IGRT): Theoretical and technological aspects. *Biomedical Imaging and Intervention Journal* 3 (2007).

Zhu, T. C., Das, I. J. & Bjärngard, B. E. Characteristics of bremsstrahlung in electron beams. *Medical physics* 28, 1352-1358 (2001).

Zubal, I. G., Harrell, C. R., Smith, E. O., Rattner, Z., Gindi, G. & Hoffer, P. B. Computerized three-dimensional segmented human anatomy. *Medical physics* 21, 299-302 (1994).